

Numerical Analysis of an Acoustofluidic Device for Particle Trapping

BY

MARCO RAGONE

B.S, Politecnico di Torino, Turin, Italy, 2016

THESIS

Submitted as partial fulfillment of the requirements
for the degree of Master of Science in Mechanical Engineering
in the Graduate College of the
University of Illinois at Chicago, 2018

Chicago, Illinois

Defense Committee:

Jie Xu, Chair and Advisor

Sabri Cetin

Pietro Asinari, Politecnico di Torino

ACKNOWLEDGMENTS

Foremost, I would like to thank my advisor Prof. Jie Xu for let me discover the interesting and promising cutting-edge science of microfluidics.

Besides my advisors, I would like to express my sincere gratitude to all the people in the Microfluidic Laboratory who helped me to fulfill my thesis. First, I would like to thank Yang, who had been supporting me the entire semester, providing helpful advices and motivating me to develop innovative ideas. I am grateful to my friend Enrico, for his patience in assisting me in the experimental part of my research, in designing and fabricating the micro-device and for the funny moments we spent together. I want to thank all the other students in the lab for the stimulating discussions which truly inspired me to pursue in my work. I want to thank also all my friends, who have been at my side in all of these years, for the moments of happiness and laughing spent together but also for the hard times of studying before the exams, when the support we gave to each other was fundamental to overcome the challenges in front of us. Finally, I want to thank my family, my parents and my brother, my uncles, my cousins and my granny who has just passed away, for encouraging me and for making my life special.

TABLE OF CONTENTS

<u>CHAPTER</u>		<u>PAGE</u>
1	INTRODUCTION	
1.1	Background.....	1
1.2	Previous numerical studies of acoustofluidics.....	4
2	FUNCTIONS AND ACOUSTIC ACTUATION OF PILLARS IN MICROFLUIDIC DEVICES	
2.1	Introduction.....	8
2.2	Background.....	8
2.3	Acoustic actuations of cylindrical pillars.....	10
3	EQUATIONS OF ACOUSTOFLUIDICS	
3.1	Introduction.....	13
3.2	Governing equations.....	13
3.3	The Nyborg's perturbation method.....	15
3.4	The first-order problem.....	17
3.5	The second-order problem.....	20
3.6	Acoustic Streaming and Acoustic Radiation Force.....	21
3.7	Acoustic actuation of two planar parallel walls.....	23
4	ACOUSTIC STREAMING	
4.1	Introduction.....	29
4.2	Physical process.....	29
4.3	Acoustic streaming between two parallel and infinite oscillating plates.....	32

TABLE OF CONTENTS (continued)

<u>CHAPTER</u>		<u>PAGE</u>
	4.4 Acoustic streaming in a cylindrical oscillating body in a fluid at rest.....	33
5	ACOUSTIC RADIATION FORCE	
	5.1 Introduction.....	36
	5.2 The general equation.....	37
	5.3 The thermoviscous model of the acoustic radiation force.....	41
6	EXPERIMENTAL SET-UP	
	6.1 Introduction.....	44
	6.2 Instruments used in the xperiment.....	45
7	NUMERICAL SIMULATION	
	7.1 Introduction.....	50
	7.2 Geometry.....	50
	7.3 Computational domain.....	52
	7.4 Numerical modelling.....	53
	7.5 Boundary conditions.....	59
	7.6 Mesh convergence.....	64
	7.7 Results and discussion.....	69
8	CONCLUSIONS	
	8.1 Summary.....	97
	8.2 Future works.....	100
	APPENDIX	101
	CITED LITERATURE	109
	VITA	112

LIST OF TABLES

<u>TABLE</u>		<u>PAGE</u>
I	PHYSICAL PARAMETERS OF THE FLUID AND THE PARTICLES.....	63

LIST OF FIGURES

<u>FIGURE</u>	<u>PAGE</u>
1	Scheme of the pillars used for Determinist Lateral Displacement applications (a) Cell sorting in DLD microdevices (b). Reproduced with permission from Royal Society of Chemistry.....9
2	Acoustic actuation of PDMS cilia for fluid mixing in Huang <i>et al</i> micro-channel. Reproduced with permission from Institute of Physics Publishing.....10
3	Uniform distribution of aligned pillars in the micro-channel used by Huang <i>et al</i> . Reproduced with permission from Institute of Physics Publishing..... 11
4	Acoustically driven oscillation of a PDMS cilia (a). Linear dependence of the cilia's deflection on the applied voltage (b). Reproduced with permission from Institute of Physics Publishing.....11
5	Acoustic actuation of two planar and parallel walls with a standing wave. Reproduced with permission from Royal Society of Chemistry.....24
6	Acoustic response at the resonance condition of a fluid enclosed between two planar and parallel oscillating walls. Reproduced with permission from Royal Society of Chemistry.....27
7	Scheme of the Rayleigh-Schlichting streaming near an oscillating wall. Reproduced with permission from Royal Society of Chemistry.....31
8	Scheme of the Rayleigh-Schlichting streaming in the third Rayleigh's problem. Reproduced with permission from Royal Society of Chemistry.....32
9	Rayleigh-Schlichting streaming in an oscillating cylinder in a fluid at rest. Reproduced with permission from Royal Society of Chemistry.....33
10	Far field region $r \gg \lambda$, where the potential ϕ_1 is the sum of the incoming and scattered potentials (a). The scattered potential in the far and near field (b). Reproduced with permission from Royal Society of Chemistry.....38
11	Acoustic wave generator.....45
12	Ceramic piezotransducer.....46

LIST OF FIGURES

<u>FIGURE</u>	<u>PAGE</u>
13	Acoustic resonator implemented for the experiment (a). Schematic configuration of an acoustic resonator with a single transducer (b). Reproduced with permission from Royal Society of Chemistry47
14	Syringe pump.....47
15	Far-field microscope integrated with the illumination system and computer screen.....49
16	Top view of the geometry of the micro-sized device (a). Zoom-in picture of the inlet section where the fluid is guided by the short channels before entering in the pillars region (b).....50
17	Computational domain.....52
18	Mesh convergence analysis. Line plots of p_1 (a), T_1 (b), v_1 (c), v_2 (d) for an increasing number of boundary layers.....66
19	Mesh convergence analysis. Line plots of p_1 (a), T_1 (b), v_1 (c), v_2 (d) , for an increasing number of nodes.....67
20	Mesh of the computational domain with $\#BL = 45$ and $d_{\text{mesh}} = 1.89 \mu\text{m}$ (a). Zoom-in on a single pillar to highlight the 45 boundary layers.....68
21	Color plots of the pscillating first-order fields of the fluid responce to the acoustic actuation of PDMS pillars with a vertical standing wave at a frequency $f = 30 \text{ kHz}$ and amplitude $l = 0.5 \mu\text{m}$: (a) pressure, (b) temperature (c) velocity v_170
22	Line plots along a vertical line in the bulk of the fluid of the first-order: (a) pressure, (b) temperture, (c) velocity.....72
23	Line plots along a vertical line in the gap between the pillars of the first-order: (a) Pressure, (b) temperature, (c) velocity.....73
24	Comparison between the numerical (a) and analytical (b) solution of the first order velocity.....76
25	Color plot of the first order velocity between two long and parallel walls.....77
26	Numerical and analytical solutions compared in the parallel walls configuration.....77
27	Color plot of the magnitude of the second-order velocity.....79

LIST OF FIGURES

<u>FIGURE</u>	<u>PAGE</u>
28	Color and vector plot (white arrows) of the second-order velocity between two pillars....79
29	Line plot of the slip streaming velocity outside the Stokes layer.....81
30	Color plot of the magnitude of the acoustic radiation force.....82
31	Vector plot of the acoustic radiation force in the vertical gap between two consecutive pillars.....83
32	Line plots of the average values of the first-order pressure (a), temperature (b) velocity (c), second-order velocity (d) respect to the pillars deflection.....85
33	Color plots of the magnitude of the second-order velocity for different values of the distance between the pillars: : (a) 60 μm , (b) 80 μm , (c) 100 μm , (d) 120 μm88
34	Vector plot of the second-order velocity for different values of the distance between the pillars: (a) 60 μm , (b) 80 μm , (c) 100 μm , (d) 120 μm90
35	Line plots of the minimum frequency for trapping particles of different sizes respect to the distance between the pillars for different flow rates: (a) 4 $\mu\text{l/min}$, (b) 6 $\mu\text{l/min}$, (c) 7 $\mu\text{l/min}$, (d) 8 $\mu\text{l/min}$93
36	Vector plots of the second-order velocity at $Q = 4 \mu\text{l/min}$, $f = 30 \text{ kHz}$: $d_{\text{plr}} < d_{\text{plr,crit}}$ (a) $d_{\text{plr}} > d_{\text{plr,crit}}$ (b).....95
37	Vector plot of the second-order velocity at $Q = 4 \mu\text{l/min}$, $d_{\text{plr}} > d_{\text{plr,crit}}$ and $f = 120 \text{ kHz}$96
38	Color plot of the second-order velocity adopting triangular pillars.....100

LIST OF ABBREVIATIONS

MATHEMATICAL OPERATORS

∂	partial derivative
$\nabla \cdot$	divergence operator
\mathbf{n}	outward pointing normal vector
ε	perturbation parameter
a	length scale
η	similarity variable
g	scale factor
ψ	stream function
b	monopole scalar function
\mathbf{B}	dipole vector function
δ	delta function
i	imaginary unit
$*$	conjugated operator

LIST OF ABBREVIATIONS (continued)

ACOUSTIC FIELD

f	frequency
ω	angular frequency
λ	wavelength
γ	acoustic damping factor
k	complex wave number
k_0	real wave number
x_c	characteristic length
$\langle X \rangle$	time-average over a period of oscillation
τ	period of oscillation
A, B	general harmonically-oscillating variables
U	solid wall oscillating velocity
U_0	solid wall oscillating velocity amplitude
l	acoustically-induced displacement amplitude

LIST OF ABBREVIATIONS (continued)

\mathbf{F}^{rad}	acoustic radiation force
f_1	monopole scattering coefficient
f_2	dipole scattering coefficient
H	thermal wave numbers function
G	Gorkov function

FLUID VARIABLES

ρ	density
ρ_0	zero-order density
ρ_1	first-order density
$\tilde{\rho}_1$	perturbed first-order density
ρ_{in}	incoming wave density
ρ_2	second-order density
$\tilde{\rho}_2$	perturbed second-order density

LIST OF ABBREVIATIONS (continued)

\mathbf{v}	velocity field
\mathbf{v}_0	zero-order velocity field
\mathbf{v}_1	first-order velocity field
v_{1x}	first-order velocity, x direction
v_{1y}	first-order velocity, y direction
$\tilde{\mathbf{v}}_1$	perturbed first-order velocity field
\mathbf{v}_{in}	incoming wave velocity
\mathbf{v}_2	second-order velocity field
v_{2x}	second-order velocity, x direction
v_{2y}	second-order velocity, y direction
$\tilde{\mathbf{v}}_2$	perturbed second-order velocity field
$\mathbf{v}_2^{\text{slip}}$	second-order slip velocity
\emptyset_1	first-order velocity potential
\emptyset_{\pm}	velocity potential unknown coefficients

LIST OF ABBREVIATIONS (continued)

ϕ_{in}	incoming wave velocity potential
ϕ_{sc}	scattered wave velocity potential
ϕ_{mp}	monopole velocity potential
ϕ_{dp}	dipole velocity potential
p	pressure
p_0	zero-order pressure
p_1	first-order pressure
\tilde{p}_1	perturbed first-order pressure
p_2	second-order pressure
\tilde{p}_2	perturbed second-order pressure
T	temperature
T_0	zero-order temperature
T_1	first-order temperature
\tilde{T}_1	perturbed first-order temperature

LIST OF ABBREVIATIONS (continued)

T_2	second-order temperature
\tilde{T}_2	perturbed second-order temperature
s	entropy
σ	stress tensor
\mathbf{F}^{drag}	Stokes drag force
μ_{b_f}	dynamic bulk viscosity
μ_f	dynamic viscosity
ν_f	kinematic viscosity
β	viscosity ratio
K_f	compressibility
c_{p_f}	specific heat capacity at constant pressure
c_{v_f}	specific heat capacity at constant volume
γ_f	specific heats ratio
α_f	thermal expansion coefficient

LIST OF ABBREVIATIONS (continued)

k_{th_f}	thermal conductivity
D_{th_f}	thermal diffusivity
c_f	speed of sound
δ_s	viscous boundary layer thickness
δ_{th}	thermal boundary layer thickness
k_{c_f}	compressional mode wave number
x_{c_f}	non-dimensional compressional mode wave number
k_{th_f}	thermal mode wave number
x_{th_f}	non-dimensional thermal mode wave number
k_{s_f}	shear mode wave number
x_{s_f}	non-dimensional shear mode wave number
γ	acoustic damping factor
Π_{s_f}	viscous damping factor
Π_{th_f}	thermal damping factor
Q_{tot}	volume flow rate injected in the channel

LIST OF ABBREVIATIONS (continued)

m_{tot}	mass flow rate injected in the channel
m_{section}	mass flow rate injected in the computational domain

PARTICLES VARIABLES

\mathbf{u}	velocity field
a_p	radius
κ_p	compressibility
ρ_p	density
$c_{p,p}$	specific heat capacity at constant pressure
α_p	thermal expansion coefficient
$k_{\text{th},p}$	thermal conductivity
$D_{\text{th},p}$	thermal diffusivity
c_p	longitudinal speed of sound
$c_{T,p}$	transverse speed of sound
$k_{c,p}$	compressional mode wave number
$x_{c,p}$	non-dimensional compressional mode wave number

LIST OF ABBREVIATIONS (continued)

k_{th_p}	thermal mode wave number
x_{th_p}	non-dimensional thermal mode wave number
k_{s_p}	shear mode wave number
x_{s_p}	non-dimensional shear mode wave number
Π_{th_p}	thermal damping factor
X_p	particle speed of sound parameter
χ_p	particle speed of sound parameter

CHANNEL GEOMETRY

w	channel width
L	channel length
h	channel height
$w_{section}$	computational domain width
$L_{section}$	computational domain length
d	distance between the pillars
r_{plr}	pillar radius

LIST OF ABBREVIATIONS (continued)

h_{plr}	pillar height
d_{mesh}	mesh size

SUMMARY

Handling with acoustic phenomena in microfluidic devices is an attractive capability for controlling microparticles and manipulating fluids at the micro-scale, with huge potential in medical research and bionengineering. In particular, the complex phenomena generating the forces acting on the particles and the acoustic streaming vortices are of high interest to accomplish these desired functions. In order to create innovative devices, acoustofluidic has been studied extensively in the recent years, with experimental and numerical approaches. The derived theoretical models and the software developement in the last decade, allow the numerical simulations to be able to reproduce well the experimental results. The aim of this work is to provide a computational analysis of the particles trapping in the streaming vortices generated by the oscillation of pillars arrays in the channel of a micro-device. This phenomenon has been observed in the experiments, but a numerical analysis is required in order to find the optimal design for the lab-on-a-chip system and to work at the best operative conditions for achieving particles trapping.

CHAPTER 1

INTRODUCTION

1.1 Background

The research on acoustic effects applied to microfluidics is of high interest for practical applications in medical diagnostics, pharmacology, biochemistry and life science. In particular, acoustic trapping allows immobilisation of cells and particles in a non-contact and non-invasive manner, it enables a fast formation of 3D cell clusters, it improves the particle-based bioassays and it facilitates interactions studies of both cells and particles. Applications of acoustic trapping in life science research are microscopy studies, incubation and washing of cells and enrichment of cells from dilute suspensions [1]. Moreover, the pressing need to design innovative and efficient devices have attracted many researchers to develop theoretical and experimental studies on the complex phenomena of acoustic waves propagation in micro-sized fluids. Different mechanisms are involved in the process of perturbing a fluid flow at the micro-scale and controlling the motion of particles in a micro-device with an external acoustic field. Propagation of acoustic waves in solid structures resulting in stresses, strains and damping in the channel walls [2], generation of sound waves in the fluid flow due to its small but non-negligible compressibility, non-linear phenomena arising due to the viscous dissipation of the acoustic energy in the fluid and the acoustophoretic motion of the particles [3] are all complex phenomena of high interest in acoustofluidic research. The physical process involves a fluid at the micro-scale flowing in a channel where the walls are forced to oscillate under the application of a perturbing

acoustic field emitted by a piezo-transducer. Particles of different nature and with different physical properties flow together with the fluid and the acoustic field is used to control their motion. In particular, particles manipulation is obtained with two well known phenomena arising in acoustofluidic: the acoustic streaming and the acoustic radiation force [3]. The first is the steady component of the fluid response due to the viscous dissipation of the acoustic energy in the bulk of the fluid and in the boundary layers near the walls [4], while the second results from the scattering of the harmonically-oscillating acoustic waves on the particles [5]. The particles response to these two acoustic effects depends on their size and physical properties such as density, compressibility, heat capacity, thermal expansion and thermal conductivity [6]. Moreover, changing the numerical values of these parameters, a transition from acoustic streaming to acoustic radiation force dominance in the particles movement is observed both in the experiments and in the numerical simulations [7].

Microparticles and cells handling in microfluidic devices are obtained also with other types of external fields such as electric, dielectric, optic and magnetic forces. Acoustic techniques have been also introduced in this scenario, and they have become an efficient strategy to achieve separation, focusing, concentration, removal, aggregation and trapping of microparticles such as biological cells or functionalized microbeads [8]. For example, acoustofluidic is a powerful technique for cells sorting and compared to other techniques, it is extremely convenient because it does not require a contact manipulation, it is cheap, easy to control and it has a high level of biocompatibility [9]. Moreover, the great advantage of their non-invasive nature makes the acoustofluidic systems very reliable to obtain homogeneous mixing. Examples are the bubble-based acoustic mixers [10],[11],[12] and the sharp-edge based micro-mixers [4],[13]. Mixing occurs due to the acoustically induced microvortices, generated by oscillating liquid or air bubbles in the first case and by the acoustic vibration of the sharp edges in the second one. On the other hand, the acoustic trapping is commonly obtained with a local

acoustic potential with a high gradient able to block the particles against the flow. The lateral component of the acoustic radiation force, perpendicular to the primary sound propagation direction and generated by the gradient of the acoustic potential, is used to counteract the Stokes drag force and immobilise the particles. Moreover, particles trapping can be achieved also with the bulk circulating flow of the acoustic streaming [1]. This thesis is addressed to study the second type of acoustic trapping. Using the same design adopted for deterministic lateral displacement (DLD) applications [14], an external acoustic field is imposed to force the pillars to vibrate harmonically. The oscillation of the pillars coupled with the viscous dissipation of the acoustic energy, generates velocity gradients in the viscous boundary layer resulting in the bulk vortices able to trap the particles. This phenomenon has been observed also in the experiments, where the trapping is obtained near the pillars when a critical frequency and critical voltage amplitude are set on the acoustic field generator. The aim of this work is to provide a numerical analysis of the acoustic effects in a microdevice where particles trapping is obtained using cylindrical pillars distributed in the channel in uniform and parallel arrays. The material used to fabricate the device is polydimethylsiloxane (PDMS), a soft polymer widely used in microfluidics applications to replace more rigid materials like silicon and glass. The particles adopted are polystyrene beads with different sizes; polystyrene is the material commonly used in both experimental and numerical analysis. In particular, we want to investigate the dependence of the critical frequency on many parameters such as the distance between the pillars, the flow rate imposed by the syringe pump, the oscillation amplitude and the particles size. Being the basic hydrodynamic behaviour of the fluid dictated by the motion of the pillars, these parameters significantly impact the generation of the streaming rolls around the pillars walls. For studying this problem, we adopt a numerical approach because experiments are too expensive and time consuming, while Computational Fluid Dynamics (CFD) is a relatively cheap and quick alternative, allowing the problem to be analysed

over a wide range of parameters simultaneously. Moreover, with a computational study we can obtain a deep understanding of the fluid response to the applied acoustic field, in order to enhance the knowledge of the complex physical behaviour of acoustic phenomena in fluids and improve the design of acoustofluidic devices for future biomedical applications in healthcare research.

1.2 Previous numerical studies of acoustofluidics

The complexity of the acoustofluidic problems and the pressing need to control them, have paved the way to advance theories and sophisticated numerical models with the aim to provide a robust mathematical formulation and computational analysis of sound waves propagation in microfluids. All the numerical models developed so far by many researchers, describe physical processes like the fluid response to the walls actuation with different types of waves (eg. surface acoustic waves (SAW), harmonic standing wave (HSW), standing surface acoustic waves (SSAW)), transmission of the acoustic waves through the channel material, acoustophoretic motion of the particles and efficient generation of streaming effects. The fundamental equations of acoustofluidics are described by Henrik Bruus in chapter 15 of the textbook 'Theoretical Microfluidics' [3]. Starting from the Navier-Stokes equations and the thermodynamic equation of state, and modelling the acoustic phenomena with the Nyborg perturbation theory, the Helmholtz equation governing the acoustic waves propagation in fluids is derived, both in the case of non-viscous and viscous damping. Then, the acoustic resonance of the harmonic behaviour of the fluid in a two-dimensional chamber is analysed, where comparison between numerical and experimental results are also provided. Finally, the equations describing the steady components of the fluid response are developed, together with the mathematical expressions of the

acoustic radiation force and the acoustic streaming. Henrik Bruus, together with Jonas Tobias Karlsen developed a theoretical analysis for describing the acoustic radiation force acting on a single spherical micro-sized particle, either a thermoviscous fluid droplet or a thermoelastic particle, flowing in a viscous and heat-conducting fluid medium [6]. The thermal effects are introduced to the former viscous model presented by Mikkel Settnes and Henrik Bruus [15], since the thermoviscous theory provides substantial effects on the acoustic radiation force when dealing with particles smaller than the thickness of the viscous and thermal boundary layers. Moreover, Bruus *et al.* presented a numerical study of the transition from streaming-induced drag to acoustic radiation force dominance of the acoustophoretic motion of the microparticles in a two-dimensional liquid-filled microchamber[7]. Computing the fluid response adopting the thermoviscous model, it is shown how the transition is a function of the geometry of the device, particles diameter and material's physical properties. In particular, the smallest particles are dominated by the acoustic streaming flow, while on the larger particles the acoustic radiation force results to be dominant. The same results are confirmed by Huang *et al.* in the numerical analysis of the acoustic motion of fluid and particles in confined and acoustically leaky system [16]. Furthermore, Huang *et al.* numerically demonstrated how controlling acoustic wavefront in microfluidic systems with waveguides of different shapes and geometry [17]. Giving a computational characterization of the complex field trajectories with defined pressure nodes in localized micro-chamber, it is illustrated how dynamically control the pressure field in order to obtain particles trapping and manipulation. Mao *et al.* elaborated a two-dimensional numerical model for describing the acoustophoretic motion of the particles in a microchannel excited by standing surface acoustic waves (SSAW) [18], in order to enhance the precision in matching the experimental results respect to the simple one-dimensional harmonic standing waves (HSW) model. Nama *et al.* proposed a numerical study of acoustophoretic motion of particles in a PDMS microchannel based on lithium

niobate substrate, acoustically actuated by surface acoustic wave (SAW) [19]. In this work, the PDMS walls were modeled with the impedance or lossy-wall boundary condition. This boundary condition is completely different from the hard-wall condition, used to model silicon or glass walls in bulk acoustic waves (BAW) systems. The impedance boundary condition allows to model a complete absorption of the acoustic wave energy in the PDMS, with no reflection in the air-wall interface. In the area of high interest of generating vortices around geometrical singularities, Huang *et al.* numerically investigated the streaming patterns around oscillating sharp edges [4]. The system was studied varying the geometrical characteristics of the channel such as the angle of the tips, the height of the sharp edges and the width of the channel. Streaming effects are also studied around the sharp-edges of an acoustically actuated micromotor placed in the middle of the channel [20]. The particles trajectories around the micromotor sharp tip were numerically computed, exhibiting a good agreement with the patterns observed in the experiments.

All the numerical models mentioned above are based on the Nyborg perturbation theory, for which the fluid response to an harmonic forcing is de-coupled in two separate sets of variables. The first-order fields refer to the oscillating acoustic response, while the second-order fields refer to the steady acoustic streaming [2]. The perturbation theory allows to overcome the challenging problem of solving the viscosus and compressible Navier-Stokes equations, where the presence of the non linear terms makes the solution problematic even with the modern computational tools [4]. According to this scheme, the flow fields after the walls actuation results in an harmonic and a steady perturbation to the fluid at rest. In acoustofluidic problems, the perturbation parameter is the ratio between the amplitude of the walls velocity and a frequency-based velocity. In this thesis the same procedure is adopted to solve the equations of motion of the fluid flow. Moreover, implementing the thermoviscous model for

a more precise analysis of the small particles behaviour, the thermodynamic heat transfer equation is introduced in the perturbation scheme.

CHAPTER 2

FUNCTIONS AND ACOUSTIC ACTUATION OF PILLARS IN MICROFLUIDIC DEVICES

2.1 Introduction

In this section it is discussed the the use of pillars arrays in microfluidic devices for different applications. Then, the analysis developed by Huang *et al* of the behaviour of PDMS pillars in a mixing acoustofluidic device is presented [21], in order to highlight the link between the acoustic actuation and the pillars deflection.

2.2 Background

Arrays of pillars distributed along a channel of a micro-device have been introduced in microfluidic stuides as an efficient technique to obtain different lab-on-a chip functions in a passive manner. In the deterministic lateral displacement (DLD) method, pillars are employed to separate millimetre, micrometre, and even sub-micrometers particles and cells in continuous flows. Applications are mostly in the medical field: separation of white blood cells (WBCs), red blood cells (RBCs), circulating tumor cells (CTCs) and platelets from blood [14]. Pillars are also used as hydrophobic barriers to create flow delay and pseudoturbulence in microcapillary flows, for enhancing the

sensitivity of lateral flow assays (LFAs) devices for point-of-care applications (POC). As a result, LFAs can be extended to a wider range of analytes, such as cancer biomarkers, DNA, toxins and metals [22].

Moreover, pillars are used as a passive strategy for achieving controlled droplets merging in many applications including sequential reactions, multiple step manipulation of cells and high-throughput bioassays [23]. Even if pillars-based microchannels consist in passive devices, the effect to external forces can be coupled to the pillars to enforce fluid handling capability and particles manipulation. The external fields can be either electric, dielectric, magnetic, gravitational and acoustic. Actuated pillars allow various processes like directional fluid transport, fluid mixing, controlling material deposition, organism alignment, sperm cell activation and moving micro-robots [20].

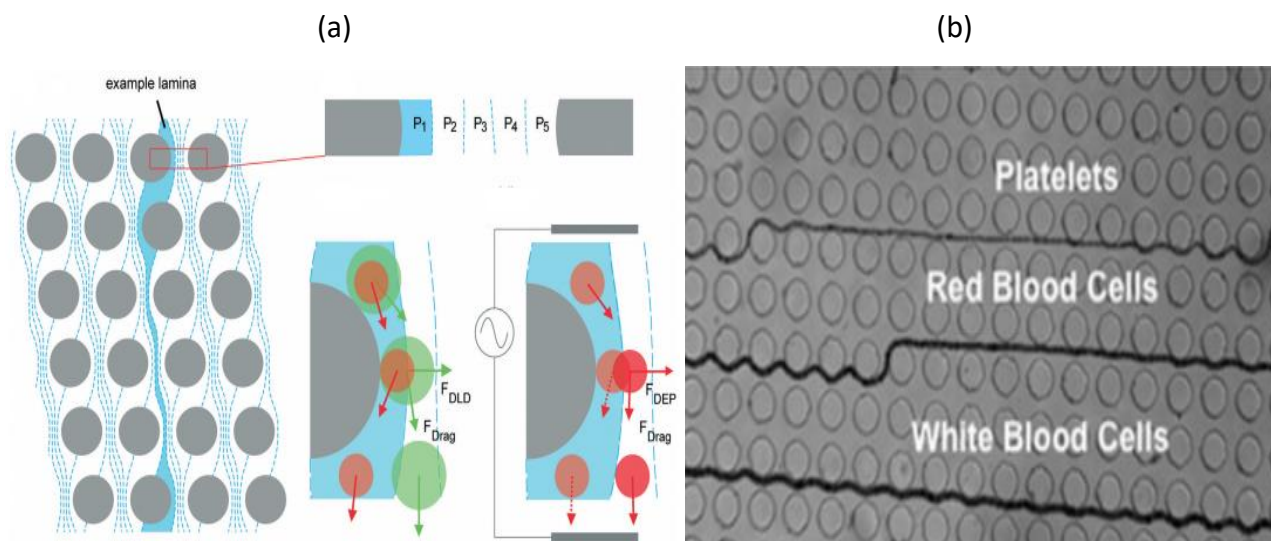


Figure 1: Scheme of the pillars used for Determinist Lateral Displacement application (a) and cells sorting in DLD microdevices (b). Reproduced with permission from Royal Society of Chemistry.

2.3 Acoustic actuation of cylindrical pillars

In this thesis the acoustically driven vibration of the pillars is used to generate acoustic streaming vortices, allowing an efficient particles and cells trapping. The acoustic actuation of pillars in a microfluidic device is an innovative technique, with huge future potentials in various lab-on-a-chip applications. Huang *et al* recently studied the acoustic actuation of PDMS cilia, for mixing DI water and fluorescent dye solutions. The actuation frequency and the imposed flow rate were respectively 4.6 kHz and 5 $\mu\text{l}/\text{min}$. [21].

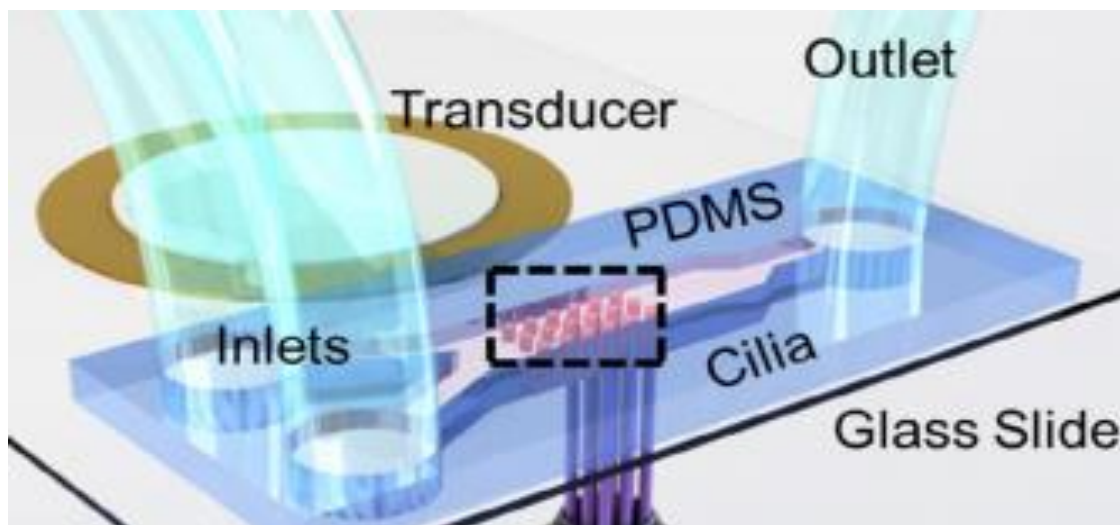


Figure 2: Acoustic actuation of PDMS cilia for fluid mixing in Huang *et al* micro-channel. Reproduced with permission from Institute of Physics Publishing.

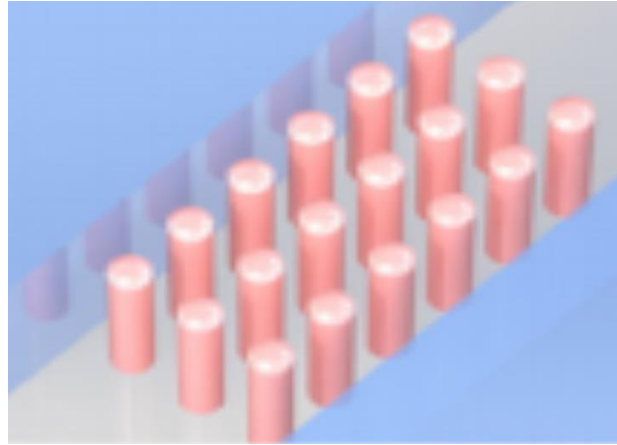


Figure 3: Uniform distribution of aligned pillars in the microchannel used by Huang *et al* . Reproduced with permission from Institute of Physics Publishing.

The oscillation's amplitude of the pillars is dictated by the voltage imposed on the acoustic field generator. Varying the values on the acoustic field generator from 20 V_{PP} to 140 V_{PP} , Huang *et al* found a linear relationship between the driving voltage and the pillars deflection. The amplitude was measured as the maximum distance of a point on the top of a cilium during one cycle of oscillation.

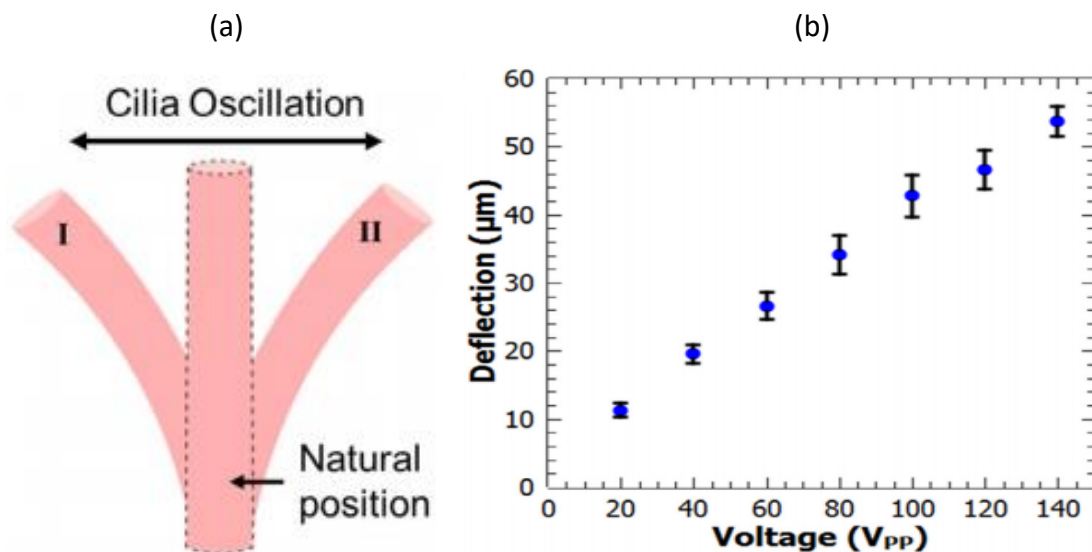


Figure 4: Acoustically driven oscillation of a PDMS cilia (a). Linear dependence of the cilia's deflection on the applied voltage (b). Reproduced with permission from Institute of Physics Publishing.

Due to its softness of PDMS, the pillars exhibited a deflection in the range of μm . Arranging the transducer in different positions, the cilia always oscillated in the same horizontal direction. Huang *et al* believed that the oscillation's direction is determined by the wave pattern on the glass substrate that the cilia are attached to. Moreover, with a variation of the applied frequency it was found a much lower oscillation magnitude. Furthermore, it was supposed that also the geometrical features of the cilia and the channel had some impacts on the deflection, nevertheless these parameter were maintained constant. In particular, increasing the channel height or the pillars diameter, an higher oscillation amplitude was expected, according to the theory of elasticity.

In this thesis, a similar acoustofluidic device but with a different purpose was analysed. Nevertheless, the results obtained by Huang *et al* allow to consider displacements in the range of μm for PDMS devices. This is is very important, since the pillars acoustic actuation was modeled with a velocity condition having the form of a standing wave:

$$v_{1x} = 0 \quad v_{1y} = \omega l e^{-i\omega t} \quad (2.1)$$

where ω and l are the angular frequency and the amplitude of the displacement.

Even if Huang *et al* estimated that the oscillation direction is independent from the the position of the transducer, in this work the deflection is imposed along the direction of propagation of the acoustic wave, emitted by the transducer perpendicular to the channels walls, while a zero displacement is set in the direction parallel to the channel, accordin to eq.[2.1]. This is a simplified assumption, since it does not consider the propagation of the sound wave in the chip structure as Huang *et al* did, but from the point of view of the numerical formulation, it mimics well the oscillation of the pillars.

CHAPTER 3

EQUATIONS OF ACOUSTOFLUIDICS

3.1 Introduction

In this chapter the theory of acoustofluidics is presented. Then, it is shown the derivation of the analytical solution of the fluid's acoustic response in the important configuration of the Rayleigh's third problem. The theoretical analysis described in this chapter was developed by Henrick Bruus in the textbook '*Theoretical Microfluidics*' [3].

3.2 Governing equations

The acoustofluidics equations are derived from the continuity and Navier-Stokes equations governing a fluid flow in a micro-channel, taking into account the effect of the fluid's compressibility and viscosity. When perturbing the equilibrium pressure in a compressible fluid with a time-harmonic forcing, sound waves can be generated in the fluid medium. Moreover, due to the dissipative nature of the fluid, the response to a time-harmonic forcing is generally not harmonic. The fluid's behaviour results in a coupling of a time-harmonic response, defined as acoustic response, and a slow steady remainder, defined as acoustic streaming. The acoustic streaming is driven by the momentum flux gradients induced by the acoustic energy flux dissipation. The dissipation arises in the fluid medium because of the bulk viscosity related to the internal friction due to the fluid's compressibility, and near

the solid walls due the dynamic viscosity related to the shear stress in the boundary layer. In the application studied in this thesis, the acoustic streaming is boundary layer driven, due to the friction between the fluid and the pillars distributed along the channel. The acoustic streaming is very important since it generates the Stokes drag force acting on particles suspended in the fluid. On the other hand, the scattering of the time-harmonic acoustic waves on the particles generates the acoustic radiation force which drives the acoustophoretic motion of the particle together with the Stokes drag force.

As a result, both the compressible and viscous contributions must be taken into account in the Navier-Stokes equations involved in acoustics problems. In order to derive the linear wave equation for the acoustic field generated in the fluid, the equations of motion are coupled with the thermodynamic equation of state expressing the pressure p in terms of the density ρ :

$$\partial_t \rho = -\nabla \cdot (\rho \mathbf{v}) \quad (3.1)$$

$$\rho \partial_t \mathbf{v} = -\nabla p - \rho \mathbf{v}(\nabla \cdot \mathbf{v}) + \mu_f \nabla^2 \mathbf{v} + \beta \mu_f \nabla(\nabla \cdot \mathbf{v}) \quad (3.2)$$

$$p = p(\rho) \quad (3.3)$$

The compressibility of the liquid gives rise to the viscosity ratio $\beta = \frac{\mu_{b_f}}{\mu_f} + \frac{1}{3}$ where μ_{b_f} is the second or bulk viscosity, and μ_f is the dynamic viscosity which. For the liquid water at 20 °C the values of the dynamic viscosity and viscosity ratio are:

$$\mu_f = 1.002 \text{ mPa s} \quad \mu_{b_f} = \frac{4}{3} \mu_f = 1.336 \text{ mPa s} \rightarrow \beta = \frac{5}{3} = 1.667$$

In the governing equations, all the external fields are neglected. Moreover, the heat transfer due to dissipation of the acoustic energy in the fluid is neglected. This leads to the simple viscous theory of

acoustofluidics. Nevertheless, in order to provide a more complete and precise framework of acoustic phenomena in fluids, H.Bruus and J.T. Karlsen derived the thermo-viscous theory, where the heat transfer equation is introduced:

$$\partial_t T + (\nabla \cdot \mathbf{v})T = D_{\text{th}_f} \nabla^2 T + \frac{\mu_f}{2\rho c_{p_f}} (\nabla \cdot \mathbf{v} + (\nabla \cdot \mathbf{v})^T)^2 \quad (3.4)$$

where D_{th_f} is the thermal diffusivity $D_{\text{th}_f} = \frac{k_{\text{th}_f}}{\rho c_{p_f}}$. For water at 20 °C, the thermal diffusivity is

$$D_{\text{th}_f} = \frac{0.597 \text{ W m}^{-1} \text{ K}^{-1}}{998 \text{ kg m}^{-3} \times 4182 \text{ J kg}^{-1} \text{ K}^{-1}} = 1.43 \times 10^{-7} \text{ m}^2 \text{ s}^{-1}$$

The thermoviscous theory is necessary to model the particles smaller than the thickness of the thermal boundary layer. In this chapter, it is discussed only the viscous theory and the thermal effects are neglected.

3.3 The Nyborg's perturbation method

The system of non-linear partial differential equations [3.1-3] is solved with the Nyborg's perturbation theory. This is the method applied in all the acoustofluidic applications, since it is a natural way to describe the physical behaviour of the fluid after the acoustic actuation. The acoustic time-harmonic response corresponds to the first-order perturbation, while the acoustic streaming is a second order effect. Perturbing the flow fields to the second-order:

$$\rho = \rho_0 + \varepsilon \tilde{\rho}_1 + \varepsilon^2 \tilde{\rho}_2 + O(\varepsilon^3) \quad (3.5)$$

$$\mathbf{v} = \mathbf{v}_0 + \varepsilon \tilde{\mathbf{v}}_1 + \varepsilon^2 \tilde{\mathbf{v}}_2 + O(\varepsilon^3) \quad (3.6)$$

$$p = p_0 + \varepsilon \tilde{p}_1 + \varepsilon^2 \tilde{p}_2 + O(\varepsilon^3) \quad (3.7)$$

The symbol \sim refers to the perturbation fields. The small non-dimensional parameter ε is evaluated according to the specific problem taken into account. In general $\varepsilon = U_0/\omega a$ where U_0 is the small velocity amplitude of the vibrating walls, ω the angular frequency of the acoustic field and a a length scale. The parameter ε must be $\ll 1$ in order to apply the perturbation scheme.

The zero-order terms are related to unperturbed state of the fluid at rest. Re-writing the first and second-order terms in the following way:

$$\rho_1 = \varepsilon \tilde{\rho}_1 \quad \mathbf{v}_1 = \varepsilon \tilde{\mathbf{v}}_1 \quad p_1 = \varepsilon \tilde{p}_1 \quad (3.8)$$

$$\rho_2 = \varepsilon^2 \tilde{\rho}_2 \quad \mathbf{v}_2 = \varepsilon^2 \tilde{\mathbf{v}}_2 \quad p_2 = \varepsilon^2 \tilde{p}_2 \quad (3.9)$$

Eq. (3.1-3) become:

$$\rho = \rho_0 + \rho_1 + \rho_2 \quad (3.10)$$

$$\mathbf{v} = \mathbf{v}_0 + \mathbf{v}_1 + \mathbf{v}_2 \quad (3.11)$$

$$p = p_0 + p_1 + p_2 \quad (3.12)$$

The zero-order terms assume constant values. In particular, the unperturbed velocity is zero since the fluid is considered quiescent before the acoustic actuation.

3.4 The first-order problem

In this paragraph the acoustic wave equations describing the time-harmonic component of the fluid response are derived. Since the acoustic response is a first-order perturbation, the second-order terms are not introduced in this analysis. The first-order perturbation leads to:

$$\rho = \rho_0 + \rho_1 \quad (3.13)$$

$$\mathbf{v} = \mathbf{v}_1 \quad (3.14)$$

$$p = p_0 + c_f^2 \rho_1 \quad (3.15)$$

where the last equation is derived from the isentropic expansion of the equation of state :

$$p(\rho) = p_0 + \left(\frac{\partial p}{\partial \rho}\right)_s \rho_1 = p_0 + c_f^2 \rho_1 \quad (3.15)$$

being c_f the isentropic speed of sound in the fluid medium.

Combining the equations and neglecting the products of first-order terms, the first-order continuity and Navier-Stokes equations assume the following expressions:

$$\partial_t \rho_1 = -\rho_0 \nabla \cdot \mathbf{v}_1 \quad (3.16)$$

$$\rho_0 \partial_t \mathbf{v}_1 = -c_f^2 \nabla \rho_1 + \mu_f \nabla^2 \mathbf{v}_1 + \beta \mu_f \nabla (\nabla \cdot \mathbf{v}_1) \quad (3.17)$$

Inserting eq. (3.17) into the time derivative of eq.(3.16):

$$\partial_t^2 \rho_1 = -\nabla \cdot (\rho_0 \partial_t \mathbf{v}_1) = c_f^2 \nabla^2 \rho_1 - (1 + \beta) \mu_f \nabla^2 (\nabla \cdot \mathbf{v}_1) \quad (3.18)$$

the wave equation for ρ_1 is obtained:

$$\partial_t^2 \rho_1 = c_f^2 \left[1 + \frac{(1+\beta)\mu_f}{\rho_0 c_f^2} \partial_t \right] \nabla^2 \rho_1 \quad (3.19)$$

The first-order field is assumed to have the form of a standing wave:

$$\rho_1(x, y, z, t) = \rho_1(x, y, z) e^{-i\omega t} \quad (3.20)$$

where $\omega = 2\pi f$ is the angular frequency and f the frequency of the acoustic field. The harmonic- time dependence is expressed by the complex phase $e^{-i\omega t}$, where the physical meaning is related to the real part. The wave equation becomes:

$$\omega^2 \rho_1 = -c_f^2 \left[1 - i \frac{(1+\beta)\mu_f \omega}{\rho_0 c_f^2} \right] \nabla^2 \rho_1 = -[1 - i2\gamma] c_f^2 \nabla^2 \rho_1 \quad (3.21)$$

γ is the acoustic damping factor:

$$\gamma(\omega) = \frac{(1+\beta)\mu_f \omega}{2\rho_0 c_f^2} \quad (3.22)$$

This important parameter describes the damping of the acoustic wave, due to the viscous dissipation of the acoustic energy in the fluid medium. The bulk and the boundary layer dissipations are taken into account, since both β and the dynamic viscosity μ_f enter in expression (3.22). For water at 25 °C and frequencies at the order of kHz the acoustic damping factor is small $\gamma \approx 10^{-2} < 1$. The smallness of γ allow to use the approximation $[1 - i2\gamma] \approx [1 + i\gamma]^{-2}$ in eq.(3.21). As a result:

$$\nabla^2 \rho_1 = - \left[\frac{\omega}{c_f} (1 + i\gamma) \right]^2 \rho_1 = -[k_0(1 + i\gamma)]^2 \rho_1 \quad (3.23)$$

which is the Helmholtz equation for damped acoustic waves:

$$\nabla^2 \rho_1 = -k^2 \rho_1 \quad (3.24)$$

with a complex wave number k and a real wave number k_0 :

$$k = k_0 (1 + i\gamma) \quad (3.25)$$

$$k_0 = \frac{\omega}{c_f} \quad (3.26)$$

Considering a standing wave also for the pressure and the velocity:

$$p_1(x, y, z, t) = p_1(x, y, z) e^{-i\omega t} = c_f^2 \rho_1(x, y, z) e^{-i\omega t} \quad (3.27)$$

$$\mathbf{v}_1(x, y, z, t) = \mathbf{v}_1(x, y, z) e^{-i\omega t} \quad (3.28)$$

the Helmotz equations for these fields are:

$$\nabla^2 p_1 = -k^2 p_1 \quad (3.29)$$

$$\nabla^2 \phi_1 = -k^2 \phi_1 \quad (3.30)$$

The velocity potential ϕ_1 generalized to the viscous case assumes the following expression:

$$\phi_1(x, y, z, t) = -i \frac{1}{\omega \rho_0 (1+i\gamma)^2} p_1(x, y, z) e^{-i\omega t} = -i \frac{c_f^2}{\omega \rho_0 (1+i\gamma)^2} \rho_1(x, y, z) e^{-i\omega t} \quad (3.31)$$

In this way it is possible to define the first-order velocity:

$$\mathbf{v}_1 = \nabla \phi_1 \quad (3.32)$$

also in the viscous case (normally eq. (3.32) is valid only in the inviscid case $\mu_f = 0$).

3.5 The second-order problem

Inserting the fields (3.5-7) perturbed at the second-order into the governing equations (3.1-3) and neglecting the products of the second-order terms, the second-order governing equations are derived:

$$\partial_t \rho_2 = -\rho_0 \nabla \cdot \mathbf{v}_2 - \nabla \cdot (\rho_1 \mathbf{v}_1) \quad (3.33)$$

$$\rho_0 \partial_t \mathbf{v}_2 = -\nabla p_2 + \mu_f \nabla^2 \mathbf{v}_2 + \beta \mu_f \nabla (\nabla \cdot \mathbf{v}_2) - \rho_1 \partial_t \mathbf{v}_1 - \rho_0 (\mathbf{v}_1 \cdot \nabla) \mathbf{v}_1 \quad (3.34)$$

$$p_2 = c_f^2 \rho_2 + \frac{1}{2} (\partial_\rho c_f^2)_0 \rho_1^2 \quad (3.35)$$

The second-order fields are not solved in the μs time-scale, but they are studied considering a time-average over a complete period of oscillation:

$$\langle X \rangle = \frac{1}{\tau} \int_0^\tau dt X(t) \quad (3.36)$$

Thus, the products of the first-order solutions can be considered as source terms in the time-averaged second-order equations. The time-averaged continuity and Navier-Stokes equations are:

$$\rho_0 \nabla \cdot \langle \mathbf{v}_2 \rangle = -\nabla \cdot \langle \rho_1 \mathbf{v}_1 \rangle \quad (3.37)$$

$$\mu_f \nabla^2 \langle \mathbf{v}_2 \rangle + \beta \mu_f \nabla (\nabla \cdot \langle \mathbf{v}_2 \rangle) - \nabla \langle p_2 \rangle = \langle \rho_1 \partial_t \mathbf{v}_1 \rangle + \rho_0 \langle (\mathbf{v}_1 \cdot \nabla) \mathbf{v}_1 \rangle \quad (3.38)$$

Being non-zero the time-average of the first-order products, $\langle \mathbf{v}_2 \rangle \neq 0$ and $\langle p_2 \rangle \neq 0$. Thus, the fluid response to the acoustic actuation has also a steady second-order order component given by $\langle \mathbf{v}_2 \rangle$ and

$\langle p_2 \rangle$. The presence of the source first-order terms in eq.(3.37-38) is the mathematical explanation of the time-independent acoustic streaming.

Neglecting the viscosity, (3.38) becomes:

$$\nabla \langle p_2 \rangle = -\langle \rho_1 \partial_t \mathbf{v}_1 \rangle - \rho_0 \langle (\mathbf{v}_1 \cdot \nabla) \mathbf{v}_1 \rangle \quad (3.39)$$

and combining (3.39) with the first-order equations, the pressure $\langle p_2 \rangle$ can be expressed as:

$$\langle p_2 \rangle = \frac{1}{2} \kappa_f \langle p_1^2 \rangle - \frac{1}{2} \rho_0 \langle \mathbf{v}_1^2 \rangle \quad (3.40)$$

where the compressibility of the fluid $\kappa_f = \frac{1}{\rho_0 c_f^2}$ has been introduced.

3.6 Acoustic Streaming and Acoustic Radiation Force

The streaming velocity $\langle \mathbf{v}_2 \rangle$ gives rise to the Stokes drag force acting on the particles flowing in the channel:

$$\mathbf{F}^{\text{drag}} = 6\pi\mu_f a_p (\langle \mathbf{v}_2 \rangle - \mathbf{u}) \quad (3.41)$$

where a_p and \mathbf{u} are respectively the particles radius and velocity.

Moreover, $\langle p_2 \rangle$ is the source of the acoustic radiation force generated by the scattering of the acoustic waves on the particles. The acoustophoretic motion is not resolved on the μs time scale of the imposed sound wave, but it is the result of the radiation force averaged over a full oscillation cycle. Thus, only the time average values $\langle \quad \rangle$ are taken into account in deriving the formula of the acoustic radiation

force. The instantaneous acoustic radiation force is calculated as the surface integral of the fluid stress $\boldsymbol{\sigma}$ acting on the particle surface and the momentum flux tensor $\rho\mathbf{v}\mathbf{v}$ entering the fluid volume through the surface $\partial\Omega(t)$ encompassing the particle:

$$\begin{aligned}\mathbf{F}^{\text{rad}} &= \left\langle \int_{\partial\Omega} [\boldsymbol{\sigma} - \rho\mathbf{v}\mathbf{v}] \cdot \mathbf{n} \, dS \right\rangle = - \int_{\partial\Omega} [\langle p_2 \rangle + \rho_0 \langle \mathbf{v}_1 \mathbf{v}_1 \rangle] \cdot \mathbf{n} dS = \\ &= - \int_{\partial\Omega} \left[\frac{1}{2} \kappa_f \langle p_1^2 \rangle - \frac{1}{2} \rho_0 \langle \mathbf{v}_1^2 \rangle + \rho_0 \langle \mathbf{v}_1 \mathbf{v}_1 \rangle \right] \cdot \mathbf{n} dS\end{aligned}\quad (3.42)$$

It is important to remind that the expression (3.40) of $\langle p_2 \rangle$ is obtained for $\mu_f = 0$. This procedure is approximately correct for particles significantly larger than the thickness δ_s of the viscous-acoustics boundary layer. Nevertheless, in order to take into account particles smaller than δ_s , some numerical corrections must be introduced to the model. Moreover, further corrections are added with the thermoviscous model, for calculating \mathbf{F}^{rad} acting on particles smaller than the thickness of the thermal boundary layer δ_{th} .

The drag and radiation force, numerically derived from the acoustic streaming $\langle \mathbf{v}_2 \rangle$ and the second order pressure $\langle p_2 \rangle$, are determinant in driving the motion of the particles in a microfluidic device. The motion of the particles is governed by the Newton's second law:

$$m_p \mathbf{a}_p = \mathbf{F}^{\text{drag}} + \mathbf{F}^{\text{rad}} = 6\pi\mu_f a_p (\langle \mathbf{v}_2 \rangle - \mathbf{u}) + \mathbf{F}^{\text{rad}} \quad (3.43)$$

where m_p and \mathbf{a}_p are the mass and acceleration of the particles. In many acoustofluidics applications, the inertia of the particles can be neglected and the velocity of the particles can be calculated as:

$$\mathbf{u} = \langle \mathbf{v}_2 \rangle + \frac{\mathbf{F}^{\text{rad}}}{6\pi\mu_f a_p} \quad (3.44)$$

3.7 Acoustic actuation of two planar and parallel walls

In this section it is derived the analytical solution for the acoustic response of a fluid enclosed between two planar and parallel walls at a distance L and forced to vibrate by the application of an acoustic field. This geometrical configuration refers to the Rayleigh's third problem, which is of high interest in acoustofluidics. First, this is one of the configurations where a numerical description of the acoustic streaming was derived by Lord Rayleigh. Then, it is representative of the acoustic behaviour of the fluid the frontal area of a microchannel when the two lateral walls are actuated by a piezo transducer.

The walls are placed parallel in the yz plane at $x = -L$ and $x = +L$. To mimic the effect of the transducer, the oscillation is modeled with the condition on the fluid's first-order velocity at the the walls:

$$v_{1x}(-L, t) = -\omega l e^{-i\omega t} \quad v_{1x}(+L, t) = +\omega l e^{-i\omega t} \quad U = U_0 e^{-i\omega t} \quad (3.45)$$

where $\omega = 2\pi f$ is the angular frequency and l is the amplitude of the oscillation. The ultrasound actuation of microfluidic channels is commonly studied in the MHz regime, thus here it is considered $f = 1$ MHz. The amplitude of the oscillation must be small respect the distance between the walls $l \ll L$. In silicon structures, a typical values of l is 1 nm. In PDMS devices, deflection in the μm regime are allowed, as it will be discussed in the next chapter. Being l small, the walls are considered to remain in a fixed position, while the velocity in contact with them oscillates harmonically according to eq.(3.45).

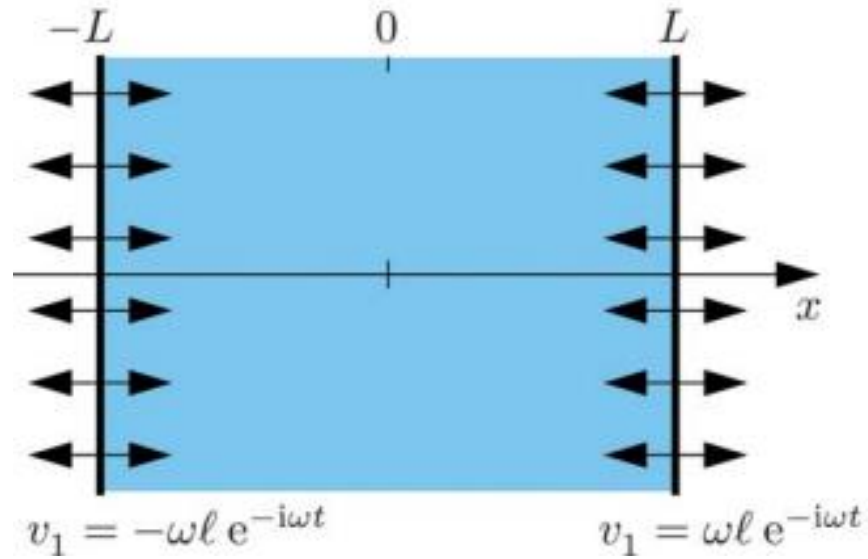


Figure 5: Acoustic actuation of two planar and parallel walls with a standing wave. Reproduced with permission from Royal Society of Chemistry.

The acoustic velocity potential for the viscous fluid has the expression (3.31):

$$\phi_1(x, t) = -i \frac{1}{\omega \rho_0 (1 + i\gamma)^2} p_1(x) e^{-i\omega t}$$

with $\mathbf{v}_1 = \nabla \phi_1$ or $\nabla \times \mathbf{v}_1 = 0$. The acoustic wave is considered a 1D wave travelling in the x direction.

The wave equation for ϕ_1 :

$$\nabla^2 \phi_1 = -k^2 \phi_1$$

can be solved writing ϕ_1 as a superposition of a pair of counter-propagating waves with a complex wave number $k = k_0 (1 + i\gamma)$ and unknown coefficients ϕ_+ and ϕ_- to be determined:

$$\phi_1(x, t) = [\phi_+ e^{ikx} + \phi_- e^{-ikx}] e^{-i\omega t} \quad (3.46)$$

The corresponding first-order velocity is :

$$v_{1x} = \partial_x \phi_1(x, t) = ik[\phi_+ e^{ikx} + \phi_- e^{-ikx}] e^{-i\omega t} \quad (3.47)$$

Introducing the anti-phase conditions (3.45):

$$\phi_+ = \phi_- = -\frac{\omega l}{2k \sin(kL)} \quad (3.48)$$

Then, the expression of \mathbf{v}_1 becomes:

$$v_{1x} = \omega l \frac{\sin(kx)}{\sin(kL)} e^{-i\omega t} \approx \omega l \frac{\sin(k_0 x) + i\gamma k_0 x \cos(k_0 x)}{\sin(k_0 L) + i\gamma k_0 L \cos(k_0 L)} e^{-i\omega t} \quad (3.49)$$

The Taylor expansion of kL around $k_0 L$ is allowed considering $\gamma k_0 L \ll 1$. The minima of \mathbf{v}_1 are given by the off-resonance condition:

$$\gamma \ll |k_0 L - n\pi| \rightarrow \text{off-resonance condition} \quad (3.50)$$

which means that $k_0 L$ differs sufficiently from integer multiples of π . Under the condition (3.50) the imaginary part of the denominator can be neglected and the velocity becomes:

$$v_{1x} \approx \omega l \frac{\sin(k_0 x)}{\sin(k_0 L)} e^{-i\omega t} \rightarrow \text{off-resonance velocity} \quad (3.51)$$

with a small amplitude:

$$|v_{1x}| \approx \omega l = \frac{\omega l}{c_f} c_f \approx 10^{-7} c_f \rightarrow \text{off-resonance velocity amplitude} \quad (3.52)$$

where $\omega \approx 10^7 \text{ rad s}^{-1}$, $l = 0.1 \text{ nm}$ and $c_f \approx 10^3 \text{ ms}^{-1}$.

The points where a standing wave exhibits the minimum amplitude of the off-resonance condition are called nodes. On the other hand the maxima are located at anti-nodes and given for the resonance condition:

$$k_0 = k_n = n \frac{\pi}{L} \quad n = 1, 2, 3, \dots \rightarrow \text{resonance condition} \quad (3.53)$$

The resonance condition is achieved when the frequency is tuned to its resonance value:

$$\omega = \omega_n = c_f k_n = n \frac{\pi c_f}{L} \quad n = 1, 2, 3, \dots \quad (3.54)$$

In the nodes at the n th resonance $\sin(k_n L) = 0$ and $\cos(k_n L) = (-1)^n$, so the acoustic velocity becomes:

$$v_{1x} \approx (-1)^n \omega l \left[-\frac{i}{n\pi\gamma} \sin\left(n\pi \frac{x}{L}\right) + \frac{x}{L} \cos\left(n\pi \frac{x}{L}\right) \right] e^{-i\omega t} \rightarrow \text{resonance velocity} \quad (3.55)$$

with an amplitude:

$$|v_{1x}| \approx \frac{1}{n\pi\gamma} \frac{\omega_n l}{c_f} c_f \approx \frac{1}{n} 10^{-2} c_n \rightarrow \text{resonance velocity amplitude} \quad (3.56)$$

which is $\left(\frac{1}{n}\right) \times 10^5$ times larger than the off-resonance component.

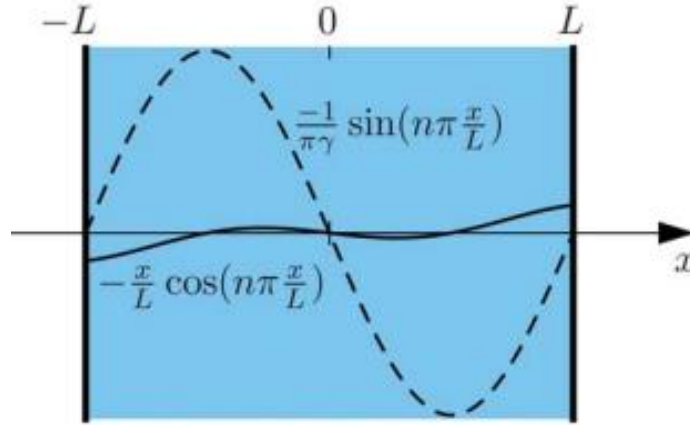


Figure 6: Acoustic response at the resonance condition of a fluid enclosed between two planar and parallel oscillating walls. Reproduced with permission from Royal Society of Chemistry.

The acoustic response of the fluid at the resonance condition has two components. A small component, proportional to $\frac{x}{L} \cos\left(\pi \frac{x}{L}\right)$ which obeys to the oscillatory condition (3.45) and it has an amplitude ωl at the walls. On the other hand, the large component, proportional to $\frac{1}{\pi \gamma} \sin\left(\pi \frac{x}{L}\right)$, is an eigenmode of the system and it has a zero velocity at the walls since it obeys to the hard-wall condition:

$$\mathbf{n} \cdot \nabla p_1 = 0 \quad (3.57)$$

This boundary condition is applied when a fluid interfaces an infinite hard wall which does not yield the fluid acoustic velocity. Thus, the normal velocity of the fluid is zero at the wall, which gives a zero pressure gradient according to eq.(3.57). In order to perform a more accurate analysis, the damping of the acoustic wave in the air gap between the transducer and the device and the acoustic impedance of the channel's walls should be taken into account. Nevertheless, the oscillatory condition in eq.(3.45) is a good approximation.

In conclusion, the fluid between two parallel walls actuated by a piezo transducer exhibits a sinusoidal behaviour described by eq.(3.49). Even if this is the ideal case of two infinite parallel walls, it can be considered to be a good model for describing the fluid behaviour in a system characterized by the presence of oscillating solid structures.

CHAPTER 4

ACOUSTIC STREAMING

4.1 Introduction

The aim of this chapter is to provide a qualitative description of the acoustic streaming in microfluidic systems. The informations are taken from the papers 'Acoustofluidics 13: Analysis of acoustic streaming by perturbation method' [24] and 'Acoustofluidics 14: Applications of acoustic streaming in microfluidic devices' [25]. Moreover, it is presented the theoretical analysis developed by Hermann Schlichting in the textbook '*Boundary-Layer Theory*' [26] about the acoustic streaming arising when a cylindrical body performs an oscillating motion in a fluid at rest.

4.2 Physical process

The acoustic streaming is the phenomenon for which a steady flow is generated in a viscous fluid in the presence of an external harmonic forcing. The acoustic energy flux carried by the incoming acoustic wave is attenuated due to the viscous dissipation of the fluid. The energy flux dissipation induces momentum flux gradients which drive acoustic streaming.

Streaming flows have different natures according to the mechanism behind the viscous attenuation of the acoustic wave generated in the fluid. There are two regions where the dissipation takes place: the bulk and the boundary layer. Dissipation in the bulk is due to the friction generated by the compressible nature of the fluid. Dissipation in the boundary layer is due to the Reynolds stress between the fluid and the oscillating fluid's enclosure or solid structures in the medium. When the dissipation of the acoustic energy occurs in the boundary layer, streaming effects are driven also in the bulk. The first type of streaming is known as 'Eckart streaming' or 'quartz wind' and it occurs only in systems where the fluid channel or the chamber parallel to the direction of the wave is of a scale > 1 mm. The second type is the famous 'Schlichting-Rayleigh streaming' and it arises in devices where the microchannel is very small compared to the wavelength of the acoustic wave. In acoustofluidic systems, acoustic streaming is boundary layer-driven. Moreover, in the particular device studied in this thesis, the acoustic streaming is generated by the oscillating PDMS pillars in the fluid channel.

For what concerns the boundary layer driven streaming, a steep velocity gradient exists in the boundary layer due to the non-slip condition at the wall. Therefore, the boundary layer dissipation is stronger than the dissipation carried in the bulk. As a result of the steep velocity gradients, the fluid inside the thin shear-wave boundary layer or Stokes layer, is forced to vibrate rotationally and rotational vortices are generated. The rotational boundary layer vorticity is termed inner boundary layer streaming or 'Schlichting streaming'. Carrying through the edge of the Stokes layer, this non-linear steady flow generates the steady streaming in the bulk of the fluid. Therefore, the fluid exhibits a rotating behaviour both in the Stokes layer and in the bulk of the fluid. On the other hand, the flow outside the boundary layer is not subjected to any non-slip condition, resulting in an irrotational vorticity. The irrotational streaming within the bulk of the fluid is named outer boundary layer

streaming or 'Rayleigh streaming'. The edge of the Stokes layer can be considered as the transition line from the rotational to the irrotational streaming of the viscous flow.

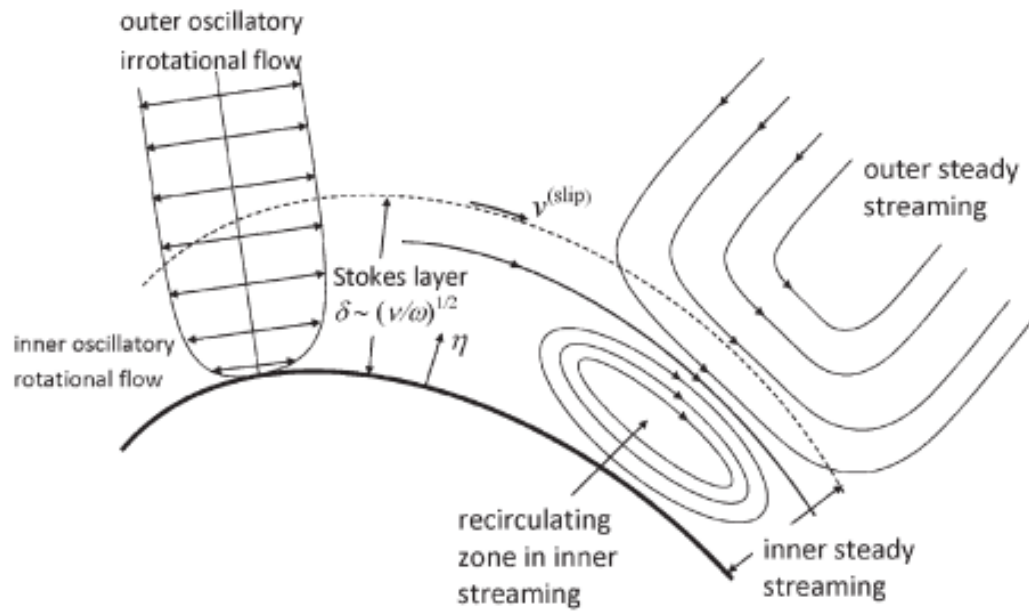


Figure 7: Scheme of the Rayleigh-Schlichting streaming near an oscillating wall. Reproduced with permission from Royal Society of Chemistry.

The thickness of the Stokes layer is:

$$\delta_s = \sqrt{\frac{2\nu_f}{\omega}} \quad (4.1)$$

where ν_f is the kinematic viscosity and ω the angular frequency of the acoustic wave propagating in the fluid.

4.3 Acoustic streaming between two infinite and parallel oscillating plates

The Schlichting-Rayleigh streaming is studied in the Rayleigh's third problem. This is the case where the acoustic streaming is generated by the vibration of a fluid enclosure. Standing sound waves between two plates with a length of $\lambda/2$ at a distance h are generated in the fluid by the small vertical oscillation of the walls induced by an incoming acoustic field. λ is the wavelength of the acoustic wave.

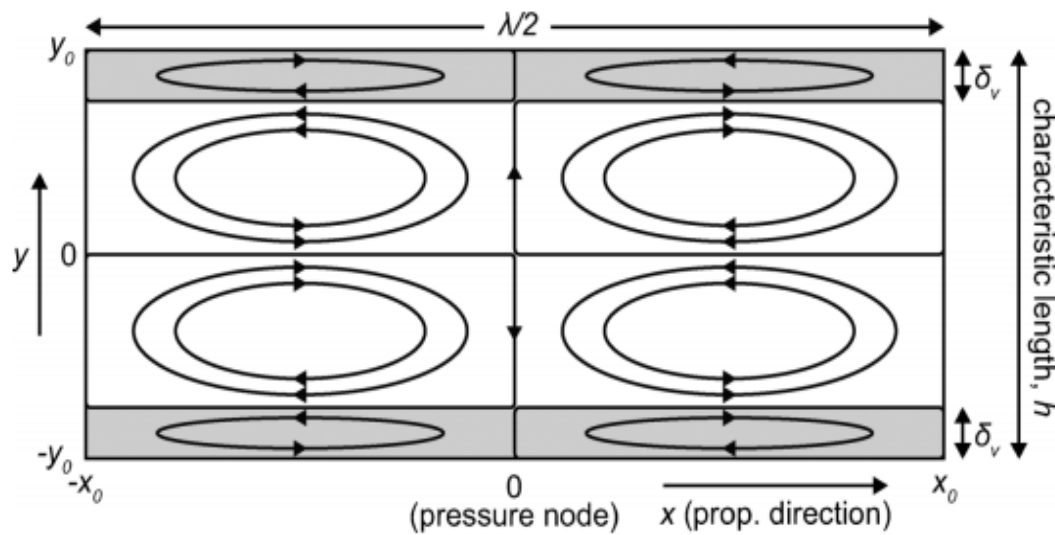


Figure 8: Scheme of the Rayleigh-Schlichting streaming in the third Rayleigh's problem. Reproduced with permission from Royal Society of Chemistry.

In the case of a standing wave parallel to the surface, the viscous dissipation results in a steady momentum flux typically oriented from the pressure antinodes to the pressure nodes close to the solid boundary. According to Landau and Lifshitz the boundary layer driven acoustic streaming is significant under the condition:

$$\lambda \gg h \gg \delta_s \quad (4.2)$$

The Rayleigh's streaming is more pronounced for chambers with length scales that are fractions of the wavelength. $\lambda/2$ which is widely used in acoustofluidic devices actuated with frequencies in the MHz regime, for which λ has the order of 1 mm.

4.4 Acoustic streaming in a cylindrical oscillating body in a fluid at rest

Another situation where acoustic streaming takes place, is the oscillation of a solid body in a fluid medium. Hermann Schlichting studied the acoustic streaming generated by the harmonic oscillation of a cylindrical body in a fluid at rest:

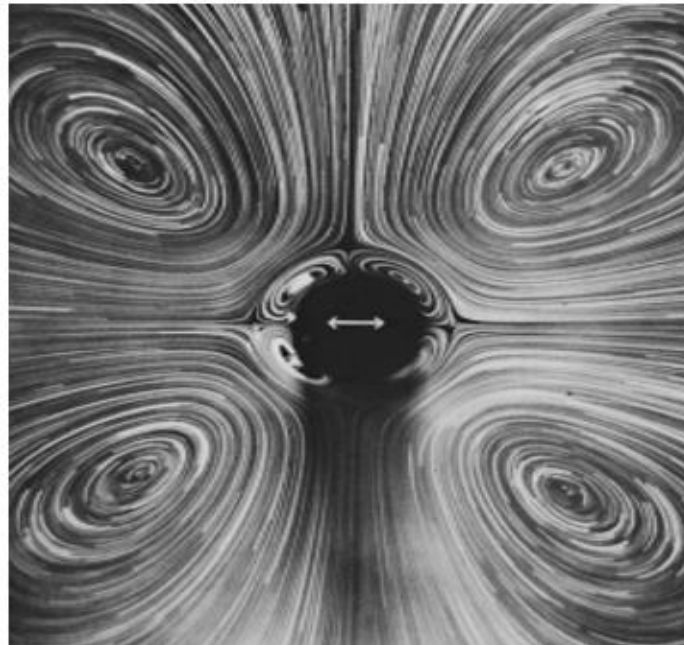


Figure 9 : Rayleigh-Schlichting streaming in an oscillating cylinder in a fluid at rest. Reproduced with permission from Royal Society of Chemistry.

This theory derived by H.Schlichting is relevant in this work, where the micro-channel is characterized by arrays of cylindrical pillars distributed along the channel and excited by the piezotransducer. We present here the main points of the Schlichting's theory.

Assuming a time-harmonic motion of the cylindrical body in the fluid, with a velocity:

$$U(x, t) = U_0(x)e^{i\omega t} \quad (4.3)$$

in order to derive an analytical expression for the slip velocity outside the Stokes layer, he solved the equation of the non-steady boundary layer along with the boundary conditions:

$$\frac{\partial \rho}{\partial t} + \rho \left(\frac{\partial u}{\partial x} + \frac{\partial v}{\partial y} \right) = 0 \quad (4.4)$$

$$\frac{\partial u}{\partial t} + u \frac{\partial u}{\partial x} + v \frac{\partial u}{\partial y} = -\frac{1}{\rho} \frac{\partial p}{\partial x} + \nu \frac{\partial^2 u}{\partial y^2} \quad (4.5)$$

$$y = 0 : \quad u = U_w(t) \quad v = 0 \quad (4.6)$$

$$y = \infty : \quad u = U(x, t) \quad (4.7)$$

using two numerical techniques developed for the boundary layers analysis: the theory of the successive approximations and the method of the similar solutions. For simplicity, the equations are shown using the same notation of Schlichting's textbook. In order to be coherent with the notation used in this thesis:

$$U(x, t) \leftrightarrow v_{1x}(x, t) \quad U_0(x) \leftrightarrow v_{1x}(x) \quad u \leftrightarrow v_{2,x} \quad v \leftrightarrow v_{2,y}$$

u and v are respectively the components of the velocity parallel and perpendicular to the wall. In particular it is assumed the component normal to wall smaller respect to the parallel component and the rate of change across the surface of the boundary layer larger than the rate of change in the direction of the flow:

$$v \ll u \quad \frac{\partial}{\partial x} \ll \frac{\partial}{\partial y} \quad (4.8)$$

Along with the theory of the successive approximations, the parallel component is de-coupled in two approximations:

$$u(x, y, t) = u_1(x, y, t) + u_2(x, y, t) \quad (4.9)$$

allowing a simplification of the differential equations [4.4-5]. The method of the similar solutions introduces the *similarity transformation* of the y direction into:

$$\eta = \frac{y}{g} \quad (4.10)$$

where $g = \sqrt{\frac{\nu_f}{\omega}}$ is the scale factor proportional to the boundary layer thickness. Then, the

components u and v of the velocity are calculated as the derivatives:

$$u = \frac{\partial \psi}{\partial y} \quad v = -\frac{\partial \psi}{\partial x} \quad (4.11)$$

of the stream function ψ . ψ is expressed in terms of an unknown function $f(\eta)$ to be determined imposing the boundary conditions at the wall and outside the boundary layer. Schlichting found the following expression for the slip velocity at the edge of the boundary layer:

$$u^{\text{slip}}(x) = -\frac{3}{4\omega} r_{\text{plr}} k \sin(4r_{\text{plr}} k x) \quad (4.12)$$

where r_{plr} is the radius of the cylinder and $k = \frac{2\pi}{\lambda}$ is the wave number. Therefore, in the numerical simulation we expect the sinusoidal behaviour expressed by eq.(4.12) of the streaming velocity outside the boundary layer $\mathbf{v}_2^{\text{slip}}$ in the direction of the flow.

CHAPTER 5

ACOUSTIC RADIATION FORCE

5.1 Introduction

The acoustic radiation force is the acoustically-induced force that governs the particles motion together with the Stokes drag force in acoustofluidic systems. The particles motion due to the radiation force is called acoustophoresis [5]. The acoustic radiation force is physically generated by the scattering on the particle of the acoustic wave propagating in the fluid medium. The derivation of the analytical expression of the acoustic radiation force acting on an incompressible and compressible particle in an ideal and inviscid fluid, was studied respectively in 1934 by King [28] and in 1955 by Yosioka and Kawasima [28]. A generalization of their work was provided in 1962 by Gorkov [29], but in the limited case of ideal fluids and particles with a radius $a_p \ll \lambda$. Moreover, Doinikov [30-32], Danilov and Mironov [33] provided a theoretical scheme for calculating the acoustic radiation force in thermoviscous fluids, but only in the limits $\delta_s, \delta_{th} \ll a_p \ll \lambda$ and $a_p \ll \delta_s, \delta_{th} \ll \lambda$. However, in lab-on-a-chip applications for particles trapping, separation and levitation, working with frequencies in the range of MHz, the previous constraints are not respected, since $\delta_s, \delta_{th} \sim a_p \ll \lambda$. For instance, in water at 2 MHz, $\delta_s = 0.4 \mu m$ and $\delta_{th} = 0.2 \mu m$, thus the acoustic radiation force is not well described for nanometer and micrometer-sized particles [6]. H. Bruus and M. Settnes derived a more general theory of arbitrary boundary layer thickness respect to the particles size, in the adiabatic limit where thermal

effects were not introduced [15]. However, also the thermal boundary layers significantly affect the acoustic radiation force exerted on the particles. Therefore, J.T. Karlsen and H. Bruus developed a more complete theoretical framework including the thermal effects and extending the analysis to compressible solid particles, either droplets and elastic particles, for which the viscous and elastic shear stress must be taken into account. The analysis is valid in the limit $\delta_s, \delta_{th}, a_p \ll \lambda$, with no restrictions on δ_s, δ_{th} and a_p [6].

In this section, we present first the main points of theoretical procedure developed by H. Bruus and J.T. Karlsen for calculating the general expression of the acoustic radiation force acting on a compressible, spherical, micrometre-sized particle. Then, the numerical corrections for including the thermoviscous effects are provided.

5.2 The general equation

The acoustic radiation force is due to the acoustic response of the fluid and it is not involved in the streaming phenomena, thus, only the first-order fields are taken into account. A small particle, *i. e.* $a_p \ll \lambda$ of density ρ_p and compressibility κ_p in an acoustically-perturbed fluid can be considered as a weak point-scatterer of the acoustic waves. The velocity potential ϕ_1 of the acoustic wave can be splitted into the potentials for the incoming wave ϕ_{in} and for the scattered wave propagating away from the particle ϕ_{sc} :

$$\phi_1 = \phi_{in} + \phi_{sc} \quad (5.1)$$

So, the acoustic velocity and pressure are:

$$\mathbf{v}_1 = \nabla \phi_{\text{in}} + \nabla \phi_{\text{sc}} \quad (5.2)$$

$$p_1 = i\rho_0\omega\phi_1 = i\rho_0\omega\phi_{\text{in}} + i\rho_0\omega\phi_{\text{sc}} \quad (5.3)$$

The acoustic radiation force can be calculated as the surface integral of the time-averaged second order pressure $\langle p_2 \rangle$ and the momentum flux tensor $\rho_0 \langle \mathbf{v}_1 \mathbf{v}_1 \rangle$ at a fixed surface outside the oscillating sphere, as it has been shown in chapter 3:

$$\mathbf{F}^{\text{rad}} = - \int_{\partial\Omega} [\langle p_2 \rangle + \rho_0 \langle \mathbf{v}_1 \mathbf{v}_1 \rangle] \cdot \mathbf{n} dS = - \int_{\partial\Omega} \left[\frac{1}{2} \kappa_f \langle p_1^2 \rangle - \frac{1}{2} \rho_0 \langle \mathbf{v}_1^2 \rangle + \rho_0 \langle \mathbf{v}_1 \mathbf{v}_1 \rangle \right] \cdot \mathbf{n} dS \quad (5.4)$$

Since no body forces are involved, any fixed surface enclosing the particle experiences the same force.

As far as the scattering theory analysis is concerned, it is convenient to choose a far field region $r \gg \lambda$ (dashed line with red arrows) rather than a near-field region $r \ll \lambda$ (full line and green arrows

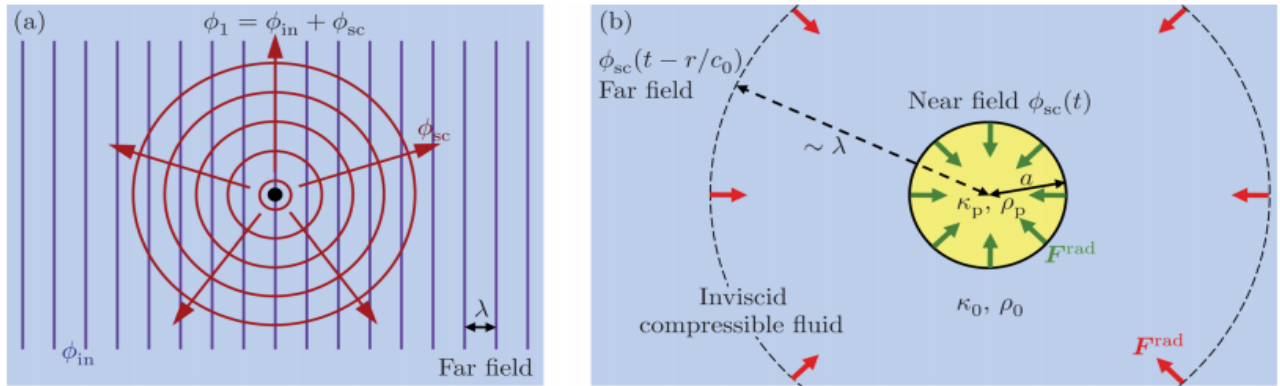


Figure 10 : Far field region $r \gg \lambda$, where the potential ϕ_1 is the sum of the incoming and scattered potentials (a). The scattered potential in the far and near field (b). Reproduced with permission from Royal Society of Chemistry.

In the scattering theory, the scattered field ϕ_{sc} from a point scatterer at the centre of a coordinate system is described as a time-retarded multipole expansion. In the far-field region, the monopole and dipole components are dominant:

$$\phi_{sc} \approx \phi_{mp} + \phi_{dp} \quad (5.5)$$

where the general relationships of ϕ_{mp} and ϕ_{dp} are:

$$\phi_{mp}(\mathbf{r}, t) = \frac{b\left(t - \frac{r}{c_f}\right)}{r} \quad (5.6)$$

$$\phi_{dp} = \nabla \cdot \left[\frac{\mathbf{B}\left(t - \frac{r}{c_f}\right)}{r} \right] \quad (5.7)$$

where b and \mathbf{B} are respectively a scalar and a vector function of the retarded argument $t - \frac{r}{c_f}$. In the first-order scattering theory ϕ_{sc} must be proportional to the incoming field ϕ_{in} . Since the only scalar and vector fields of concern are ρ_{in} and \mathbf{v}_{in} , $b \sim \rho_{in}$ and $\mathbf{B} \sim \mathbf{v}_{in}$. As a result, the scattered field in the far-field is:

$$\phi_{sc} = -f_1 \frac{a_p^3}{3\rho_0} \frac{\partial_t \rho_{in}\left(t - \frac{r}{c_f}\right)}{r} - f_2 \frac{a_p^3}{2} \nabla \cdot \left(\frac{\mathbf{v}_{in}\left(t - \frac{r}{c_f}\right)}{r} \right) \quad \text{for } r \gg \lambda \quad (5.8)$$

The particle radius a_p , the unperturbed density ρ_0 and the time derivative are introduced to have the correct physical dimension m^2s^{-1} of ϕ_{sc} . $\frac{1}{3}$ and $\frac{1}{2}$ are used for convenience related to the calculations.

The most important role is played by the two dimensionless scattering coefficients f_1 and f_2 , named respectively monopole and dipole scattering coefficients. f_1 is the coefficient in the monopole scattering potential ϕ_{mp} from a stationary sphere in the incoming density wave ρ_{in} , while f_2 is the coefficient in the dipole scattering potential ϕ_{dp} from an incompressible sphere moving with a velocity \mathbf{u} in the incoming velocity wave \mathbf{v}_{in} .

Expanding eq. (5.4) in terms of the incoming and scattered acoustic field, the i th component of the acoustic radiation force is:

$$F_i^{\text{rad}} = - \int_{\partial\Omega} \left\{ \left[\frac{c_f^2}{\rho_0} \langle \rho_{\text{in}} \rho_{\text{sc}} \rangle - \rho_0 \langle v_k^{\text{in}} v_k^{\text{sc}} \rangle \right] \delta_{ij} + \rho_0 \langle v_i^{\text{in}} v_j^{\text{sc}} \rangle + \rho_0 \langle v_i^{\text{sc}} v_j^{\text{in}} \rangle \right\} \cdot n_j \, da \quad (5.9)$$

Applying the Gauss theorem, introducing the vector potential of the scattered field ϕ_{sc} and after some manipulations:

$$F_i^{\text{rad}} = - \int_{\Omega} d\mathbf{r} \rho_0 \langle v_i^{\text{in}} \left(\partial_j^2 \phi_{\text{sc}} - \frac{1}{c_f^2} \partial_t^2 \phi_{\text{sc}} \right) \rangle \quad (5.10)$$

where $\partial_j^2 - \frac{1}{c_0^2} \partial_t^2$ is the D'Alembert operator acting on ϕ_{sc} . Since ϕ_{sc} is a sum of a monopole and a dipole terms, the D'Alembert operator can be written as delta function distribution $\delta(\mathbf{r})$ of the resulting fields ρ_{in} and \mathbf{v}_{in}

$$\partial_j^2 \phi_{\text{sc}} - \frac{1}{c_f^2} \partial_t^2 \phi_{\text{sc}} = f_1 \frac{4\pi a_p^3}{3\rho_0} \partial_t \rho_{\text{in}} \delta(\mathbf{r}) + f_2 2\pi a_p^3 \nabla \cdot [\mathbf{v}_{\text{in}} \delta(\mathbf{r})] \quad (5.11)$$

As a result (37f) becomes:

$$F_i^{\text{rad}} = - \int_{\Omega} d\mathbf{r} \rho_0 \langle v_i^{\text{in}} \left(f_1 \frac{4\pi a_p^3}{3\rho_0} \partial_t \rho_{\text{in}} \delta(\mathbf{r}) + f_2 2\pi a_p^3 \nabla \cdot [\mathbf{v}_{\text{in}} \delta(\mathbf{r})] \right) \rangle \quad (5.12)$$

After further calculations, the final general expression for the acoustic radiation force is obtained:

$$\mathbf{F}^{\text{rad}} = - \frac{4\pi}{3} a_p^3 \left[\frac{1}{2} \kappa_f \text{Re}[f_1^* p_{\text{in}}^* \nabla p_{\text{in}}] - \frac{3}{4} \rho_0 \text{Re}[f_2^* \mathbf{v}_{\text{in}}^* \nabla \mathbf{v}_{\text{in}}] \right] \quad (5.13)$$

In the special case of a standing wave $\phi(\mathbf{r}, t)_{\text{in}} = \phi_k(t) e^{-i\omega t}$, eq.(5.13) becomes:

$$\mathbf{F}^{\text{rad}} = - \frac{4\pi}{3} a_p^3 \nabla \cdot \left[\frac{1}{2} \text{Re}[f_1] \kappa_f \langle p_{\text{in}}^2 \rangle - \frac{3}{4} \text{Re}[f_2] \rho_0 \langle \mathbf{v}_{\text{in}}^2 \rangle \right] \quad (5.14)$$

Eq. (5.13-14) is the general expression for the acoustic radiation force acting on a particles of radius $a_p \ll \lambda$. Usually, the first-order fields are used instead of the incoming wave. Thus, eq.(5.14) becomes:

$$\mathbf{F}^{\text{rad}} = - \frac{4\pi}{3} a_p^3 \left[\frac{1}{2} \kappa_f \text{Re}[f_1^* p_1^* \nabla p_1] - \frac{3}{4} \rho_0 \text{Re}[f_2^* \mathbf{v}_1^* \nabla \mathbf{v}_1] \right] \quad (5.15)$$

and in the special case of a standing wave:

$$\mathbf{F}^{\text{rad}} = -\frac{4\pi}{3} a_p^3 \nabla \cdot \left[\frac{1}{2} \text{Re}[f_1] \kappa_f \langle p_1^2 \rangle - \frac{3}{4} \text{Re}[f_2] \rho_0 \langle \mathbf{v}_1^2 \rangle \right] \quad (5.16)$$

5.3 The thermoviscous model of the acoustic radiation force

The thermoviscous effects enter in eq.(5.16) through the analytical expression of the monopole and dipole scattering coefficients f_1 and f_2 . The thermoviscous theory allows to take into account the effects of the thermal gradients and the viscous gradients respectively inside the thermal and viscous boundary layer. The thickness of the boundary layers are:

$$\delta_{\text{th}} = \sqrt{\frac{2D_{\text{th},f}}{\omega}} \quad \delta_s = \sqrt{\frac{2\nu_f}{\omega}} \quad (5.17)$$

Important parameters for describing the thermoviscous theory are the compressional, thermal and shear mode wave numbers. For the fluid:

$$k_{c,f} = \frac{\omega}{c} \left[1 + \frac{i}{2} [\Pi_{s,f} + (\gamma - 1) \Pi_{\text{th},f}] \right] \quad (5.18)$$

$$k_{\text{th},f} = \frac{(1+i)}{\delta_{\text{th}}} \left[1 + \frac{i}{2} (\gamma - 1) (\Pi_{s,f} - \Pi_{\text{th},f}) \right] \quad (5.19)$$

$$k_{s,f} = \frac{(1+i)}{\delta_s} \quad (5.20)$$

and the particle:

$$k_{c,p} = \frac{\omega}{c} \left[1 + \frac{i}{2} (\gamma - 1) \chi_p \Pi_{t,p} \right] \quad (5.21)$$

$$k_{\text{th},p} = \frac{(1+i)}{\delta_{\text{th}}} \frac{1}{\sqrt{1-X_p}} \left[1 + \frac{i}{8} \frac{\gamma^2 \Pi_{\text{th},p}}{(1-X_p)} \right] \quad (5.22)$$

$$k_{s_p} = \frac{\omega}{c_{T_p}} \quad (5.23)$$

The corresponding non-dimensional form is obtained multiplying by the particle size a_p . For the fluid:

$$x_{c_f} = a_p k_{c_f} \quad x_{th_f} = a_p k_{th_f} \quad x_{s_f} = a_p k_{s_f} \quad (5.24)$$

and the particle

$$x_{c_p} = a_p k_{c_p} \quad x_{th_p} = a_p k_{th_p} \quad x_{s_p} = a_p k_{s_p} \quad (5.25)$$

Π_{s_f} , Π_{th_f} , Π_{th_p} are the viscous and thermal damping factor for the fluid and the particle. These parameters represent the viscous and thermal dissipation of the acoustic energy respectively due to the propagation in the fluid and the scattering on the particle of the acoustic wave.

$$\Pi_{s_f} = \frac{(1+\beta)v_f\omega}{c_f^2} \quad \Pi_{th_f} = \frac{D_{th_f}\omega}{c_f^2} \quad \Pi_{th_p} = \frac{D_{th_p}\omega}{c_p^2} \quad (5.26)$$

X_p and χ_p are the particle speed of sound parameters:

$$X_p = (\gamma_p - 1)(1 - \chi_p) \quad (5.27)$$

$$\chi_p = 1 - \frac{4}{3} \frac{c_{T_p}^2}{c_p^2} \quad (5.28)$$

where c_{T_p} and c_{p_p} are the transverse and longitudinal speed of sound of the particle.

We introduce the thermal wave numbers function:

$$H(x_{th_f}, x_{th_p}) = \frac{1}{x_{th_f}^2} \left[\frac{1}{1 - ix_{th_f}} - \frac{1}{\tilde{k}_{th}} \frac{\tan x_{th_p}}{\tan x_{th_p} - x_{th_p}} \right]^{-1} \quad (5.29)$$

and the Gorkov function:

$$G(x_{s_f}) = \frac{3}{x_{s_f}} \left(\frac{1}{x_{s_f}} - i \right) \quad (5.30)$$

Then, we introduce the non-dimensional compressibility, density, specific heat, thermal expansion coefficient and thermal conductivity

$$\tilde{\kappa} = \frac{\kappa_p}{\kappa_f} \quad (5.31)$$

$$\tilde{\rho}_0 = \frac{\rho_p}{\rho_0} \quad (5.32)$$

$$\tilde{c}_p = \frac{c_{p-p}}{c_{p-f}} \quad (5.33)$$

$$\tilde{\alpha} = \frac{\alpha_p}{\alpha_f} \quad (5.34)$$

$$\tilde{k}_{th} = \frac{k_{th-p}}{k_{th-f}} \quad (5.35)$$

According to the thermoviscous theory developed by H. Bruus and T.J. Karlsen [6], the monopole and dipole scattering coefficients have the following expressions:

$$f_1^* = \frac{1 - \tilde{\kappa} + 3(\gamma_f - 1) \left[\left(1 - \frac{\tilde{\alpha}}{\tilde{\rho}_0 \tilde{c}_p} \right) \left(1 - \frac{\chi_p \tilde{\alpha}}{\tilde{\rho}_0 \tilde{c}_p} \right) - \frac{4}{3} \frac{\chi_p \tilde{\alpha} \tilde{\kappa}}{\tilde{c}_p} \frac{c_{T_p}^2}{c_f^2} \left(1 - \frac{\tilde{\alpha}}{\tilde{\rho}_0 \tilde{c}_p \tilde{\kappa}} \right) \right] H(x_{th_f}, x_{th_p})}{1 + 4(\gamma_f - 1) \frac{\chi_p \tilde{\alpha}^2}{\tilde{\rho}_0 \tilde{c}_p^2} \frac{c_{T_p}^2}{c_f^2} H(x_{th_f}, x_{th_p})} \quad (5.36)$$

$$f_2^* = \frac{2(\tilde{\rho}_0 - 1)[1 - G(x_{s-f})]}{2\tilde{\rho}_0 + 1 - 3G(x_{s-f})} \quad (5.37)$$

Introducing these coefficients into the general equation of the acoustic radiation force, it is possible to introduce the effects of the thermal and viscous boundary layers into the numerical models .

CHAPTER 6

EXPERIMENTAL SET-UP

6.1 Introduction

In this section, it is provided a brief description of the tools used in the experiments. Even if this thesis is concerned on a numerical analysis, the experiment is fundamental in order to validate the computational results. The aim of the experiment is to verify that the polystyrene particles are trapped in the small vortices generated near the pillars when the acoustic field is actuated. The components of the experimental set-up are: the wave generator, the piezotransducer, the acoustic resonator, the syringe pump and the microscope.

6.2 Instruments used in the experiment

Acoustic wave generator



Figure 11: Acoustic wave generator

The acoustic wave generator allows to broadcast different types of signal to the piezotransducer: sine, square, ramp, pulse, noise and arb waves. In order to reproduce a standing wave, 'sine wave' must be selected. Moreover, it is possible to adjust the frequency and the voltage amplitude to the maximum level prescribed by the machine. The generator used in our work is a RIGOL DG1022, with a maximum frequency of 25 MHz and a maximum voltage of 20 V_{pp} . This voltage generate micrometer displacements in the PDMS walls.

Ceramic piezo-transducer

Piezoelectric materials are used extensively for generating vibrations in microfluidic devices through a conversion of an electric signal into a mechanical motion. This method has several advantages. First, it is possible to generate waves of complex shapes and frequencies with a high level of repeatability, simply by tuning the signal generator. Then, adjusting the transducer, the device can be excited with various modes of waves. In order to take these advantages, a material with a high level of piezoelectricity charge constant is required. The best candidates are the piezoelectric ceramics, widely used to fabricate the transducers in acoustofluidics applications [34]. The large part of the ultrasonic transducers work at the resonant frequency, for which the emitted signal is at the maximum magnitude.

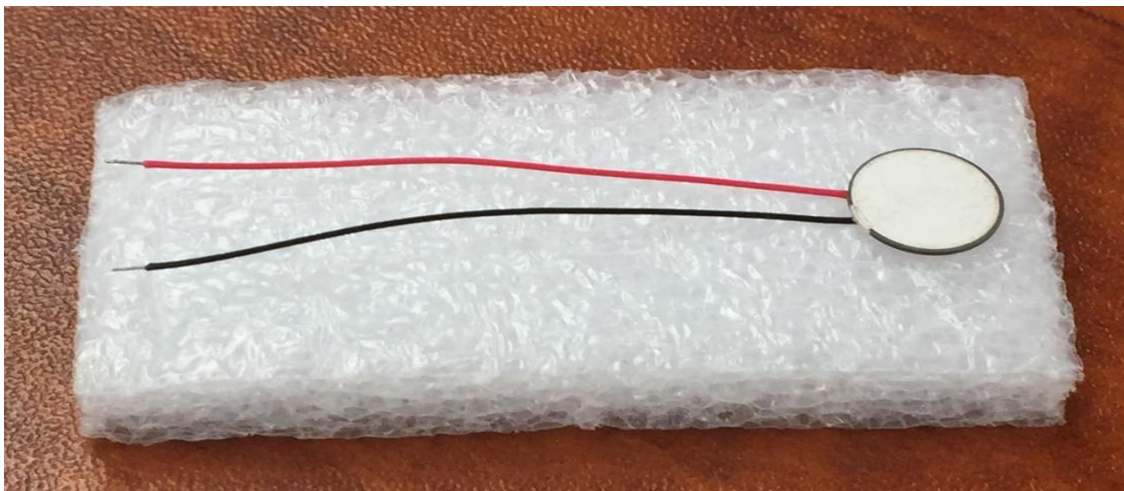


Figure 12: Ceramic piezotransducer

The black and red electrodes are connected to the cable of the acoustic wave generator, in order to transmit the acoustic signal to the piezotransducer.

Acoustic resonator:

The acoustic resonator is a microfluidic device actuated by an external acoustic field. A common way to fabricate an acoustic resonator is to create a compartment where one wall of the resonator has a piezoceramic transducer glued to two layers of glass or metal, while the opposite wall behaves as a passive reflector [35]. In our device we used glass and PDMS respectively for the basement and the coupling layer.

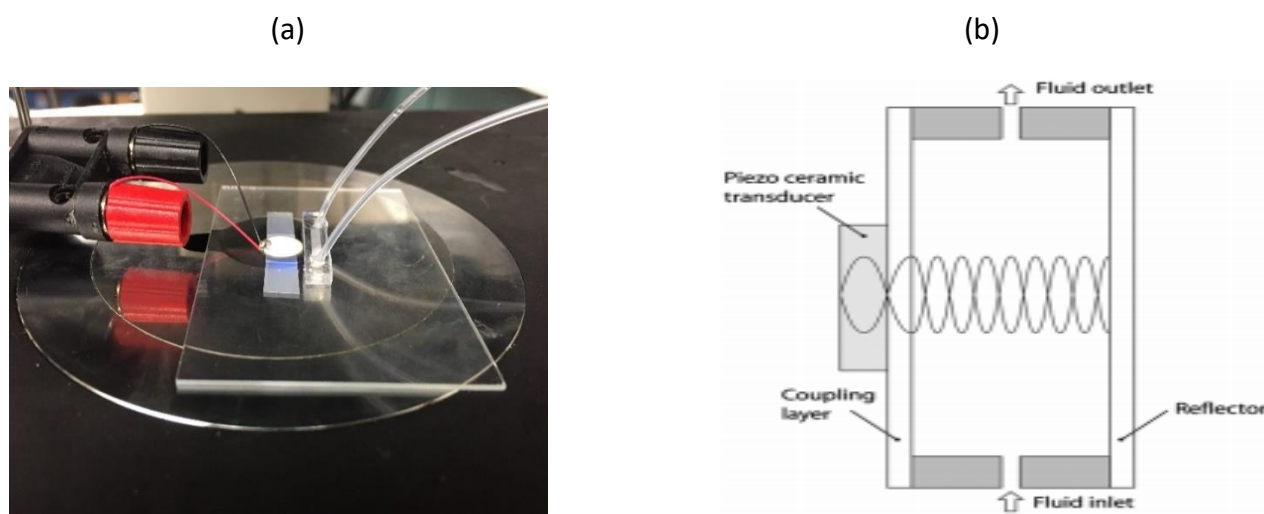


Figure 13: Acoustic resonator implemented for the experiment (a). Schematic configuration of an acoustic resonator with a single transducer (b). Reproduced with permission from Royal Society of Chemistry.

Syringe pump



Figure 14: Syringe pump

The syring pump allows to inject a micro-sized fluid flow in the device chamber through a thin plastic tube, which is connected to the inlet section. A second plastic tube is connected to the outlet, in order to drain out the fluid at the exit of the channel. On the machine it is possible to select the velocity or the flow rate of the fluid pumped in the device. The unit of measure of the velocity and the flow rate are respectively $\mu\text{m}/\text{min}$ and $\mu\text{l}/\text{min}$.

Microscope

The optical microscope is an essential tool for experimental investigations of objects with a size range from few millimeters down to the nanometer. The microscope used in the experiment is a wide-field microscope with an integrated illumination system. In this type of instrument, the entire field of view is uniformly illuminated with a light and the picture can be observed through the eyepiece and by a camera. The main components are: the illumination system, the objective, optional filters, the imaging detector (eye or camera). The integrated illumination system is provided for the most advanced microscopes and it is used to illuminate the non-entirely luminous specimens in a uniform way. Moreover, it is possible to control the illuminated area, the light intensity and the solid angle under which the specimen is illuminated. The uniform illumination is provided by a series of optical elements and a collector-condenser, aligned to obtain a maximum defocus on the image of the light source in the specimen plane [36].



Figure 15: Far-field microscope integrated with the illumination system and a computer screen

A computer screen is also integrated to visualize the device monitored by the camera. This is a very useful tool which allow to record the video of the particles movement in the channel.

CHAPTER 7

NUMERICAL SIMULATION

7.1 Introduction

The work presented here is based on the numerical simulation “Acoustic Streaming in a Microchannel Cross Section”, available on the web-site of COMSOL Multiphysics. This simulation relies on the thermoviscous theory of acoustofluidic presented by Bruus *et al* [7] and it investigates the 2D cross section of a microfluidic channel. Following the same approach, in this work it is simulated the longitudinal section of the particles-trapping micro-device used in the experiments.

7.2 Geometry

We consider a microfluidic device with the following geometry:

(a)



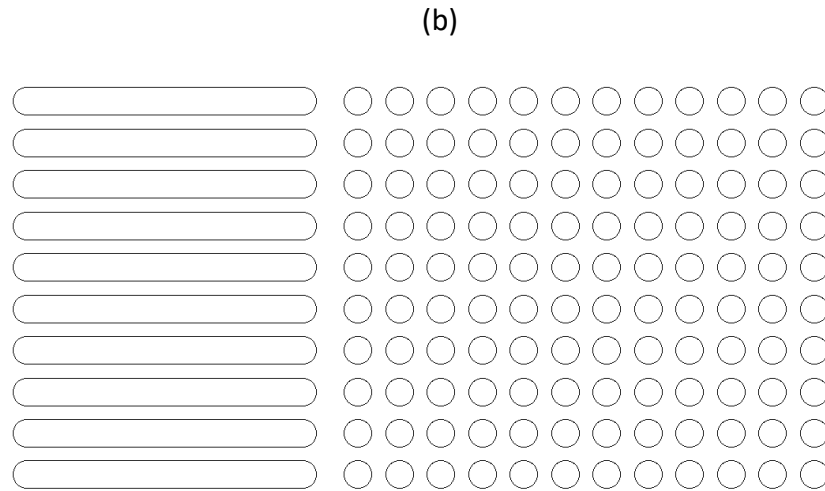


Figure 16: Top view of the geometry of the micro-sized device (a). Zoom-in picture of the inlet section where the fluid is guided by the short channels before entering in the pillars region (b)

-length: $L = 4000 \text{ } \mu\text{m} = 4 \text{ mm}$

-width: $w = 1950 \text{ } \mu\text{m} = 1.95 \text{ mm}$

-height: $h = 50 \text{ } \mu\text{m}$

In the channel there is a grid of many cylindrical and aligned pillars with a radius and height:

$$r_{\text{plr}} = 20 \text{ } \mu\text{m}$$

$$h_{\text{plr}} = 40 \text{ } \mu\text{m}$$

The device has just one inlet and one outlet. At the inlet and outlet section we have 34 short channels

for driving the fluid when it is injected by the syringe pump.

7.3 Computational domain

In order to reduce the computational domain, we consider a the 2D longitudinal section of the channel from the inlet to the outlet. Moreover, only a 3x3 squared grid of pillars is considered. The 3x3 grid is physically representative of the entire device and it is assumed to be large enough to simulate the patterns of the particles in the whole channel.

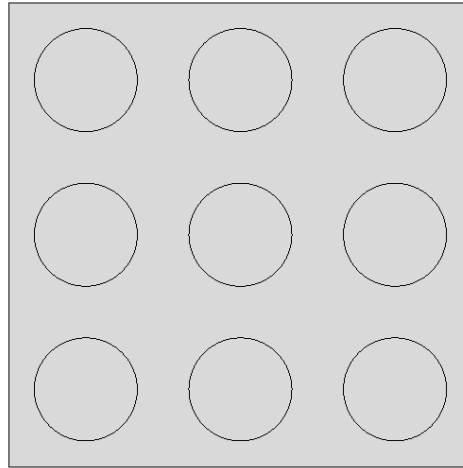


Figure 17: Computational domain

Since one of the main objectives of this work is studying the acoustofluidic phenomena varying the distance between the pillars d , the length and the width of the section are set as:

-length section $L_{\text{section}} = 6r_{\text{plr}} + 3d$

-width section $w_{\text{section}} = 6r_{\text{plr}} + 3d$

Being r_{plr} constant, the control volume enclosing the computational domain change its size according to the value of d .

7.4 Numerical modelling

The simulation is based on the thermoviscous theory of acoustofluidic developed by H. Bruus and J.T. Karlsen [6]. The governing equations of the thermoviscous theory are the continuity, the viscous and compressible Navier-Stokes and the heat transfer equations and the thermodynamic equation of state. The fluid's response to the ultrasound actuation is assumed to be de-coupled in a time-harmonic component (acoustic response) and a steady remainder (acoustic streaming). Thus, the governing equations are solved using the Nyborg's perturbation theory. The thermoacoustic equations are solved to the first-order in the frequency domain of the acoustic actuations. Then, the products of the resulting first-order field are used as source terms in the time-averaged second order equations to estimate the effect of the acoustic streaming. Finally, the first and second-order fields are used to obtain the acoustic radiation force and the drag force in order to simulate the particles patterns.

The governing equations are:

$$\partial_t \rho = -\nabla \cdot (\rho \mathbf{v}) \quad (7.1)$$

$$\rho \partial_t \mathbf{v} = -\nabla p - \rho \mathbf{v}(\nabla \cdot \mathbf{v}) + \mu_f \nabla^2 \mathbf{v} + \beta \mu_f \nabla(\nabla \cdot \mathbf{v}) \quad (7.2)$$

$$\partial_t T + (\nabla \cdot \mathbf{v})T = D_{th-f} \nabla^2 T + \frac{\mu_f \nabla^2}{2\rho c_{p-f}} (\nabla \cdot \mathbf{v} + (\nabla \cdot \mathbf{v})^T)^2 \quad (7.3)$$

$$p = p(\rho) \quad (7.4)$$

Before the actuation of any acoustic field, we consider a quiescent fluid at a constant temperature T_0 , density ρ_0 and pressure p_0 . Applying the perturbation theory:

$$p = p_0 + p_1 + p_2 \quad (7.5)$$

$$T = T_0 + T_1 + T_2 \quad (7.6)$$

$$\mathbf{v} = \mathbf{v}_1 + \mathbf{v}_2 \quad (7.7)$$

where:

$p_1 = \varepsilon \tilde{p}_1$, $T_1 = \varepsilon \tilde{T}_1$, $\mathbf{v}_1 = \varepsilon \tilde{\mathbf{v}}_1$ and $p_2 = \varepsilon^2 \tilde{p}_2$, $T_2 = \varepsilon^2 \tilde{T}_2$, $\mathbf{v}_2 = \varepsilon^2 \tilde{\mathbf{v}}_2$. The symbol \sim on the p, T and \mathbf{v} refers to the first and second-order perturbed variables. In acoustofluidic problems the perturbation parameter is calculated as $\varepsilon = U_0/\omega a$ where U_0 is the small velocity amplitude of the vibrating walls, ω the angular frequency and a a length scale. Usually, for high frequency oscillations, we can consider the velocity U_0 as the product of the frequency and the amplitude of the oscillation l [28]. Thus, $\varepsilon = \omega l/\omega a = l/a$. In the special case of cylindrical bodies, the length scale a is assumed to be the diameter d_{plr} . Therefore, in our problem we can write ε as:

$$\varepsilon = \frac{l}{d_{\text{plr}}} \quad (7.8)$$

where d_{plr} is the diameter of the pillars. The perturbation parameter must be $\varepsilon \ll 1$, meaning that the amplitude of the oscillation must be small respect the size of the pillar. Since the fluid is supposed at rest before the actuation, $\mathbf{v}_0 = 0$.

The governing equations for the first-order fields are:

$$\partial_t p_1 = \frac{1}{\gamma_f} [\alpha_f \partial_t T_1 - \nabla \cdot \mathbf{v}_1] \quad (7.9)$$

$$\partial_t T_1 = D_{\text{th}_f} \nabla^2 \mathbf{v}_1 T_1 + \frac{\alpha_f T_0}{\rho_0 c_{p_f}} \partial_t p_1 \quad (7.10)$$

$$\rho_0 \partial_t \mathbf{v}_1 = -\nabla p_1 + \mu_f \nabla^2 \mathbf{v}_1 + \beta \mu_f \nabla (\nabla \cdot \mathbf{v}_1) \quad (7.11)$$

Assuming that all the first order fields have an harmonic time dependence through the term $e^{-i\omega t}$:

$$p_1 = p_1(x, y)e^{-i\omega t} \quad T_1 = T_1(x, y)e^{-i\omega t} \quad \mathbf{v}_1 = \mathbf{v}_1(x, y)e^{-i\omega t} \quad (7.12)$$

and using the thermodynamic identity $\frac{T_0 \alpha_f^2}{\rho_0 c_{p_f} K_f} = \gamma_f - 1$, the governing equations are simplified to:

$$i\omega \mathbf{v}_1 + \nu_f \nabla^2 \mathbf{v}_1 + \nu_f \left[\beta + i \frac{1}{\gamma_f \rho_0 K_f \nu_f \omega} \right] \nabla (\nabla \cdot \mathbf{v}_1) = \frac{\alpha_f}{\gamma_f \rho_0 K_f} \nabla T_1 \quad (7.13)$$

$$i\omega T_1 + D_{th_f} \nabla^2 T_1 = \frac{\gamma_f - 1}{\alpha_f} \nabla \cdot \mathbf{v}_1 \quad (7.14)$$

From equations [7.13-7.14] the thermal and the viscous penetration depth δ_{th} and δ_s can be derived:

$$\delta_{th} = \sqrt{\frac{2D_{th_f}}{\omega}} \quad \delta_s = \sqrt{\frac{2\nu_f}{\omega}} \quad (7.15)$$

The equations of the first-order field are solved in COMSOL using the Thermoacoustics, Frequency Domain Interface. This interface is used to compute the acoustic variation of pressure, velocity and temperature in geometry of small dimensions. It computes the important viscous and thermal losses near rigid the walls, where the boundary layers arise. The Frequency Domain interface solves the thermoacoustics equations in the frequency domain, assuming all fields and sources to be harmonic in time according to the expressions (7.12).

The second-order continuity and Navier-Stokes equations are:

$$\partial_t \rho_2 = -\rho_0 \nabla \cdot \mathbf{v}_2 - \nabla \cdot (\rho_1 \mathbf{v}_1) \quad (7.16)$$

$$\rho_0 \partial_t \mathbf{v}_2 = -\nabla p_2 + \mu_f \nabla^2 \mathbf{v}_2 + \beta \mu_f \nabla (\nabla \cdot \mathbf{v}_2) - \rho_1 \partial_t \mathbf{v}_1 - \rho_0 (\mathbf{v}_1 \cdot \nabla) \quad (7.17)$$

The coupling in the second-order equations between the temperature field T_2 and the mechanical variables p_2 and \mathbf{v}_2 are neglected because for water the thermal effects in the first-order equations are minute, being small the pre-factor $\gamma_f - 1 \approx 10^{-2}$ and $\delta_{th}/\delta_s \approx 0.3$. Thus, the thermal effects are

computed only for the acoustic response. Considering the time-averaged equations and not the microsecond length scale of the ultrasound oscillation:

$$\rho_0 \nabla \cdot \langle \mathbf{v}_2 \rangle = -\nabla \cdot \langle \rho_1 \mathbf{v}_1 \rangle \quad (7.18)$$

$$\mu_f \nabla^2 \langle \mathbf{v}_2 \rangle + \beta \mu_f \nabla (\nabla \cdot \langle \mathbf{v}_2 \rangle) - \nabla \langle p_2 \rangle = \langle \rho_1 \partial_t \mathbf{v}_1 \rangle + \rho_0 \langle (\mathbf{v}_1 \cdot \nabla) \mathbf{v}_1 \rangle \quad (7.19)$$

The product of first-order fields act as source terms for the second-order problem. The equations of the second-order fields are solved in COMSOL using the Laminar Flow Interface. This interface computes the velocity and pressure fields for the flow of a single-phase fluid in laminar regime. Microfluidics deals with low Reynolds numbers and in the present application a single phase fluid is considered.

The equations solved by the Laminar Flow Interface are the continuity and the viscous-compressible Navier-Stokes equations. The term $-\nabla \cdot \langle \rho_1 \mathbf{v}_1 \rangle$ in eq. is introduced in eq.(7.19) as a Mass Source term by adding the following Weak Contribution in the continuity equation :

$$\text{Mass Source term} \rightarrow -\frac{1}{2} \iint [\partial_x \text{Re}(\rho_1 v_{1x}^*) + \partial_t \text{Re}(\rho_1 v_{1y}^*)] \tilde{p}_2 dV \quad (7.20)$$

where \tilde{p}_2 is the pressure test function.

The terms $\langle \rho_1 \partial_t \mathbf{v}_1 \rangle$ and $\rho_0 \langle (\mathbf{v}_1 \cdot \nabla) \mathbf{v}_1 \rangle$ are included in eq.(7.19) as Body Force term introducing the following Weak Contributions in the conservation of momentum:

$$\text{Body Force } x \rightarrow F_{1x} + F_{2x}$$

$$\text{Body Force } y \rightarrow F_{1y} + F_{2y}$$

where $F_{1x,y}$ and $F_{2x,y}$ are:

$$F_{1x,y} = \frac{1}{2} \text{Re}(\rho_1^* e^{-i\omega} v_{1x,y}) \quad (7.21)$$

$$F_{2x,y} = \frac{1}{2} \rho_0 (\text{Re}(v_{1x}^* \frac{dv_{1x,y}}{dx}) + \text{Re}(v_{1y}^* \frac{dv_{1x,y}}{dy})) \quad (7.22)$$

where x and y refers to the components of the velocity. In addition, the fourth-order non linear term $\rho_0(\langle \mathbf{v}_2 \rangle \cdot \nabla) \langle \mathbf{v}_2 \rangle$ is kept in the Laminar Flow Interface to enhance numerical stability. The Laminar Flow Interface is studied in a stationary time regime since the acoustic streaming is a steady-state phenomenon.

The motion of the particles is simulated computing the time-averaged acoustic radiation force and the Stokes drag force once the first and second order fields are obtained. The acoustic radiation force on a suspended small and spherical particle of radius a_p is given in equation (5.15):

$$\mathbf{F}^{\text{rad}} = -\frac{4\pi}{3} a_p^3 \left[\frac{1}{2} \kappa_f \text{Re}[f_1^* p_1^* \nabla p_1] - \frac{3}{4} \rho_0 \text{Re}[f_2^* \mathbf{v}_1^* \nabla \mathbf{v}_1] \right] \quad (7.23)$$

where κ_f is the compressibility of the fluid given by $\kappa_f = 1/(\rho_0 c_f^2)$. The monopole and dipole scattering coefficients f_1^* and f_2^* , according to equations (5.36-37) are:

$$f_1^* = \frac{1 - \tilde{\kappa} + 3(\gamma_f - 1) \left[\left(1 - \frac{\tilde{\alpha}}{\tilde{\rho}_0 \tilde{c}_p} \right) \left(1 - \frac{\chi_p \tilde{\alpha}}{\tilde{\rho}_0 \tilde{c}_p} \right) - \frac{4}{3} \frac{\chi_p \tilde{\alpha} \tilde{\kappa}}{\tilde{c}_p} \frac{c_{T,p}^2}{c_f^2} \left(1 - \frac{\tilde{\alpha}}{\tilde{\rho}_0 \tilde{c}_p \tilde{\kappa}} \right) \right] H(x_{\text{th}_f}, x_{\text{th}_p})}{1 + 4(\gamma_f - 1) \frac{\chi_p \tilde{\alpha}^2}{\tilde{\rho}_0 \tilde{c}_p^2} \frac{c_{T,p}^2}{c_f^2} H(x_{\text{th}_f}, x_{\text{th}_p})} \quad (7.24)$$

$$f_2^* = \frac{2(\tilde{\rho}_0 - 1)[1 - G(x_{s_f})]}{2\tilde{\rho}_0 + 1 - 3G(x_{s_f})} \quad (7.25)$$

where the expressions for $\tilde{\rho}_0, \tilde{c}_p, \tilde{\alpha}, \tilde{\kappa}, \chi_p, H(x_{th_f}, x_{th_p})$ and $G(x_s)$ are given in equations (7.29-35).

The time-averaged Stokes drag force on a spherical particle of radius a_p moving with a velocity \mathbf{u} near a solid wall in a fluid having a streaming velocity $\langle \mathbf{v}_2 \rangle$ has the following expression:

$$\mathbf{F}^{\text{drag}} = 6\pi\mu_f a_p (\langle \mathbf{v}_2 \rangle - \mathbf{u}) \quad (7.26)$$

valid for a particle sufficiently far from rigid walls. Nevertheless, in the present system the particles move very close to the pillars so the constraint is not respected. On the other hand, there are not theoretical expressions developed so far for the drag force acting on a particle moving close to cylindrical walls, so in the simulation eq.(7.26) is considered valid with some approximations.

The motion of the particles is simulated in COMSOL using the Particle Tracing for Fluid Flow Interface. This interface allows to trace the trajectories of particles in the presence of an external field. In the case of a fluid flow perturbed by an external acoustic field we add to the interface the predefined drag force available in the list of the applied fields and a force contribution, where the x and y components of the acoustic radiation force are given in input:

$$F_x^{\text{rad}} = -\frac{4\pi}{3} a_p^3 \left[\frac{1}{2} \kappa_f \text{Re} \left[f_1^* p_1^* \frac{\partial p_1}{\partial x} \right] - \frac{3}{4} \rho_0 \text{Re} \left[f_2^* (v_{1x}^* \frac{\partial v_{1x}}{\partial x} + v_{1y}^* \frac{\partial v_{1x}}{\partial y}) \right] \right] \quad (7.27)$$

$$F_y^{\text{rad}} = -\frac{4\pi}{3} a_p^3 \left[\frac{1}{2} \kappa_f \text{Re} \left[f_1^* p_1^* \frac{\partial p_1}{\partial y} \right] - \frac{3}{4} \rho_0 \text{Re} \left[f_2^* (v_{1x}^* \frac{\partial v_{1y}}{\partial x} + v_{1y}^* \frac{\partial v_{1y}}{\partial y}) \right] \right] \quad (7.28)$$

The particle tracing module provides a Lagrangian description of the motion of the particles. The particles are considered to be governed by Newton's law of motion, involving one ordinary differential equation (ODE) for each spatial direction. Thus, in total $2N$ ODEs are solved for studying the particle's behaviour. The particle masses m_j and all forces $F_i(r_j)$ acting on each particle at the position r_j are given in input. The ODE for the j th particle with a velocity $\mathbf{u}_j = d\mathbf{r}_j/dt$ is:

$$m_j \frac{du_j}{dt} = \sum_i \mathbf{F}_i(r_j) \quad (7.29)$$

where the forces $\mathbf{F}_i(r_j)$ acting on the particles are the acoustic radiation force and the Stokes drag force. The Particle Tracing for Fluid Flow Interface is studied with a time dependent solver in order to simulate the motion of the particles in the time domain.

7.5 Boundary conditions

Thermoacoustics Frequency Domain

Wall condition on the pillars boundaries :

This condition contains both a mechanical and a thermal selection. The mechanical condition we impose is the No Slip boundary condition which means that the velocity of the flow on the hard wall of the pillars is equal to zero:

$$\mathbf{v}_1 = 0 \rightarrow \text{No Slip boundary condition} \quad (7.30)$$

The thermal condition is the adiabatic boundary condition. This condition imposes no heat transfer between the wall and the medium.

$$-\mathbf{n} \cdot (k \nabla T) = 0 \rightarrow \text{Adiabatic boundary condition} \quad (7.31)$$

where \mathbf{n} is the outward pointing surface normal vector.

Velocity condition on the pillars walls:

The actuation of the external acoustic fields on the the pillars is modelled with a boundary condition on the first order velocity:

$$\mathbf{n} \cdot \mathbf{v}_{1y} = \omega l e^{-i\omega} \quad (7.32)$$

where l is the amplitude of the oscillation and ω the angular frequency. ωl is frequency-based velocity used to calculate the perturbation parameter. The incoming acoustic perturbation provided by the transducer is supposed to be a standing plane wave parallel to the x direction and travelling in the y direction; thus we consider the oscillation of the pillars only along the y axis. It is important to underline that this assumption can be adopted if the wavelength λ of the acoustic wave is larger than the channel transverse width [3]. Being $w = 1950 \mu\text{m} = 1.95 \text{ mm}$, it is imperative to use frequencies in the range of kHz which provide a wavelength of the order of cm. Nevertheless, streaming effects in acoustofluidic devices are more significant for frequencies in the MHz regime. For such high frequencies, λ becomes smaller than the transverse width of the channel and the assumption of the standing plane wave can no longer be used. The same assumption is adopted by Huang *et al.* in the analysis of streaming phenomena around oscillating sharp edges [4]. Boundary condition (7.32) is considered to mimic well the effect of the transducer. The first-order acoustic field is studied in the frequency domain, so the time dependency does not appear in the eq (7.32). The amplitude of the pillars oscillation l is given in input. Typical values of the displacement in a silicon structure have the order of 0.1 nm but with a more soft material like the PDMS amplitudes of the order of 0.1 μm can be adopted. This amplitude is acceptable from the point of view of the perturbation theory, since it is much lower than the pillars diameter and the condition $\varepsilon = l/d_{plr} \ll 1$ is respected. Combining the Wall and the Velocity conditions, the fluid's velocity is zero only in the x direction.

Periodic Conditions :

On the inlet and the outlet section of the domain we impose the Periodic Conditions on the first-order velocity, pressure and temperature. The continuity condition is imposed on the periodicity:

$$\mathbf{V}_{1,\text{in}} = \mathbf{V}_{1,\text{out}} \quad (7.33)$$

$$p_{1,\text{in}} = p_{1,\text{out}} \quad (7.34)$$

$$T_{1,\text{in}} = T_{1,\text{out}} \quad (7.35)$$

The periodic boundary condition is used because only a reduced portion of the device is simulated, which must be representative of the physical behaviour of the global system.

Laminar Single Phase Flow

Wall condition on the pillars boundaries:

The pillars are treated with the Wall condition where the No Slip velocity is imposed on the rigid boundaries:

$$\mathbf{v}_2 = 0 \rightarrow \text{No Slip boundary condition} \quad (7.36)$$

Inlet condition

At the inlet section is imposed a mass flow rate boundary condition in order to simulate the inflow of the water:

$$m_{\text{section}} = - \iint \rho(\mathbf{v}_2 \cdot \mathbf{n}) h \, dS \quad (7.37)$$

where h is the height of the device. The mass flow rate m we impose in the 3X3 grid is calculated as:

$$m_{\text{section}} = \frac{m_{\text{tot}}}{N_{\text{sections}}} \quad (7.38)$$

where m_{tot} is the total mass flow rate injected by the pump and controlled with the digital syringe pump and N_{sections} is the number of 3X3 grids along the vertical direction. Since the width of the channel is $w = 1950 \, \mu\text{m}$ and the width of the 3X3 grid is given by $6r_{\text{plr}} + 3d_{\text{plr}}$, the approximate value of N_{sections} is:

$$N_{\text{sections}} \approx \frac{w}{6r_{\text{plr}} + 3d} \quad (7.39)$$

According to the value of d_{plr} , different mass flow rates enter in the computational domain. The total mass flow rate is given in $\left[\frac{\text{kg}}{\text{s}}\right]$ and it is calculated from the flow rate in $\left[\frac{1}{\text{min}}\right]$ set in the digital syringe pump.

Periodic conditions

The Periodic Flow Condition is imposed on the inlet and the outlet section:

$$\mathbf{v}_{2,\text{in}} = \mathbf{v}_{2,\text{out}} \quad (7.40)$$

$$p_{2,\text{in}} = p_{2,\text{out}} \quad (7.41)$$

and the demanded pressure difference is calculated with the formula derived to estimate the Δp of a Poiseuille flow in a rectangular cross section of a flat channel:

$$\Delta p = \frac{12 Q_{\text{section}} L_{\text{section}} \mu_f}{w_{\text{section}} h^3 \left[1 - 0.630 \frac{h}{w}\right]} \quad (7.42)$$

where Q_{tot} is the flow rate in $\left[\frac{\text{m}^3}{\text{s}}\right]$, μ_f the dynamic viscosity of the water, $L_{\text{section}} = 6r_{\text{plr}} + 3d$, $w = 6r_{\text{plr}} + 3d$ and h are the length, the width and the height of the section of the 3X3 grid. The relationship (7.42) is valid for $h < w$.

Particle Tracing for Fluid Flow

Release from Grid :

The particles flowing in the channel are released from the inlet section at the time $t = 0$ s from spcified points given in input. At the inlet section we set the initial velocity of the particle equal to the velocity of the fluid flow computed by the Laminar Flow study:

$$\mathbf{u} = \mathbf{v}_2 \quad (7.43)$$

Drag Force and Acoustic Radiation Force

The particles are subjected to the acoustic radiation force and Stokes drag force introduced in the simulation as explained before.

The fluid and particles properties are summarized in the following table:

TABLE I: PARAMETERS OF THE FLUID AND THE PARTICLES

WATER			
Density	ρ_0	1000	kg m^{-3}
Compressibility	K_0	$4.45 \cdot 10^{-10}$	Pa^{-1}
Bulk viscosity	μ_b	$2.4 \cdot 10^{-3}$	Pa s
Dynamic viscosity	μ	$8.5 \cdot 10^{-4}$	Pa s
Speed of sound	c_0	1502	m s^{-1}
Specific heat capacity	C_p	4180	$\text{J kg}^{-1} \text{K}^{-1}$
Specific heat capacity ratio	γ	1.014	
Thermal conductivity	k_{th}	0.61	$\text{W m}^{-1} \text{K}^{-1}$
Thermal diffusivity	D_{th}	$1.43 \cdot 10^{-7}$	$\text{m}^2 \text{s}^{-1}$
Thermal expansion coefficient	α	$2.75 \cdot 10^{-4}$	K^{-1}

PARTICLES			
Density	ρ_0	1050	kg m^{-3}
Compressibility	K_0	$2.38 \cdot 10^{-10}$	Pa^{-1}
Speed of sound	c_0	1502	m s^{-1}
Specific heat capacity	C_p	1120	$\text{J kg}^{-1} \text{K}^{-1}$
Specific heat capacity ratio	γ	1.04	
Thermal conductivity	k_{th}	0.154	$\text{W m}^{-1} \text{K}^{-1}$
Thermal expansion coefficient	α	$2.1 \cdot 10^{-4}$	K^{-1}

7.6 Mesh Convergence

The simulation is performed with COMSOL Multiphysics, a finite elements solver. Two important steps in a finite elements analysis is the choice of the element type and the mesh convergence. In the simulation the selected element is Free Triangular. The common strategy used to choose the proper mesh size in finite elements simulations of acoustofluidic problems is to adopt a coarse mesh in the bulk of the fluid and refining near the walls. In this way, it is possible to provide a precise analysis of the boundary layers where the gradients of the physics variables are more significant. Moreover, the mesh convergence is studied varying the dimension of the mesh d_{mesh} as a linear function of the thickness of the viscous boundary layer δ_s , until a defined convergence parameter $C(g)$ becomes independent to any further decrease of the ratio δ_s/d_{mesh} . The relative convergence parameter for a solution g is:

$$C(g) = \sqrt{\frac{\int (g - g_{\text{ref}})^2 dy dx}{\int g_{\text{ref}}^2 dy dx}} \quad (7.44)$$

where g_{ref} is the solution for the most refined mesh. In this work it follows a different approach, for three main reasons:

- (i) Presence of pillars: the pillars are close to each other so it is important to refine the mesh in all the computational domain in order to study the significant gradients in the areas between the pillars.
- (ii) Circular walls: the solid walls are the circular boundaries of the pillars, so it is much more convenient to use the Boundary Layers around the pillars rather than performing a mesh refinement.
- (iii) Variation of the applied frequency: the aim of this work is to change the frequency until a minimum value allows particles trapping. Thus, it is not reasonable to select a mesh as a function of the frequency (the viscous boundary layer thickness is a function of the angular frequency ω).

The mesh convergence is divided in two steps: first an arbitrary mesh size is given in input (arbitrary mesh size \rightarrow an arbitrary number of nodes) and the number of the boundary layers is increased until the variables of interest start to converge. Then, the mesh size d_{mesh} is reduced to determine the minimum value at which the solutions do not change after further reductions. The supervised variables are the first-order pressure p_1 , temperature T_1 , velocity \mathbf{v}_1 and the second-order velocity \mathbf{v}_2 . For what concerns the first-order fields, only the real part is considered (the first-order solutions are plane waves propagating in space with the complex wave number). The surface average of the variables are exported from COMSOL. The mesh convergence analysis is performed adopting the input parameters used in the experiments:

- $f = 30 \text{ kHz}$
- $l = 0.5 \text{ }\mu\text{m}$
- $d = 20 \text{ }\mu\text{m}$
- $Q_{\text{tot}} = 0.5 \frac{\mu\text{l}}{\text{min}}$

The boundary layer dependence is performed with a mesh size:

$$d_{\text{mesh}} = 12.1 \text{ }\mu\text{m} \rightarrow \text{\#Nodes} = 60708$$

The thickness of the first boundary layer is $1/20$ of the element size and the imposed stretching factor is 1.2. It means that the thickness increases by 20% from one layer to the next.

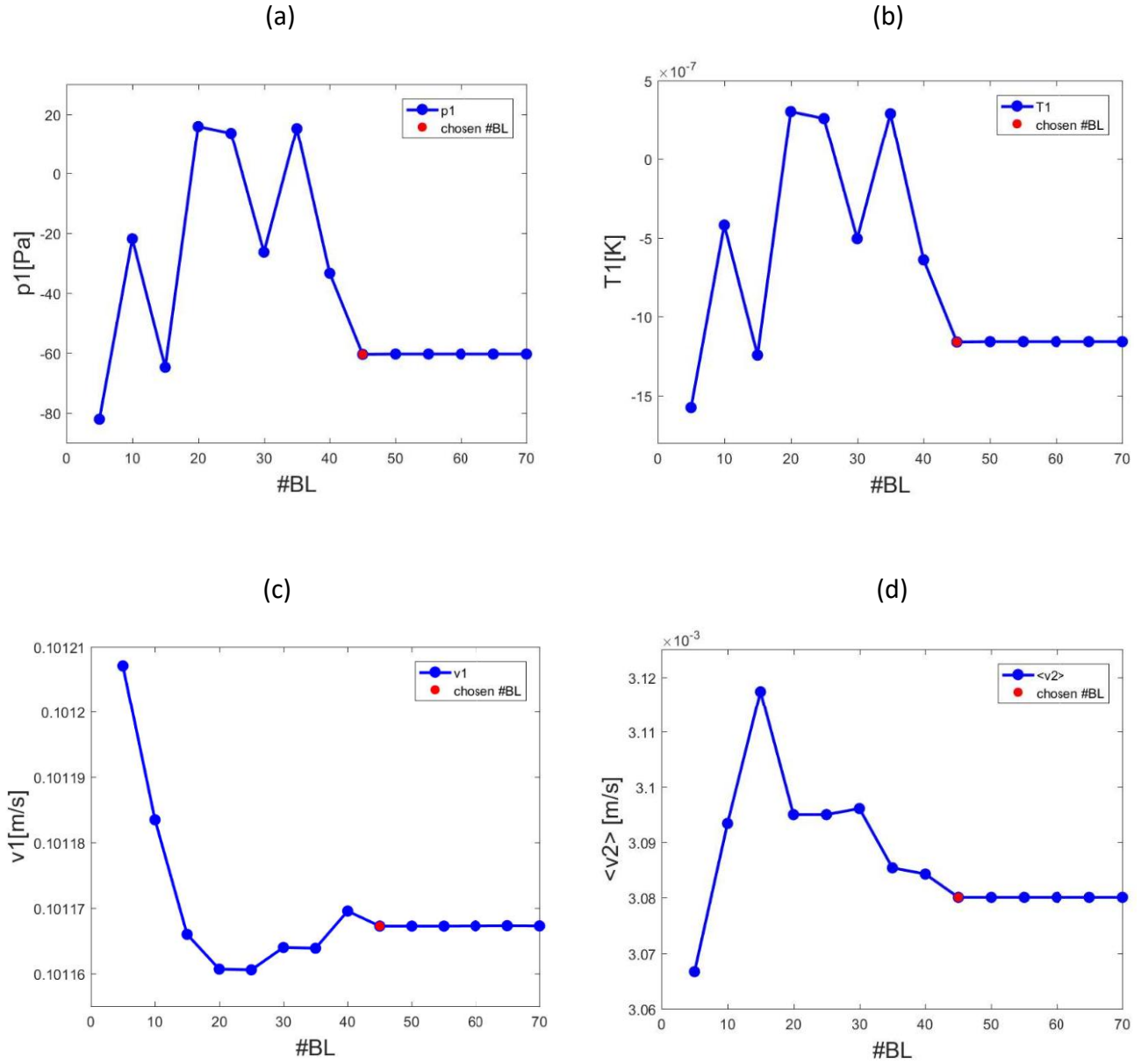


Figure 18: Mesh convergence analysis. Line plots of p_1 (a), T_1 (b), v_1 (c), v_2 (d) for an increasing number of boundary layers.

As the figures reveal, the convergence is achieved for all the variables adopting 45 boundary layers.

Now 45 boundary layers are kept constant, while the mesh size is reduced (the number of nodes is increased).

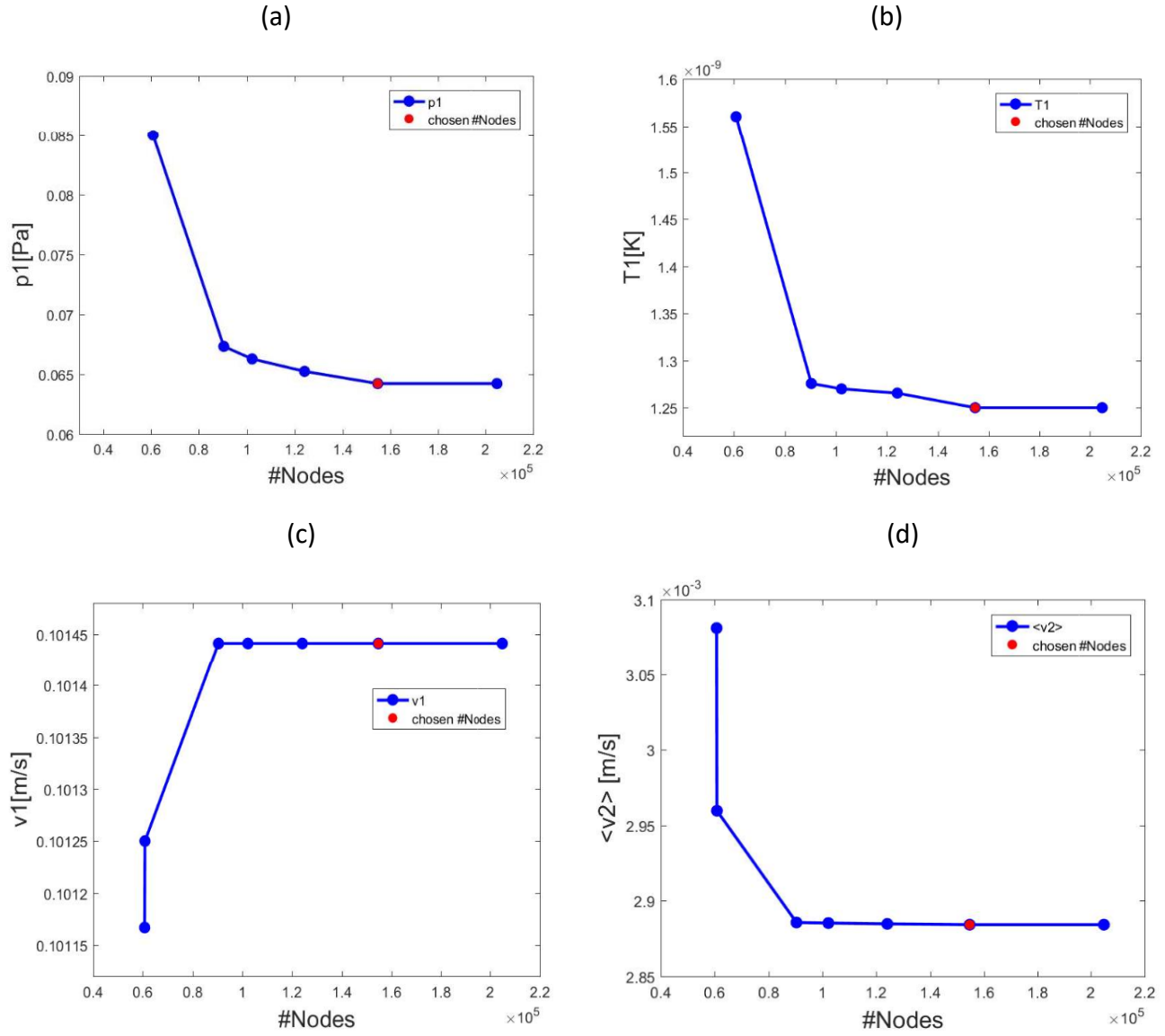


Figure 19: Mesh convergence analysis. Line plots of p_1 (a), T_1 (b), v_1 (c), v_2 (d), for an increasing number of nodes.

For the first and second order velocity 90374 nodes are sufficient ($d_{\text{mesh}} = 3.03 \mu\text{m}$) but for the first order pressure and first order temperature 154665 nodes ($d_{\text{mesh}} = 1.89 \mu\text{m}$) are required. As a result, 154665 nodes should be adopted.

Finally, the mesh convergence analysis has provided the following results:

#Boundary Layers= 45

154665 nodes $\rightarrow d_{\text{mesh}} = 1.89 \text{ } \mu\text{m}$

It is important to underline that 154665 nodes are valid for this particular geometry. Increasing the distance between the pillars, the section of 3x3 pillars becomes bigger and with a mesh size $d_{\text{mesh}} = 1.89 \text{ } \mu\text{m}$ the number of nodes increases. Nevertheless, we give in input the dimension of the the mesh and not the number of nodes, so the mesh convergence remains valid also for larger computational domains.

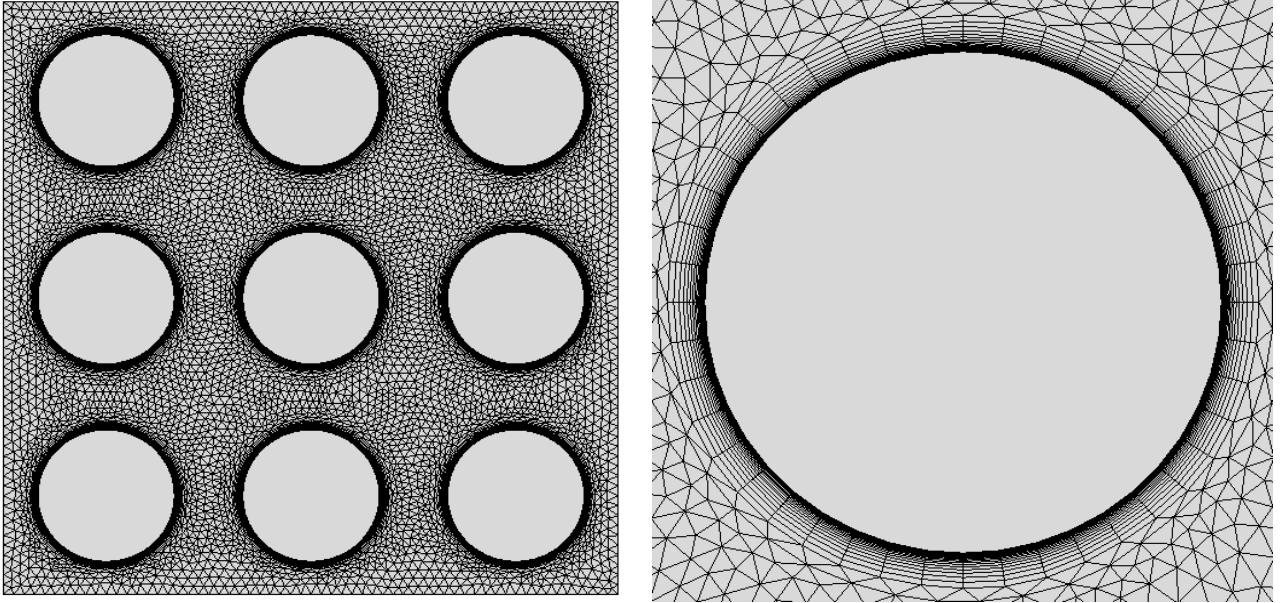


Figure 20: Mesh of the computational domain with $\#BL = 45$ and $d_{\text{mesh}} = 1.89 \text{ } \mu\text{m}$ (a). Zoom-in on a single pillar to highlight the 45 boundary layers.

7.7 Results and discussion

The simulation is performed with the input parameters adopted in the mesh convergence

- $f = 30 \text{ kHz}$
- $l = 0.5 \text{ }\mu\text{m}$
- $d_{\text{plr}} = 20 \text{ }\mu\text{m}$
- $Q_{\text{tot}} = 0.5 \frac{\mu\text{l}}{\text{min}}$

At this frequency, the depth of the thermal and viscous boundary layer and the wavelength are:

$$\delta_{\text{th}} = \sqrt{\frac{2D_{\text{th}}}{\omega}} = \sqrt{\frac{2 \cdot 1.43 \cdot 10^{-7}}{1.885 \cdot 10^5}} \approx 1.2 \text{ }\mu\text{m} \quad \delta_s = \sqrt{\frac{2\nu_f}{\omega}} = \sqrt{\frac{2 \cdot 8.5 \cdot 10^{-7}}{1.885 \cdot 10^5}} \approx 3.1 \text{ }\mu\text{m} \quad \lambda = \frac{c_f}{f} = \frac{1502}{30000} = 5 \text{ cm}$$

so the conditions for the validity of the thermoviscous model $\delta_s, \delta_{\text{th}} \ll \lambda$ are respected. Moreover, the models remains applicable for every frequency in the range of KHz and MHz. Since particles with a size $a_p \sim \delta_{\text{th}}, \delta_s$ are taken in consideration, the thermoviscous model is necessary to capture well the particles behaviour.

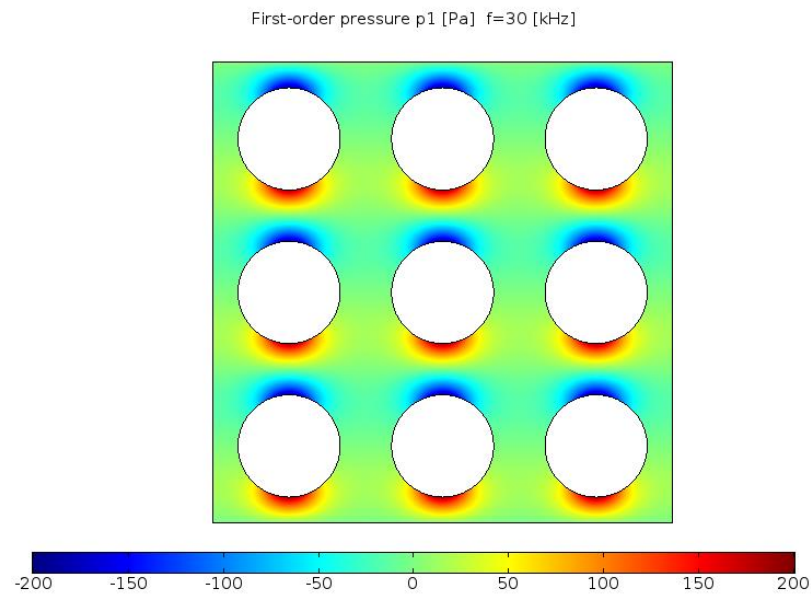
According to the analysis of Huang *et al* $l = 0.5 \text{ }\mu\text{m}$ is the amplitude corresponding to a voltage of 10 V_{PP} , which is the value used in the experiments.

For what concerns the acoustic temperature, we want to underline that COMSOL computes the small thermal variations to the initial temperature and not the absolute values. With this in mind, we refer to T_1 as the small changes to the thermal field after the actuation of the acoustic wave to the pillars.

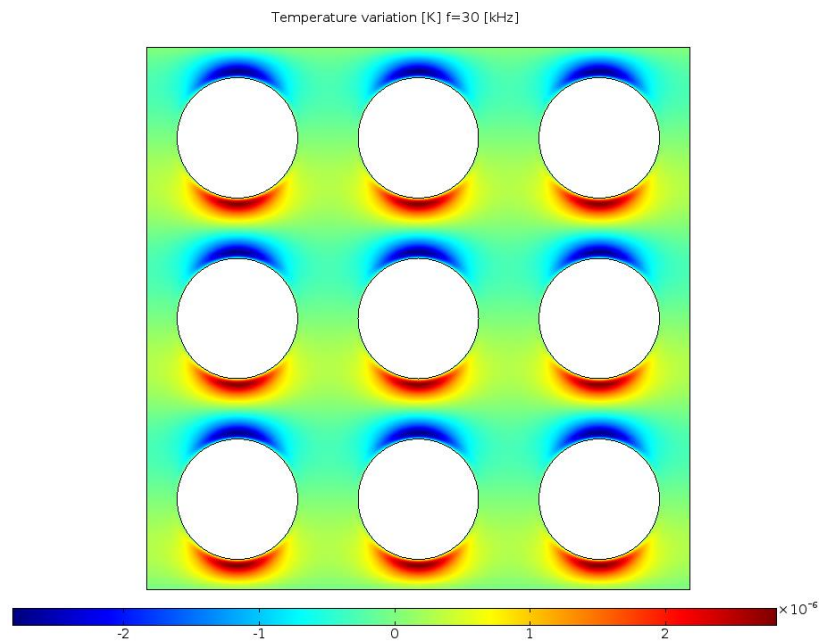
First-order fields

The following figures provide the magnitude of the acoustic first-order field after the actuation of the pillars:

(a)



(b)



(c)

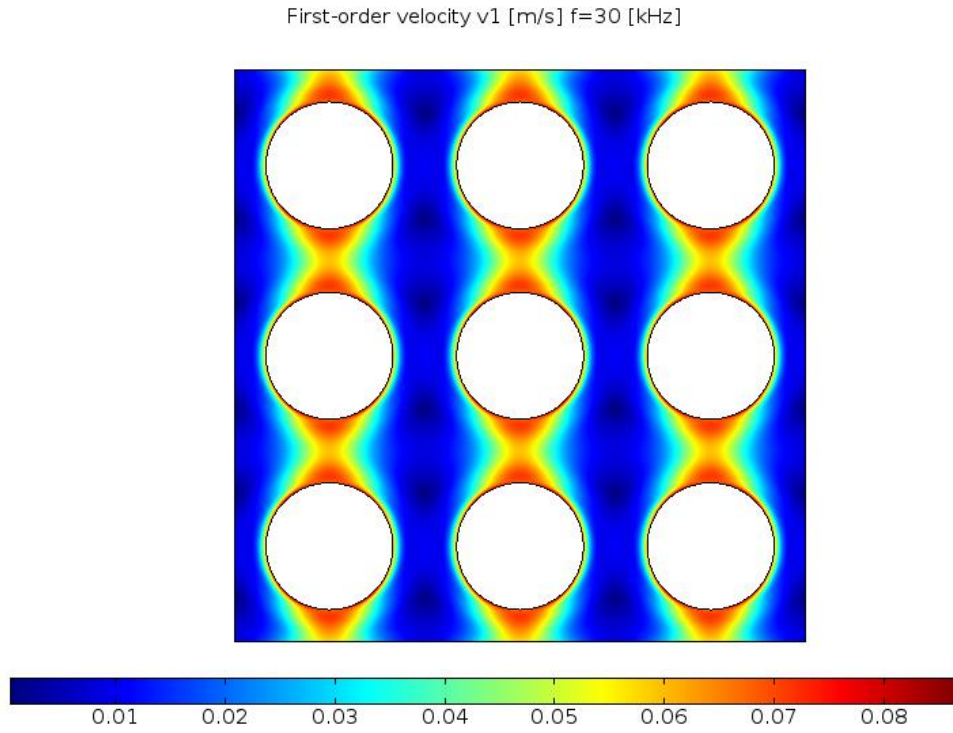
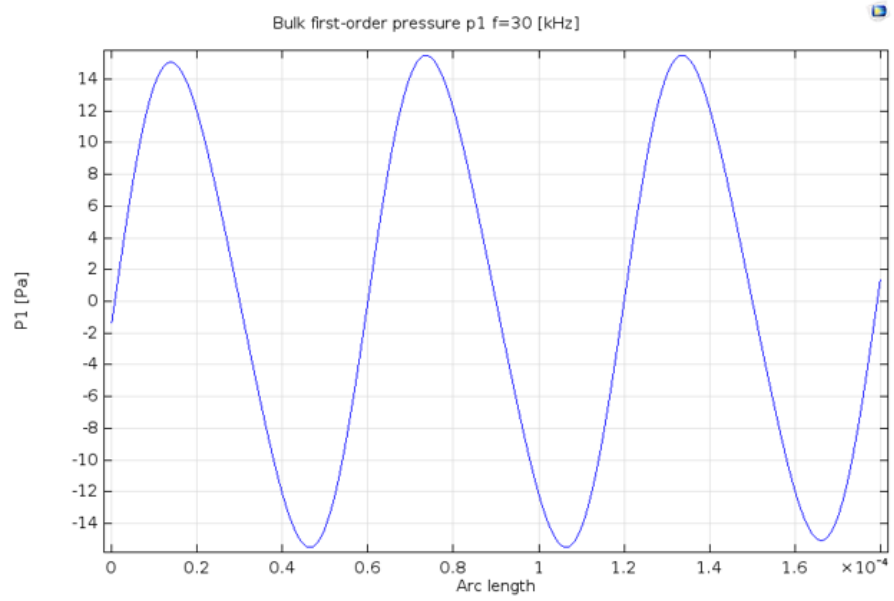


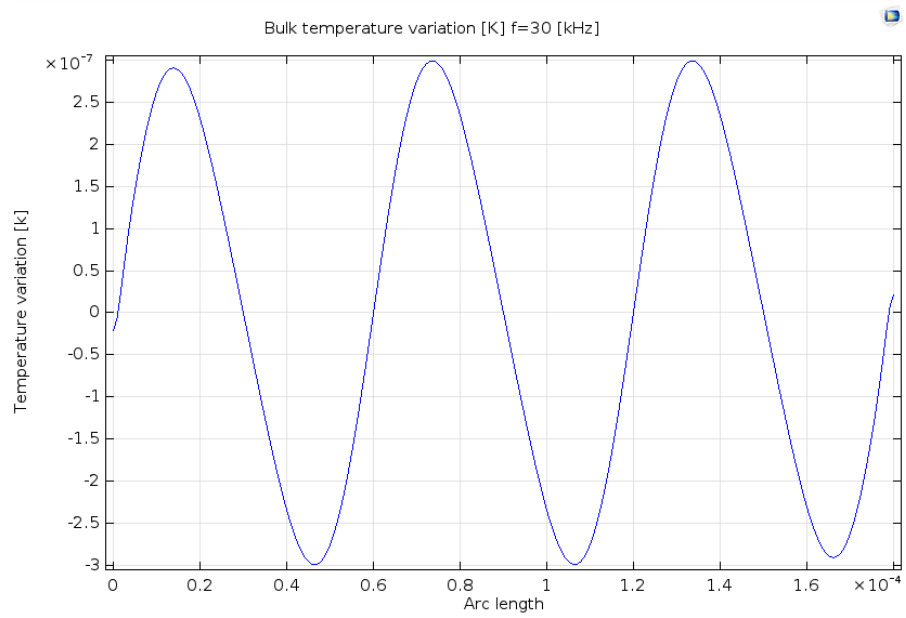
Figure 21: Color plots of the psicillating first-order fields of the fluid response to the acoustic actuation of PDMS pillars with a vertical standing wave at a frequency $f = 30$ kHz and amplitude $l = 0.5 \mu\text{m}$: (a) pressure, (b) temperature (c) velocity v_1

Then, the trends of p_1 , T_1 and v_1 along vertical lines in the two regions of interest, the bulk of the fluid and the critical area between two neighbouring pillars, are shown in the line-plots below:

(a)



(b)



(c)

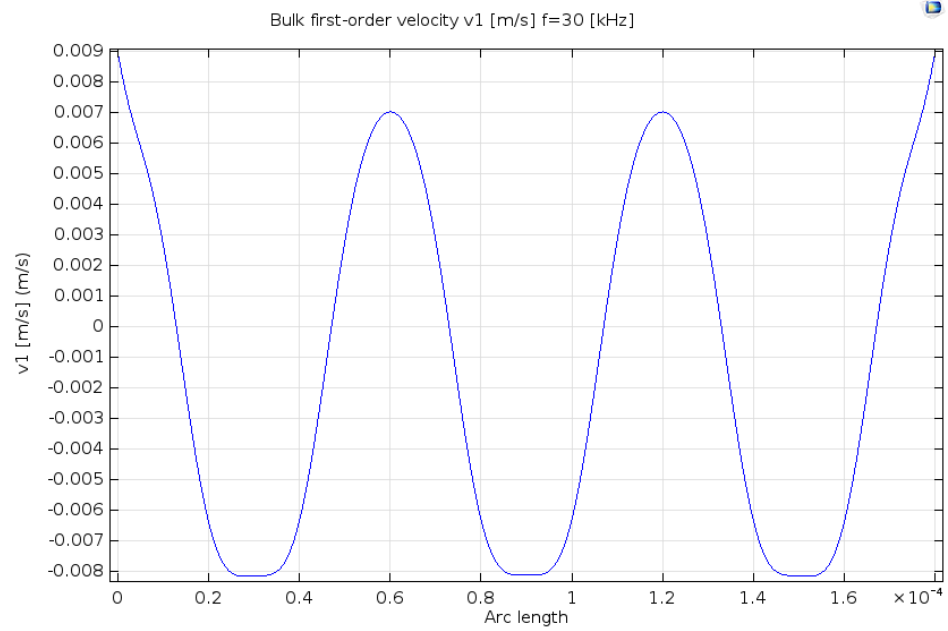
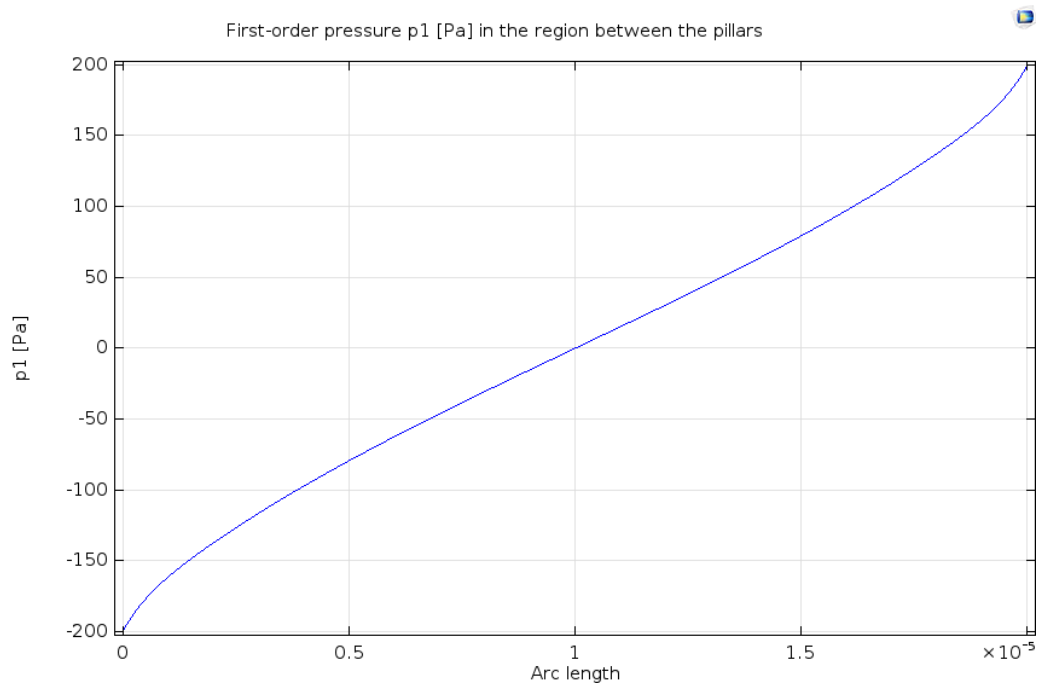
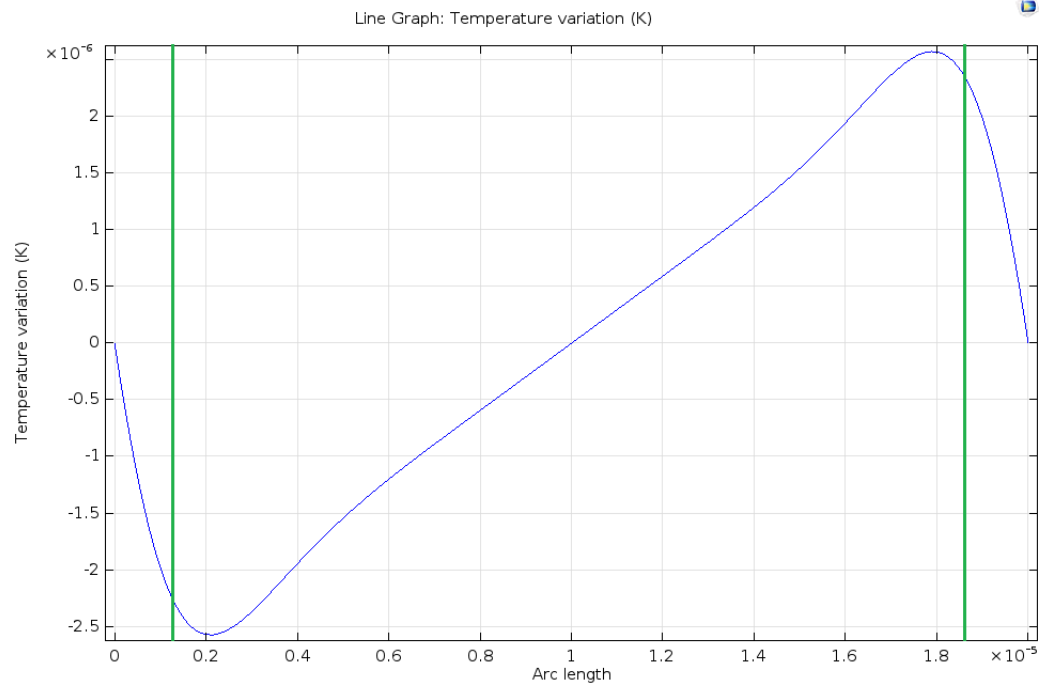


Figure 22: Line plots along a vertical line in the bulk of the fluid of the first-order: (a) pressure, (b) temperature, (c) velocity

(a)



(b)



(c)

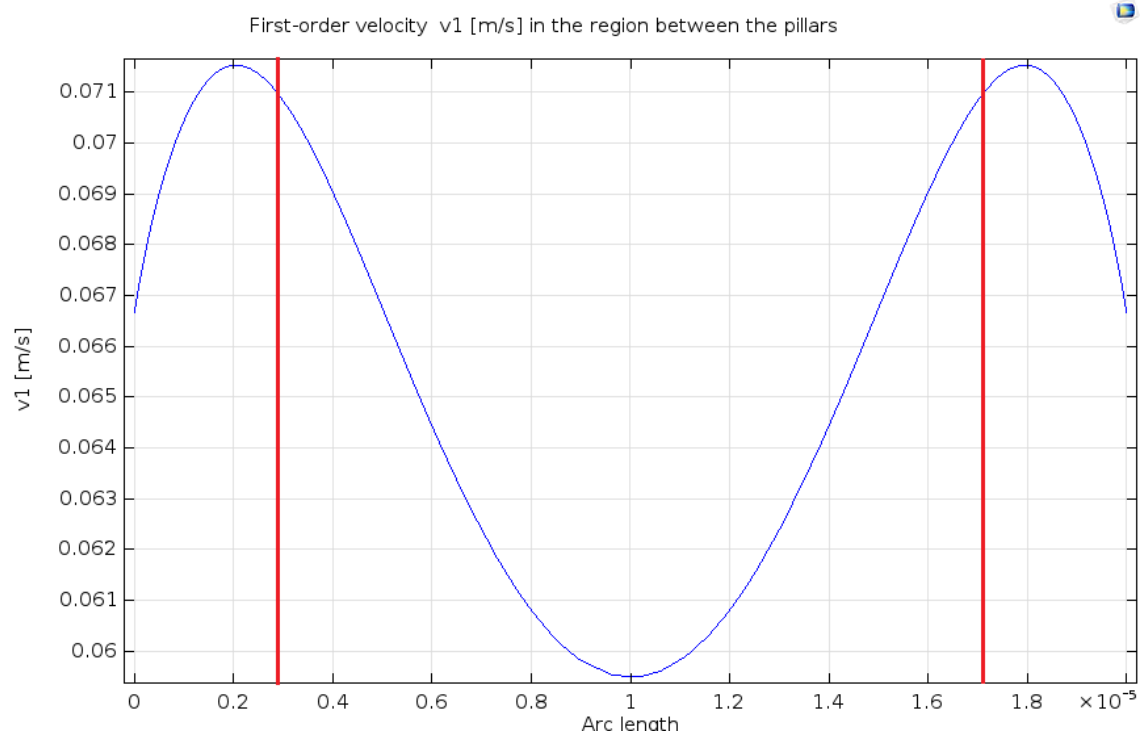


Figure 23: Line plots along a vertical line in the gap between the pillars of the first-order: (a) pressure, (b) temperature, (c) velocity.

Figures 21 (a-b) show that the magnitude of p_1 and T_1 has the same spatial structure, with a significant variation on the opposite sides of the pillars in the direction of the oscillation, while in the bulk the it is almost homogeneous. The acoustic wave is supposed to travel from the bottom to the top of the section, resulting in the positive and negative values respectively in the inferior and superior half boundaries of the pillars. On the contrary, figure 21 (c) shows how the first order velocity \mathbf{v}_1 remains positive both in the upper and lower parts of the pillars where it exhibits also its maximum values, as expected. Along the vertical gap between the pillars at $x = 0, d + 2r_{plr}, 2d + 4r_{plr}, 3d + 6r_{plr}$, we can observe the six nodes of the first order velocity, two for each pillar. Along the same gap, according to figure 22 (a-b), p_1 and T_1 oscillate with a sinusoidal behaviour while \mathbf{v}_1 has as pseudo-harmonic variation due to the presence of the nodes. The sinusoidal behaviour of the first-order field is expected: as it is shown in chapter [3], H.Bruus demonstrated that when two opposite vertical walls of a microfluidic chamber are forced to oscillate in anti-phase with a velocity $\mathbf{v}_{1x}(\pm L, t) = \pm \omega l e^{-i\omega t}$, where L is the distance between the walls, the solution of the first-order velocity is a superposition of a pair of counter-propagating plane waves with a complex wave number $k = k_0 (1 + i\gamma_f)$. The solution of the first-order velocity of the fluid \mathbf{v}_1 derived by H. Bruus, assumes expression (3.49):

$$\mathbf{v}_{1x}(x, t) \approx (-1)^n \omega l \left[-\frac{i}{n\pi\gamma} \sin\left(n\pi \frac{x}{L}\right) + \frac{x}{L} \cos\left(n\pi \frac{x}{L}\right) \right] e^{-i\omega t}$$

Our analysis is different because the actuated boundaries are the walls of the pillars and not the walls of the chamber. In order to verify the consistency of the numerical model, the profile of the first order velocity along a vertical line between two pillars (fig. 23(c)) is compared to the analytical solution derived by Bruus (eq. 3.49):

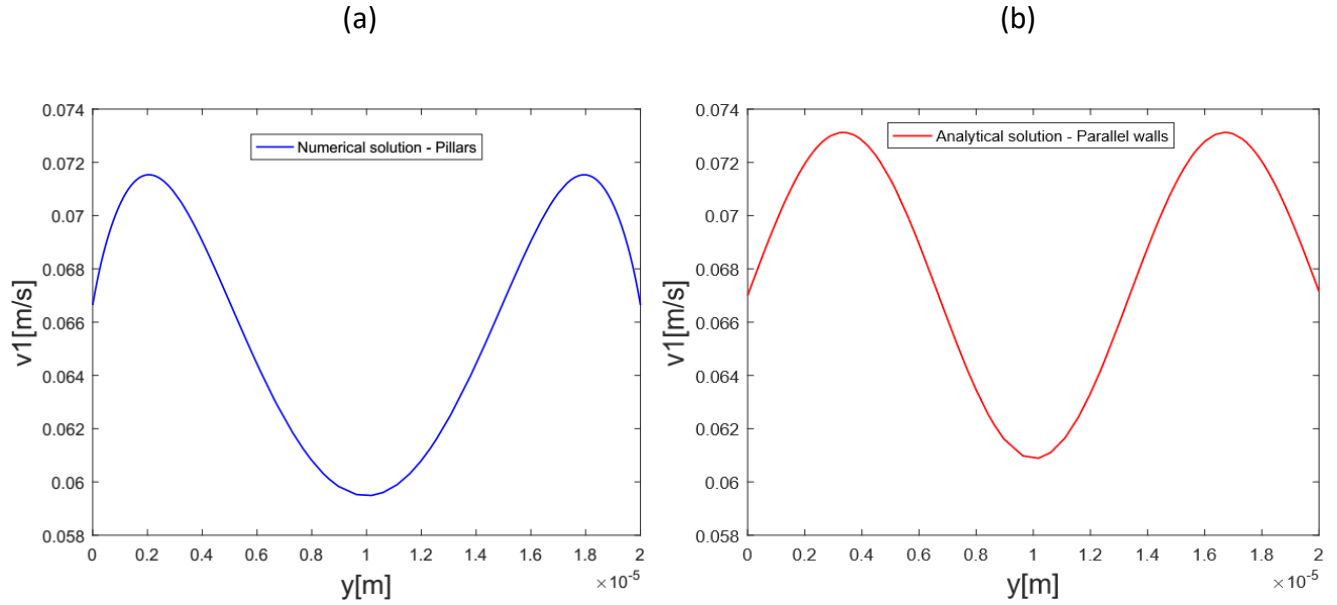


Figure 24: Comparison between the numerical (a) and analytical (b) solution of the first order velocity

The numerical solution is very close to the analytical prediction, but it displays lower values. The differences between the two profiles are related to the different geometries taken into account. For what concerns the analytical solution, two parallel and vertical walls of infinite length are considered. On the other hand, the computational results are derived studying the oscillation of two circular walls with a finite length. With this in mind, and considering the similar shape of the two curves, the numerical model is verified and it can be considered consistent with the theoretical behavior. In order to perform the verification using the same setup for the numerical and the analytical solution, the model is implemented in a configuration where the parallel and infinite walls are simulated by two parallel walls very long compared to the distance ($L = 2000 \text{ } \mu\text{m} \gg d = 20 \text{ } \mu\text{m}$). In this case, it is expected to obtain a behavior of the fluid which is very close to the theoretical domain used to derive the analytical solution. The distance between the walls is equal to the distance between the pillars $d = 20 \text{ } \mu\text{m}$.

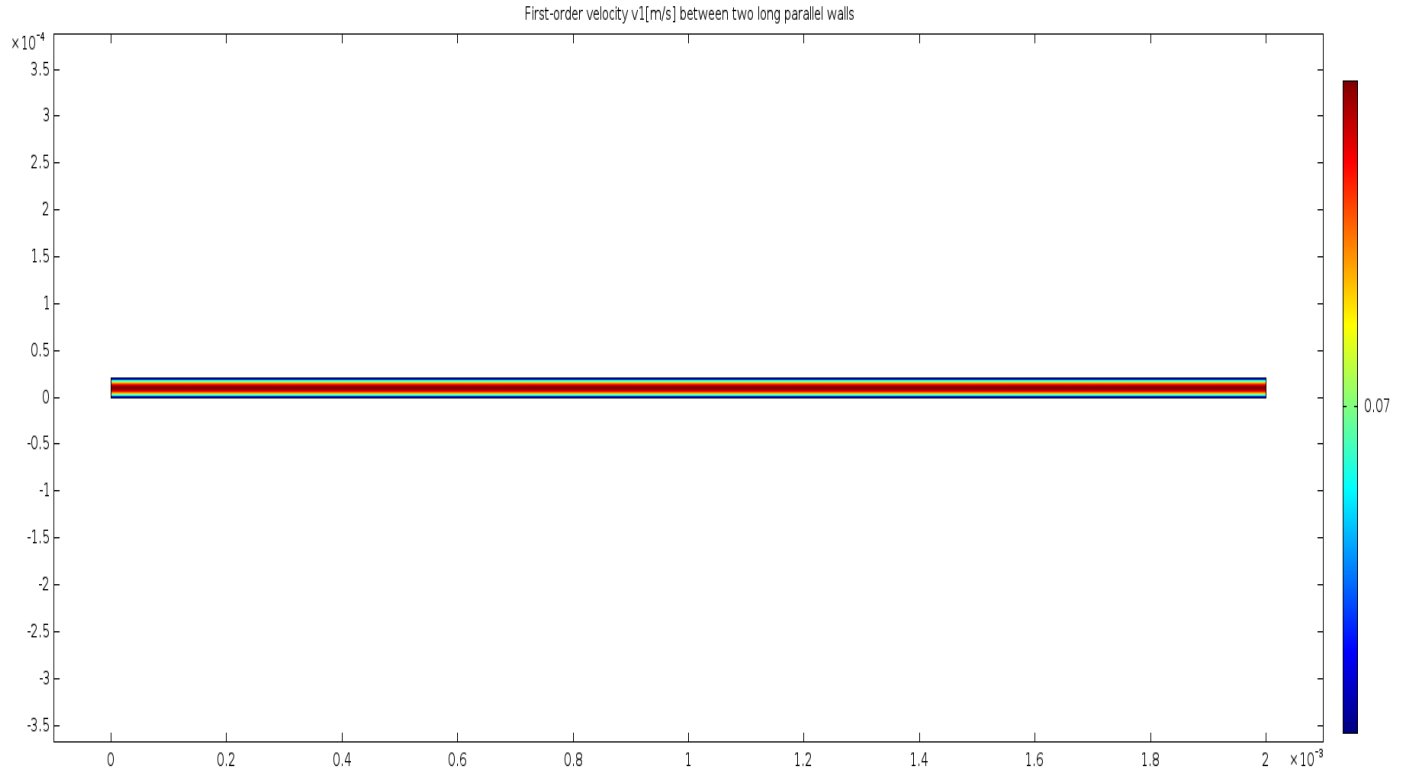


Figure 25: Color plot of the first order velocity between two long and parallel walls

The comparison between the numerical and the analytical solution is considered along a vertical line at $x = L/2$, at the middle of the length of the plates.

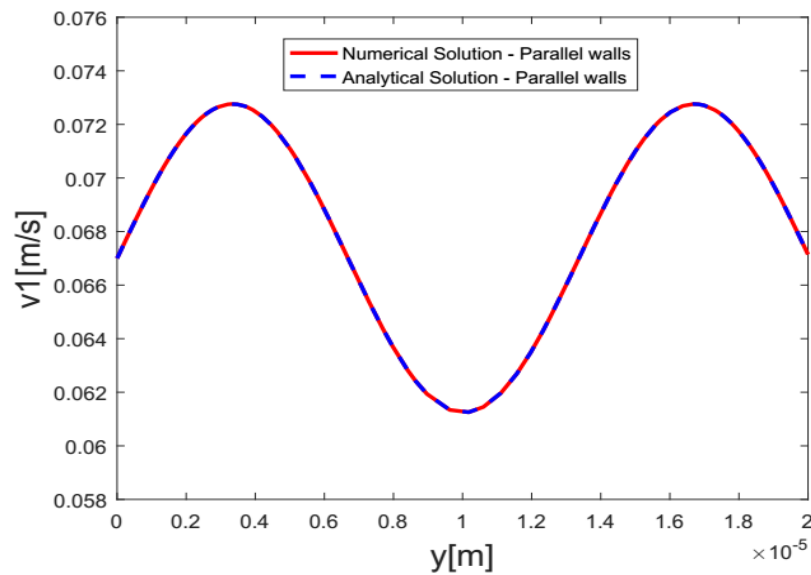


Figure 26: Numerical and analytical solutions compared in the parallel walls configuration

In this configuration, it is obtained a good superposition between the numerical and the analytical solution, meaning that the model is accurate and self-consistent.

Figures 23 (a-b-c) provide the trend of the first-order fields along a vertical line connecting two consecutive pillars. As mentioned before, p_1 and T_1 change in sign between the upper and lower boundary of a pillar and this variation is linear both for p_1 and T_1 . The temperature variation on the pillars walls is zero since we applied the adiabatic condition. The thickness of the thermal boundary layers δ_{th} is indicated with the vertical green line. The rate of change of T_1 inside the thermal boundary layer is approximately 2.5 %. On the other hand, figure 23 (c) reveals that \mathbf{v}_1 has a parabolic profile along the vertical distance between two pillars, with the minimum value in the center. The amplitude δ_s of the viscous boundary layers is marked with the red line; inside the boundary layers, \mathbf{v}_1 increases locally with a rate of 6 %.

Second-order field

In this section the color and vector plot of the streaming velocity are provided. The first emphasizes the magnitude of $\langle \mathbf{v}_2 \rangle$, while the second shows the streaming trajectories followed by the particles dominated by the acoustic streaming. The vector plots are computed in COMSOL giving in input the x and y components of the variable of interest. For what concerns the acoustic streaming, we give in input v_{2x} and v_{2y} . Meanwhile, the color plot of the magnitude of the second-order velocity plotted is

given by $|\mathbf{v}_2| = \sqrt{v_{2x}^2 + v_{2y}^2}$.

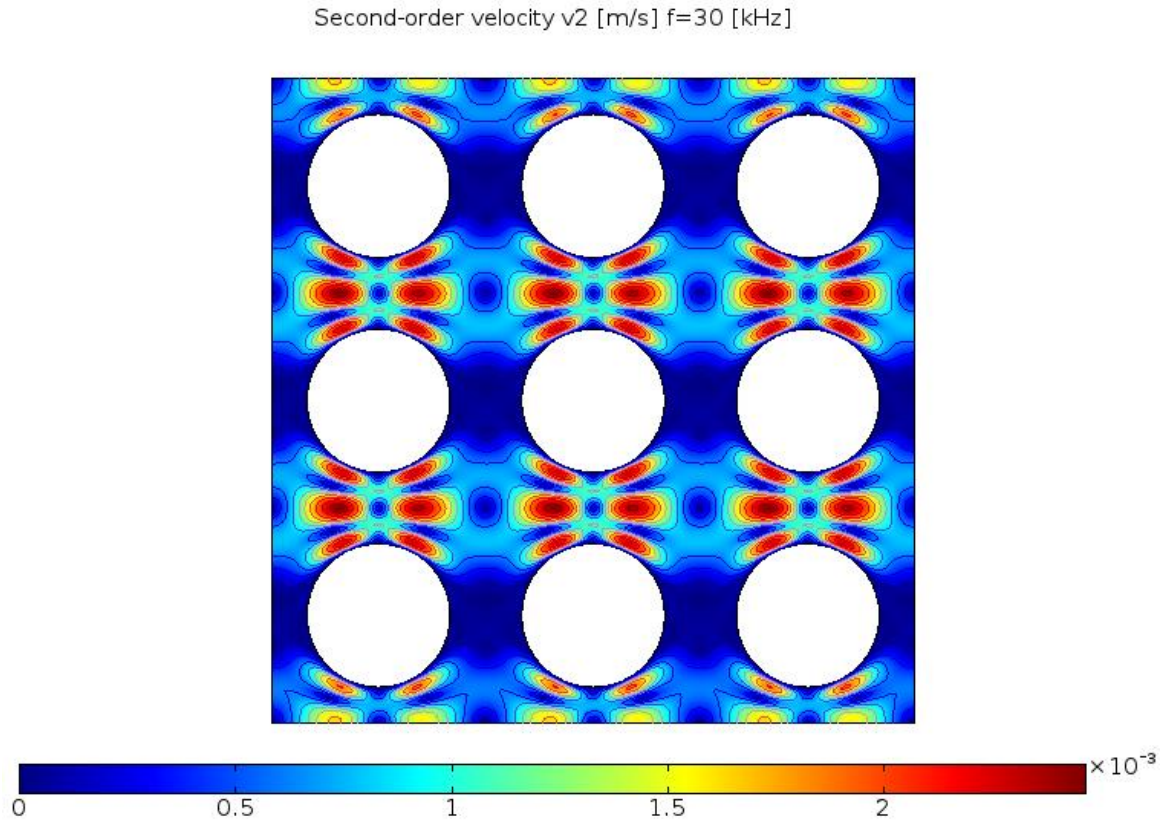


Figure 27: Color plot of the magnitude of the second-order velocity

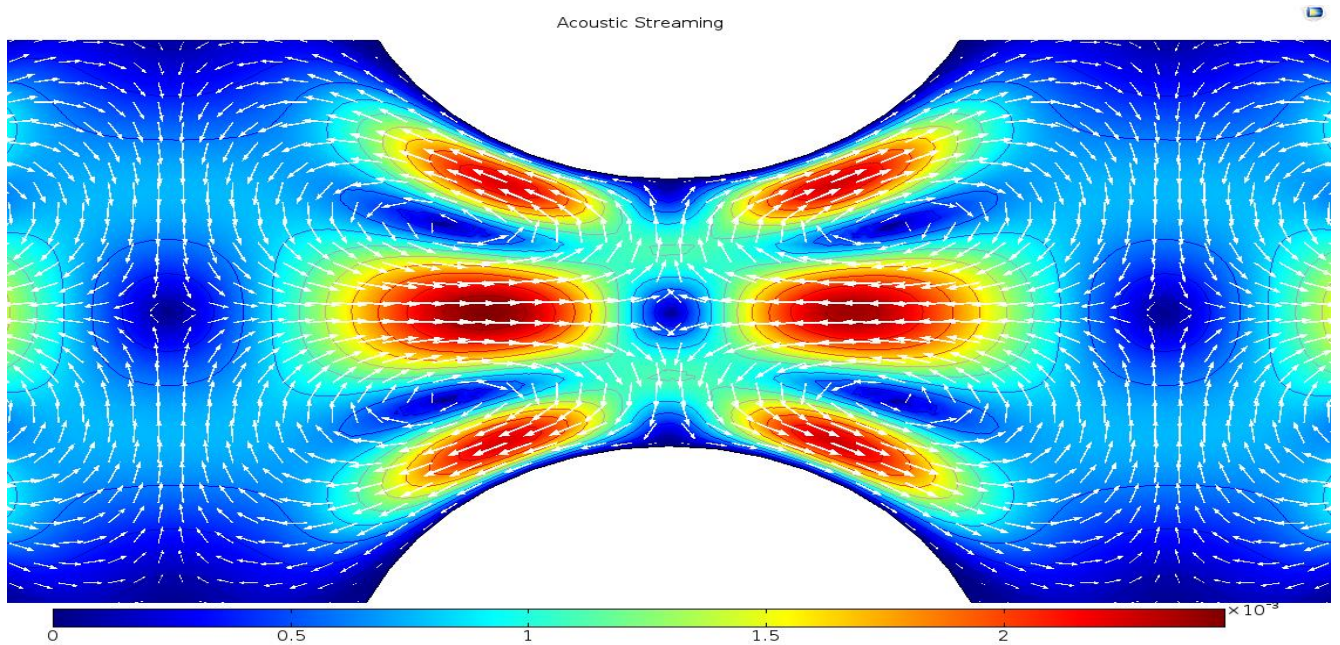


Figure 28: Color and vector plot (white arrows) of the second-order velocity between two pillars

Figure 28 exhibits the four Rayleigh streaming rolls in the bulk of the fluid (white arrows). The magnitude of the streaming velocity is maximum close to solid walls and it has two local maxima on the horizontal center axis between two pillars, where the opposite pairs of bulk rolls meet. A similar solution is obtained by Bruus *et al* in the numerical study of the frontal surface of a liquid-filled micro-chamber [7]. The configuration of the the acoustic streaming is close to Rayleigh's analytical solution in figure 8, but it deviates on the following points: (i) The oscillating boides are cylinders and not parallel plates, meaning that the Schlichting boundary vortices are not parallel to to the Rayleigh bulk vortices but they follow the shape of the cylinder. The effects are on the lower strength in driving the acoustic streaming from the Stokes layer to the bulk.

(ii) The analysed section is not the frontal area of liquid-filled gap but the longitudinal surface of the channel where the flow rate is injected and a pressure difference exists between the inlet and the outlet.

(iii) The length of the oscillating boundaries of the pillars is the semi-perimeter πr_{plr} , which is shorter than $\lambda/2$, the length scale usually adopted for the chambers where the Rayleigh streaming is more pronounced. As a result, the magnitude of the bulk streaming is lower respect to the Rayleigh predictions. On the other hand, the maximum gap between the vibrating walls is $2r_{plr} + d \ll \lambda$ so the limit of the Schlichting-Rayleigh streaming theory is respected.

According to the Schlichting's solution, the slip velocity in the bulk has a sinusoidal behaviour $\mathbf{v}^{slip} = -\frac{3}{4\omega} r_{plr} k \sin(4r_{plr} kx)$.

A similar trend can be seen in the line plot shown in figure 29. The slip velocity has been computed on a horizontal center line between two pillars from the inlet to the outlet of the domain.

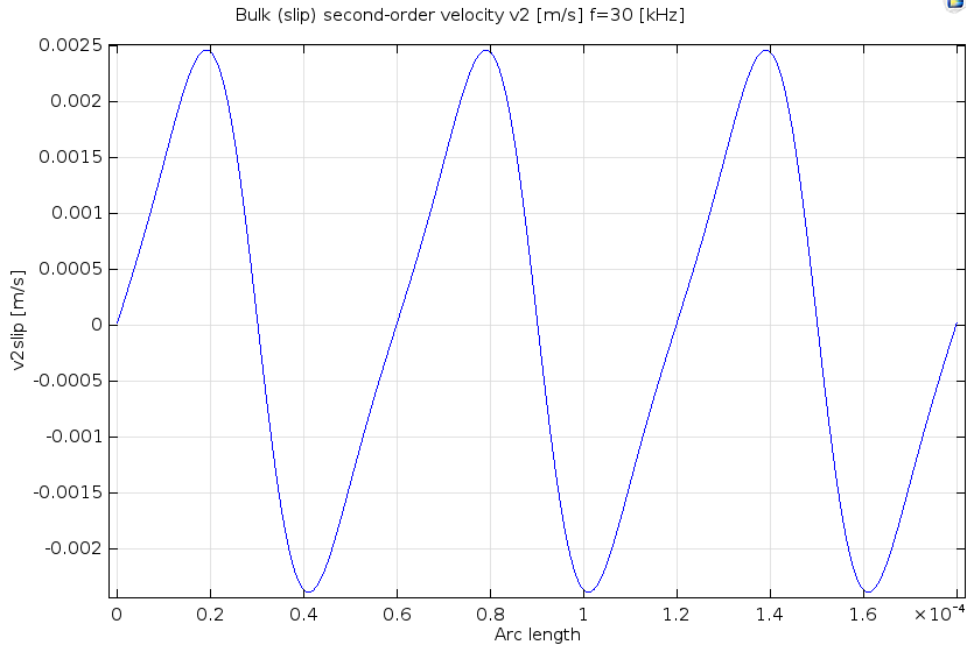


Figure 29: Line plot of the slip streaming velocity outside the Stokes layer

Acoustic radiation force

In this paragraph we focus on the analysis of the acoustic radiation force, the other important physical phenomena involved in acoustofluidic which allow the manipulation of the microparticles. The color plot of the magnitude of F^{rad} is provided, in order to show where the acoustic radiation force is more

significant. The magnitude of the force is computed as $F^{\text{rad}} = \sqrt{F_x^{\text{rad}2} + F_y^{\text{rad}2}}$. Then, F_x^{rad} and F_y^{rad} are given in input to obtain the vector plot of F^{rad} , is given in a logarithmic scale.

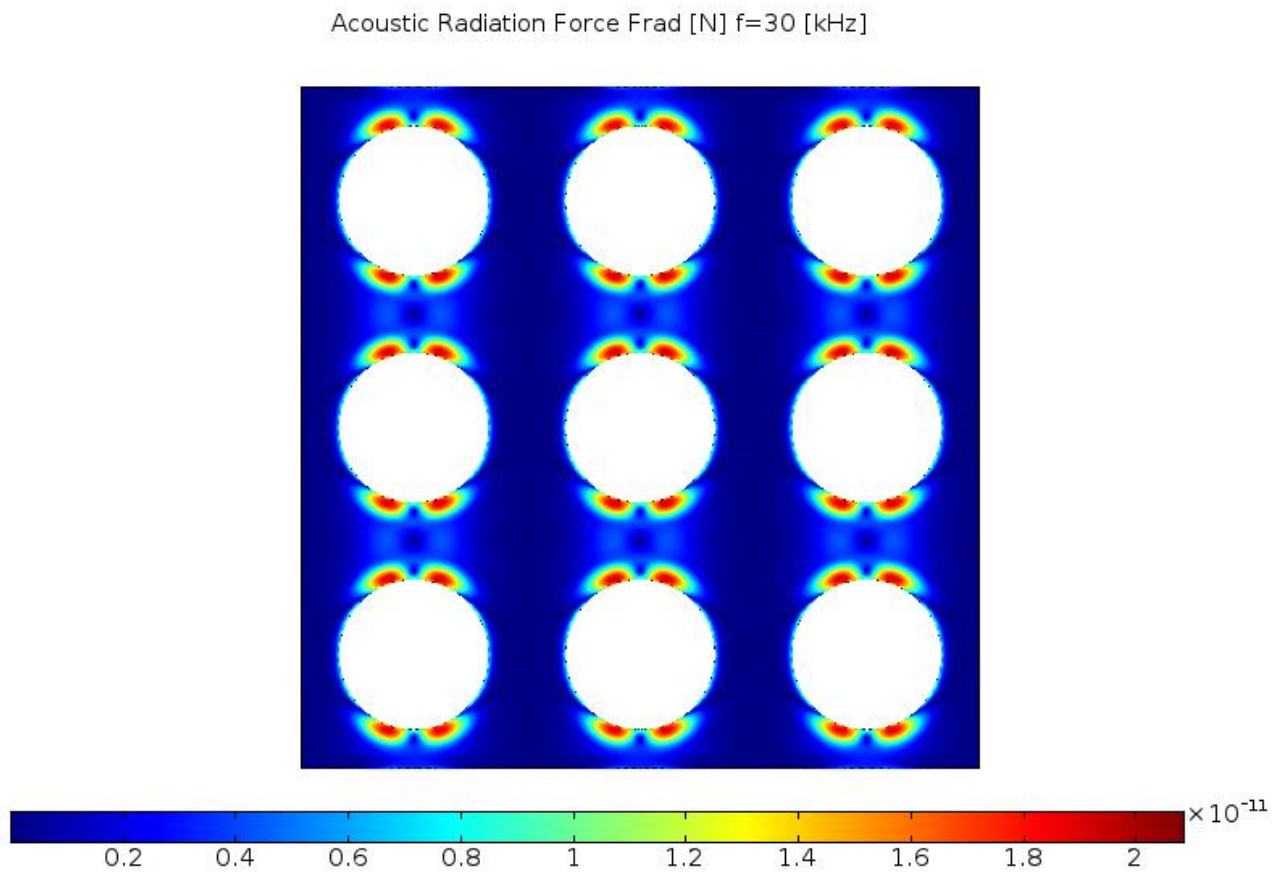


Figure 30: Color plot of the magnitude of the acoustic radiation force

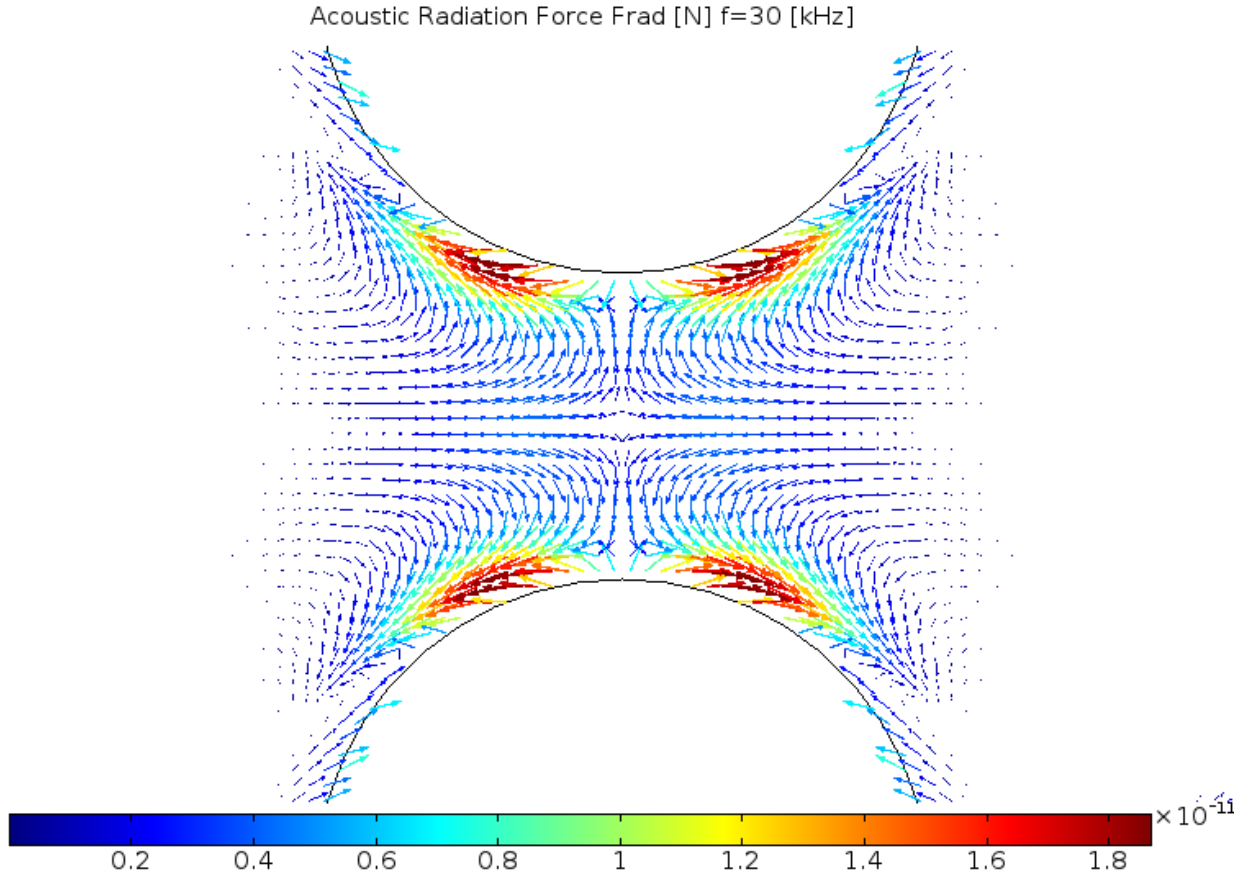


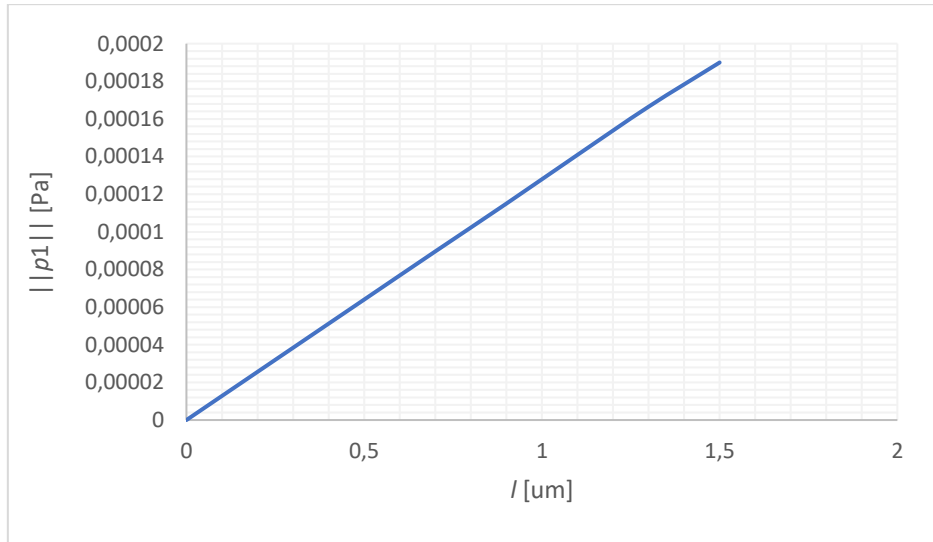
Figure 31: Vector plot of the acoustic radiation force in the vertical gap between two consecutive pillars

Figure 30 shows that the acoustic radiation force is significant only in the thin annulus around the pillars, it is minimum in the gap and zero in the remaining part of the section. Figure 31 reveals that F^{rad} enforces the acoustic streaming in trapping the particles inside the Rayleigh vortices, being the acoustic radiation force in similar directions of the second-order velocity trajectories. The acoustic radiation force will be significant in capturing the larger particles inside the streaming rolls, while for the smallest particles the trapping is due mainly to the magnitude of \mathbf{v}_2 .

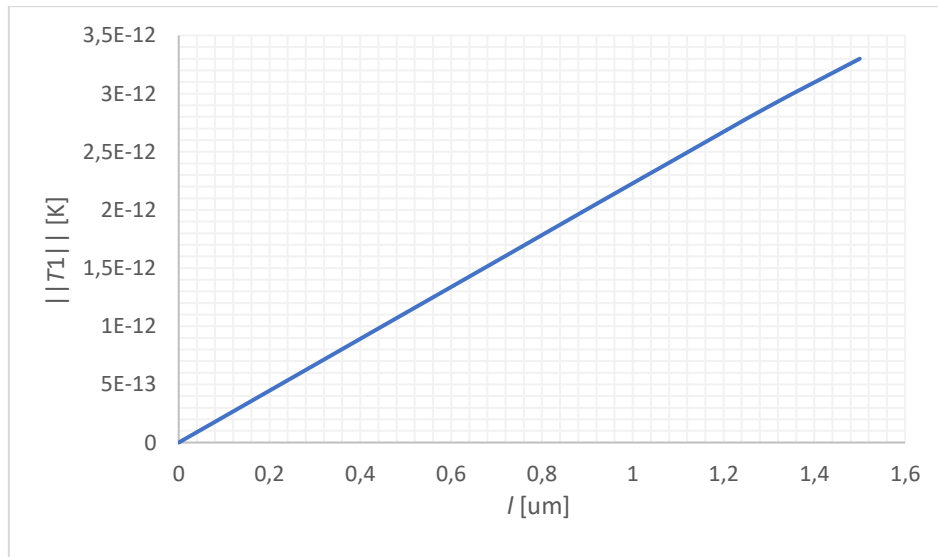
Effect of the amplitude of the displacement

In this section we want to analyze the effect of the amplitude of the displacement on the first and second-order fields. We perform the simulation with different values of the amplitude l varying in the range $[0 ; 1.5] \mu\text{m}$. The maximum value $l = 1.5 \mu\text{m}$ has been selected in order to respect the limit imposed by the perturbation method for $\varepsilon = \frac{l}{d_{\text{plr}}} \ll 1$ where ε is the perturbation parameter and d_{plr} the diameter of the pillars. It means that $l \ll d_{\text{plr}}$ and considering a diameter of $d_{\text{plr}} = 40 \mu\text{m}$, $l_{\text{max}} = 1.5 \mu\text{m}$ can be an acceptable value. In the experiments, the value of the imposed displacement can be adjusted changing the amplitude of the voltage.

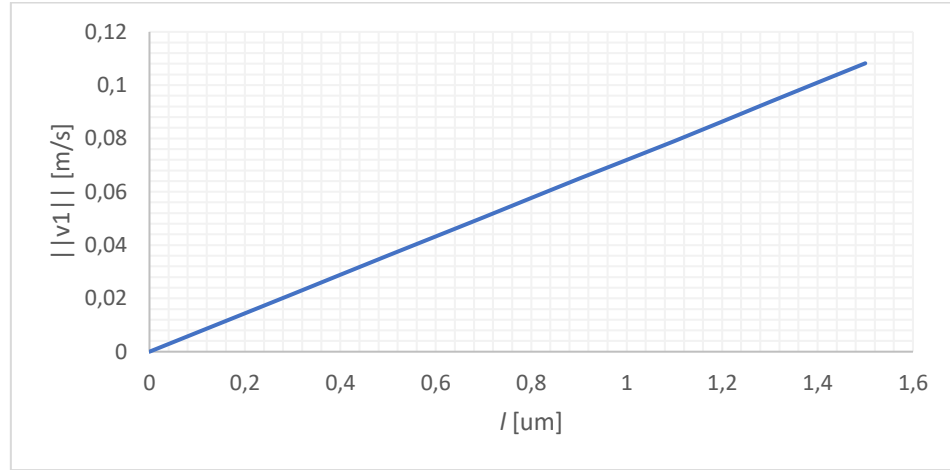
(a)



(b)



(c)



(d)

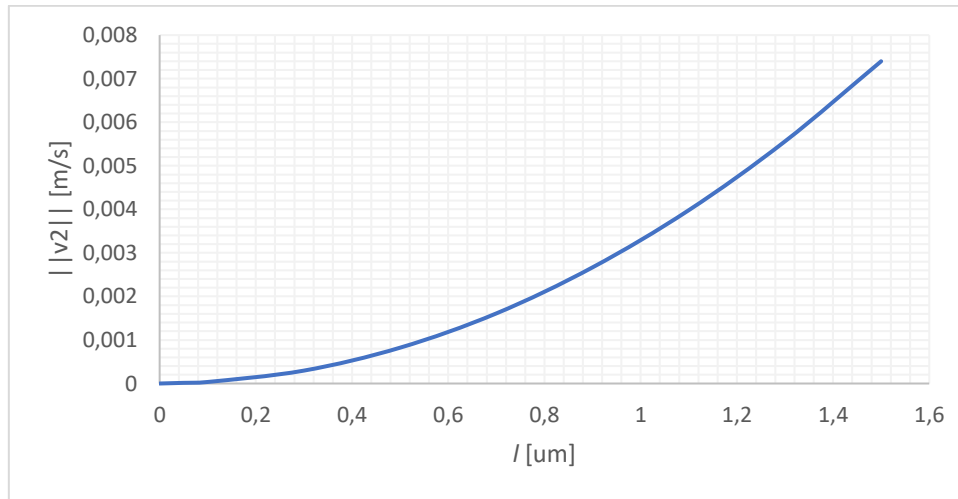


Figure 32: Line plots of the average values of the first-order pressure (a), temperature (b) velocity (c), second-order velocity (d) respect to the pillars deflection

Figures 32 (a-b-c) show that the first-order acoustic variables have a linear dependence on the oscillation amplitude. On the other hand, the second-order streaming velocity in figure 32 (d) is a quadratic function of the displacement. This is expected, being the first-order pressure and velocity

linearly-dependent on the oscillation amplitude and the second-order velocity a quadratic function on the first-order pressure and velocity. This result is confirmed by a similar analysis conducted by Huang *et al.* on a microchannel with oscillating sharp edges [4]. Varying the displacement of the walls from 0 to 5 μm , they found a parabolic profile of the streaming velocity. As a result, increasing the amplitude of the displacement, the “strength” of the streaming vortices raise quadratically. However, the variation of the amplitude is limited by the dimension of the pillars, in order to respect the condition on the perturbation parameter. Thus, in our simulation the amplitude of the displacement will be kept constant at $l = 0,5 \mu\text{m}$.

Effect of the distance between the pillars

Now we study the effects of the geometry on the solution by comparing the results computed with different distance between the pillars $d = 60, 80, 100, 120 \mu\text{m}$ and keeping constant all the other values. As the distance between two adjacent pillars become larger, more water flows in the 3X3 grid so a different behaviour of the fluid response is expected. The new flow rates can be obtained with equation (7.39) changing the values of d . Increasing the distance, a slower flow is expected between two consecutive pillars. Being S the section between the pillar available for the fluid flow, the mean velocity between two pillars of the computational domain can be calculated as:

$$v_{\text{plr}} = \frac{m_{\text{section}}}{\rho_0 S} = \frac{\frac{m_{\text{tot}}}{N_{\text{sections}}}}{\rho_0 h 3d} = \frac{\frac{\frac{m_{\text{tot}}}{w}}{6r_{\text{plr}}+3d}}{\rho_0 h 3d} = \frac{m_{\text{tot}} (6r_{\text{plr}}+3d)}{w \rho_0 h 3d} \quad (7.7.2)$$

and being m_{tot} , w , ρ_0 , h constant:

$$v_{\text{plr}} \sim 2 \frac{r_{\text{plr}}}{d} \quad (7.7.3)$$

Increasing the distance between the pillars, a reduced mean velocity is expected.

We do not study the acoustic fields, since the most significant effects of the variations of d are expected on the streaming velocity.

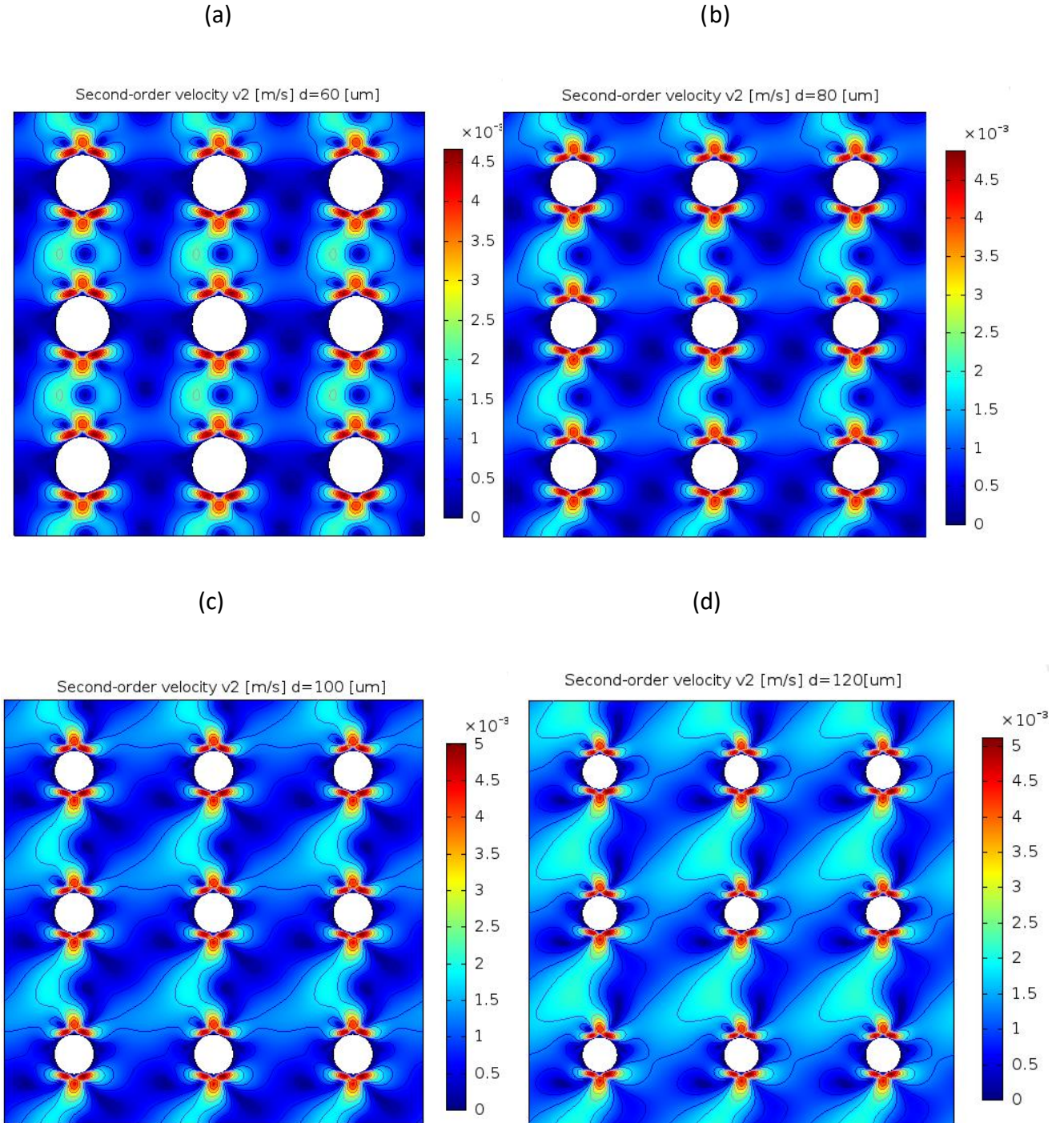
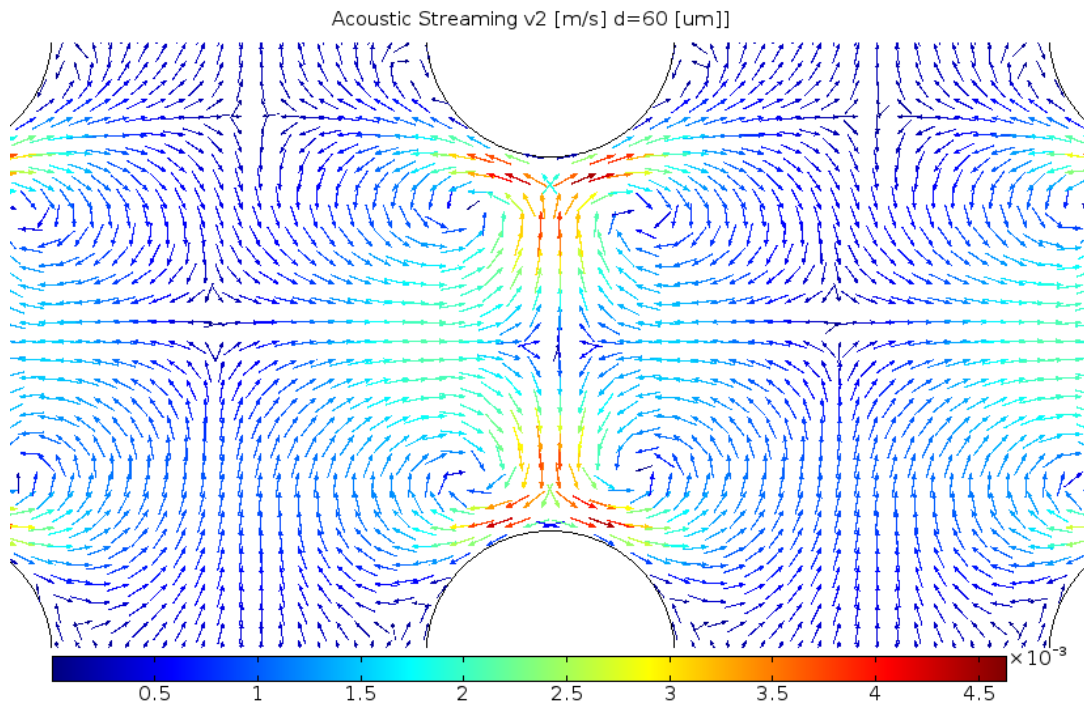


Figure 33: Color plots of the magnitude of the second-order velocity for different values of the distance between the pillars: : (a) 60 μm , (b) 80 μm , (c) 100 μm , (d) 120 μm

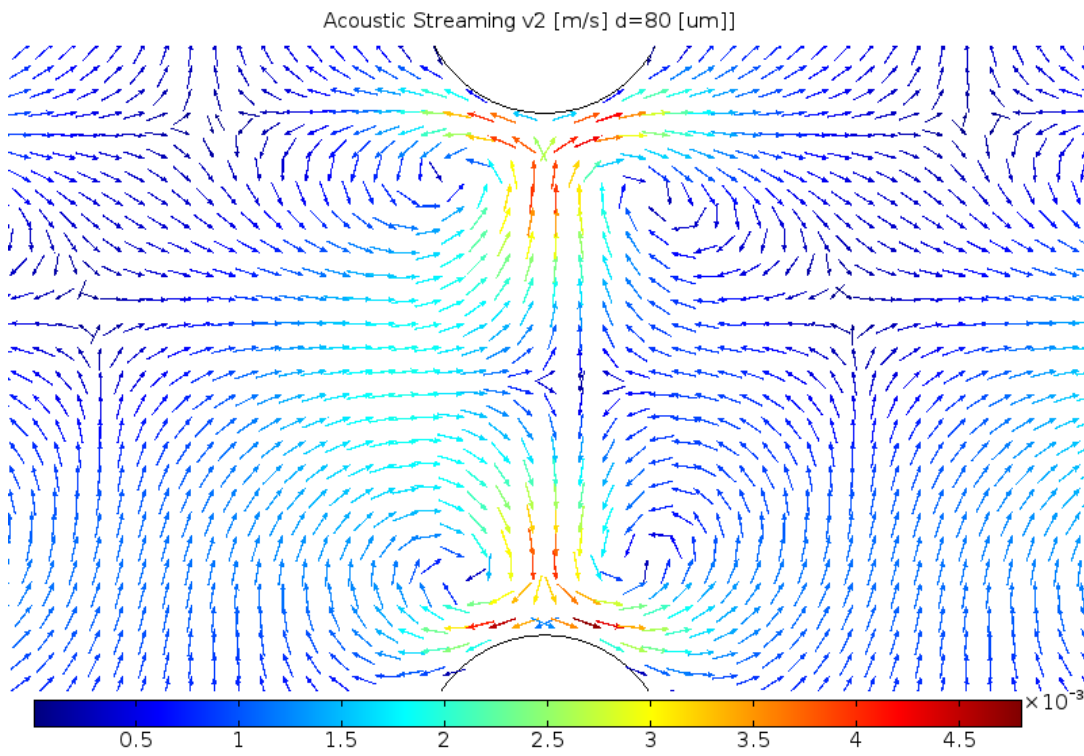
Figures 33 show how increasing the distance between the pillars the second-order velocity has significant variations. As expected, the mean velocity between two pillars is reduced. The two local maxima between the pillars vanish, while a single local maxima arise between the two Schlichting rolls in the boundary layer near the pillars. Moreover, a net flow can be seen between two pillars and it becomes more evident as the gap becomes wider. It means that increasing the distance between the pillars, the flow to the outlet is enhanced, while the eddies formation becomes weaker. This is confirmed by the following vector plots. Adopting larger values of d , the vortices tend to disappear and the fluid drift to the outlet of the domain. When $d = 100 \mu\text{m}$ the vortices start to lose completely their influence in the streaming pattern of the fluid. For $d = 120 \mu\text{m}$ the eddies are completely absent. We can conclude that when a critical distance is overcome, the streaming trajectories fail to exhibit the vortices. This is due to the increasing of the mass flow rate between two pillars: increasing the distance, more space is available for the fluid flow between the pillars and the net flow overcomes the acoustic effects induced by the pillars vibration.

In the following section it is demonstrated that this critical distance is a function of the flow rate injected in the device.

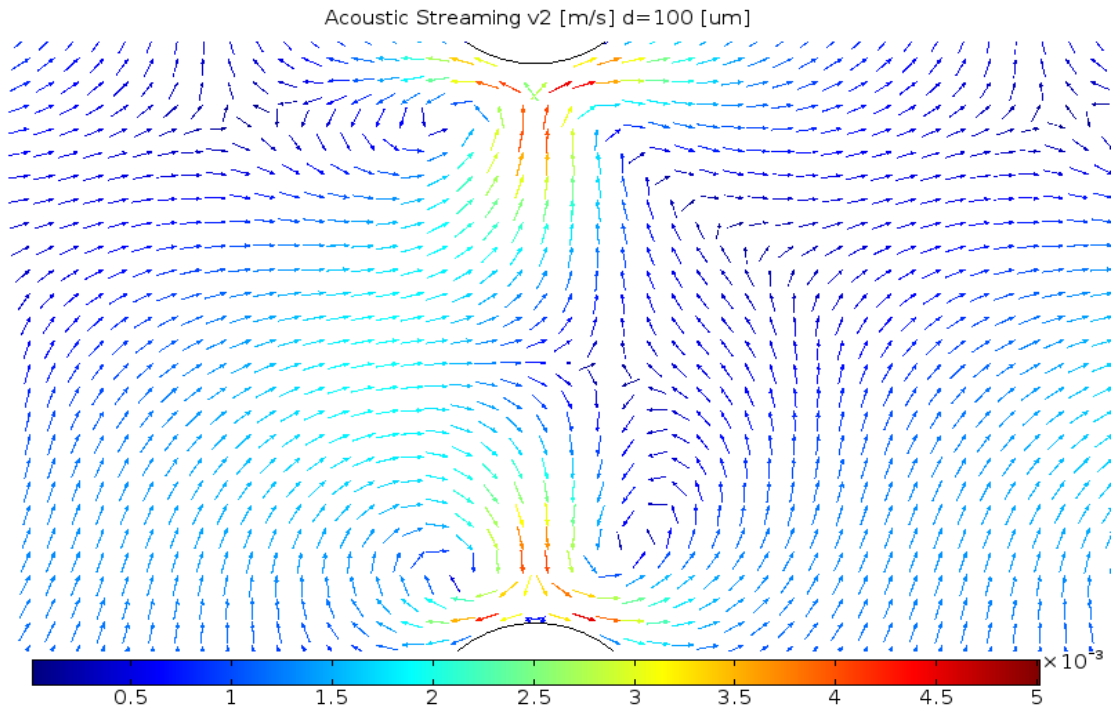
(a)



(b)



(c)



(d)

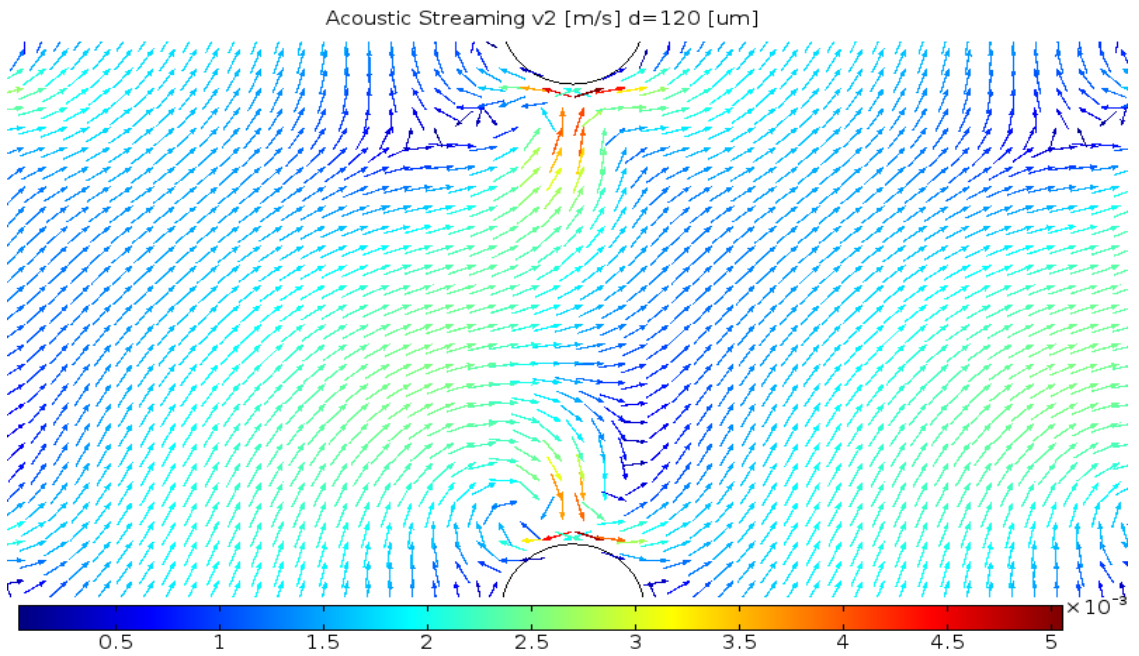


Figure 34: Vector plot of the second-order velocity for different values of the distance between the pillars: (a) 60 μm , (b) 80 μm , (c) 100 μm , (d) 120 μm

Critical trapping frequency

In this section we perform a parametric study of the minimum frequency necessary to trap the particles. The critical frequency is found to be a function of different parameters: the distance between the pillars, the flow rate injected with the syringe pump, the particles size and the oscillation amplitude. Nevertheless, it has been discussed previously that the amplitude of the oscillation is limited by the condition on the perturbation parameter, so we can not arbitrarily increase this value in order to trap the particles. We vary the distance between the pillars between 5 and 60 μm , with a step of 5 μm , studying the minimum frequency to trap particle with a prescribed size. Then, the same analysis is repeated for different sizes. The values of the particles radius taken into account are the same available in our laboratory: $2a_p = 0.5, 1, 2, 5 \mu\text{m}$. This procedure is repeated for four values of the water flow rate: $Q_{\text{tot}} = 4, 6, 7, 8 \mu\text{l/min}$. The flow rate $Q_{\text{tot}} = 0.5 \mu\text{l/min}$ has not been considered since it has been found that a distance of 100 μm is necessary to avoid the eddies formation. The following study is time consuming, since the simulation is repeated until the minimum frequency is found. Thus, a maximum value of 60 μm is taken into account. We have used a minimum distance of $d = 5 \mu\text{m}$, since a lower value is non reasonable from the point of view of the design.

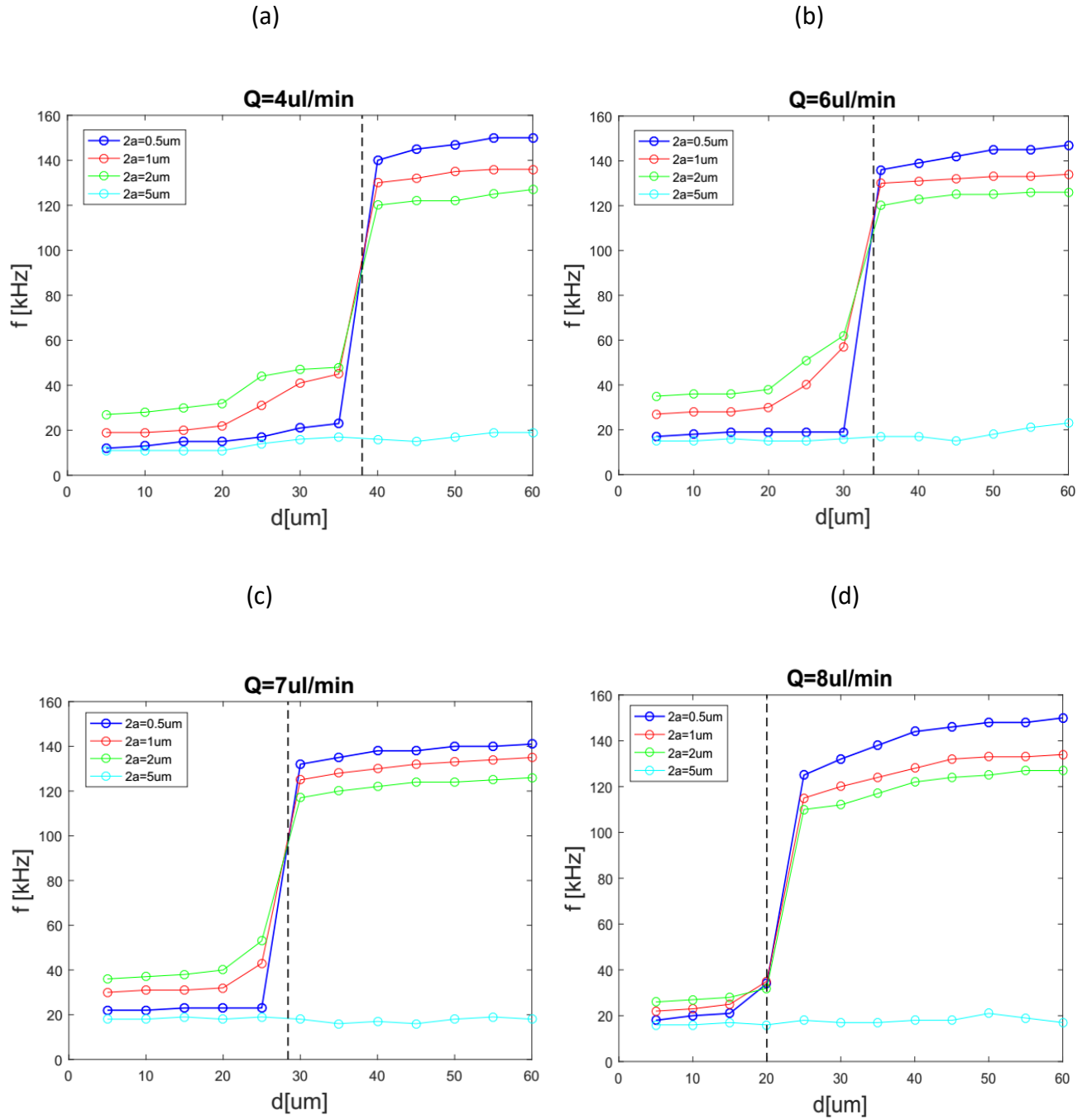


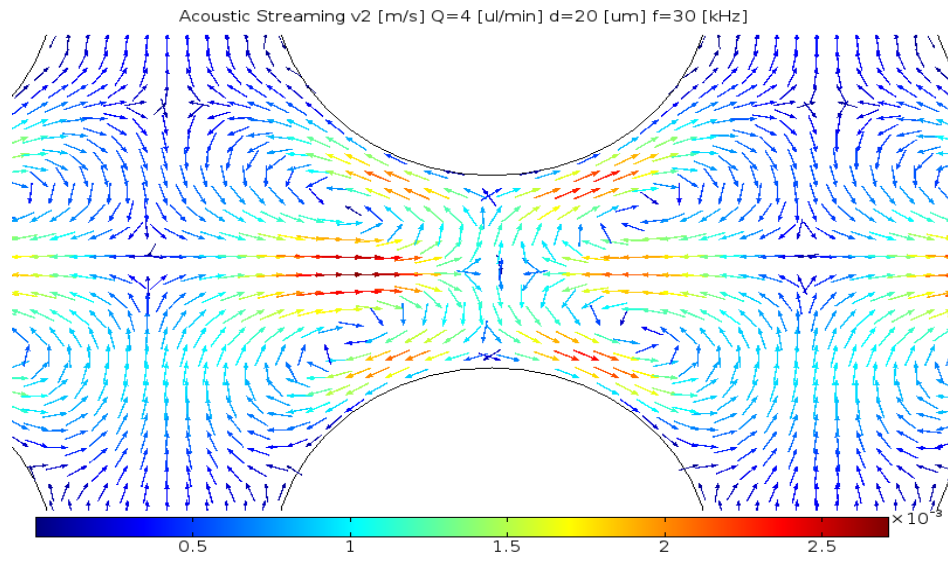
Figure 35 : Line plots of the minimum frequency for trapping particles of different sizes respectto the distance between the pillars for different flow rates: (a) 4 $\mu\text{l/min}$, (b) 6 $\mu\text{l/min}$, (c) 7 $\mu\text{l/min}$, (d) 8 $\mu\text{l/min}$.

Figures 35 show that over a critical distance, the minimum trapping frequency is higher for the smallest particles. On the other hand, beyond the critical distance, the required frequency is almost constant at low values. When the pillars are close to each other, streaming vortices are generated and a small particle is easily trapped by the eddies at a low frequency. In contrast, when the distance overcomes d_{crit} , the eddies tend to vanish. Nevertheless, with a significant increase of the applied frequency to the high value in the range of hundred of kHz, it is possible to win the effect of the drift flow and generate streaming eddies to trap the particles. This frequency is almost constant after the value of d_{crit} , and it is higher for the smaller particles. The critical distance decreases when more flow rate is injected in the channel: for $Q_{\text{tot}} = 4 \mu\text{l/min}$ $d_{\text{crit}} \approx 37 \mu\text{m}$, while for $Q_{\text{tot}} = 8 \mu\text{l/min}$ $d_{\text{crit}} \approx 20 \mu\text{m}$. The higher the flow rate, the wider the range of distances for which a high frequency is require. It has been found before that for a low flow rate $Q_{\text{tot}} = 0.5 \mu\text{l/min}$, $d_{\text{crit}} \approx 100 \mu\text{m}$, meaning that it is possible to trap the particles at a low frequency in a larger range of distances. On the other hand, the variation of the distance has no effect on the larger particles, which are trapped for a constant low frequency also for $d > d_{\text{crit}}$. The trapping of the larger particles is dominated by the acoustic radiation force, which is independent from the distance between the pillars. Figure 31 shows that also the acoustic radiation force has pseudo-vortices in the same direction of the acoustic streaming. Thus, combining, the pseudo-vortices of the acoustic radiation force and the trajectories of the streaming flow, the larger particles are trapped at low frequencies for arbitrary values of d . In the following figures, the patterns of the streaming velocity are provided for $Q_{\text{tot}} = 4 \mu\text{l/min}$, $f = 30 \text{ kHz}$, and two values of the distance:

- $d = 20 \mu\text{m} < 37 \mu\text{m} = d_{\text{crit}}$ (a)

- $d = 50 \mu\text{m} > 37 \mu\text{m} = d_{\text{crit}}$ (b)

(a)



(b)

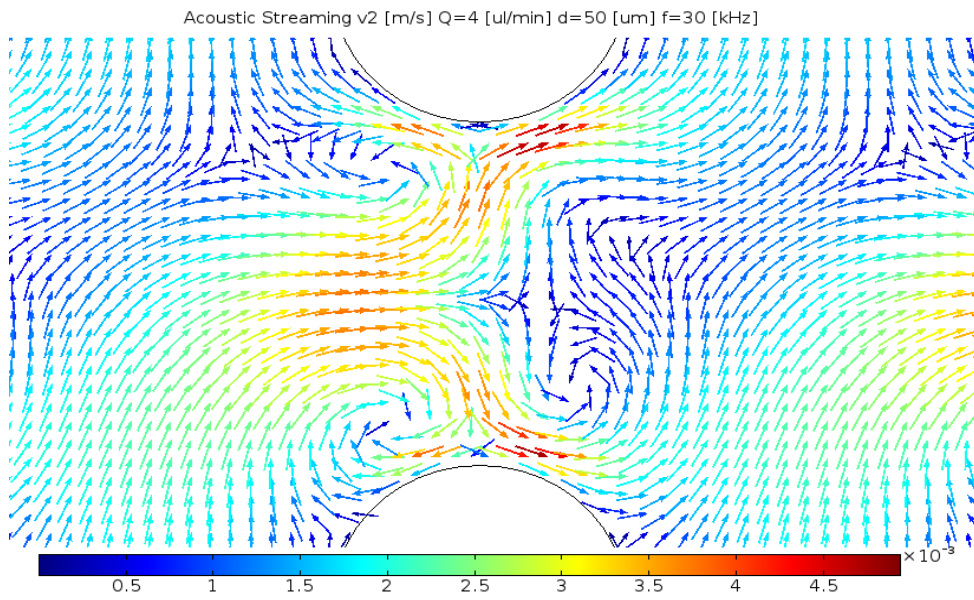


Figure 36 : Vector plots of the second-order velocities at $Q = 4 \mu\text{l/min}$, $f = 30 \text{ kHz}$: $d < d_{\text{crit}}$ (a)
 $d > d_{\text{crit}}$ (b)

As the figures reveal, for $d = 20 \mu\text{m}$ the streaming velocity exhibits the four Rayleigh streaming rolls in the bulk, while for $d = 50 \mu\text{m}$ the rolls are almost disappeared. Thus, for $d = 20 \mu\text{m}$ we have trapping, while $d = 50 \mu\text{m}$ the particles follow the drift flow to the outlet. The figure below shows the streaming trajectories for $d = 50 \mu\text{m}$ but at the frequency $f = 125 \text{ kHz}$. This is the minimum frequency require for trapping particles with a diameter of $2 \mu\text{m}$.

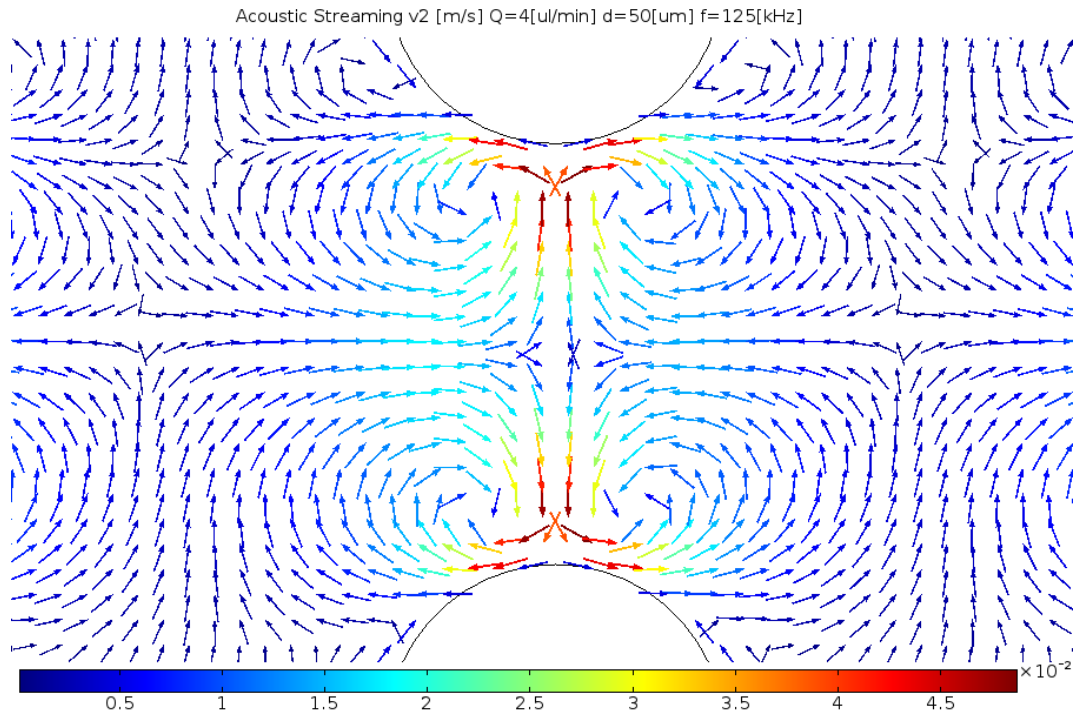


Figure 37: Vector plot of the second-order velocity at $Q = 4 \mu\text{l/min}$, $d > d_{\text{crit}}$ and $f = 125 \text{ kHz}$.

Increasing the frequency to 125 kHz , the streaming vortices are generated also for $d > d_{\text{crit}}$ and the trapping of the $2 \mu\text{m}$ particles is obtained.

CHAPTER 8

CONCLUSIONS

8.1 Summary

In the present work we studied the particles trapping in an acoustofluidic device using a numerical approach for providing a better knowledge of the physical phenomena involved in the experiments. In the device we investigated, particles manipulation was obtained with a grid of parallel circular pillars at a prescribed distance d . The pillars were forced to vibrate by the actuation of an incoming acoustic field generated by a piezo-transducer placed in contact with the channel walls. The material adopted to fabricate the device is PDMS, a soft polymer able to provide oscillations in the field of μm when actuated with a frequency in the range of kHz. It was observed that when a critical frequency f_{crit} was applied by the acoustic field generator, particles started to rotate near the pillars. The particles followed this circular motion because they were trapped inside the acoustic streaming small vortices. f_{crit} was found to be a function of the distance between the pillars d , the particle size a_p and the flow rate Q_{tot} pumped in the channel. The aim of the numerical simulation was to provide a parametric analysis of the acoustic-induced trapping in order to enhance the design and performance of the devices. The computational analysis developed in this thesis is based on the thermoviscous model of acoustofluidic presented by H.Bruus and T.J. Karlsen [6], where the equations of motion and the energy equation are solved with the Nyborg perturbation theory. The model was implemented in

COMSOL Multiphysics, an open source software which computes the numerical results with different physical interfaces using the finite elements method; in our simulation the first-order oscillating field is computed with the Thermoacoustics interface, while the second-order steady streaming is solved with the Laminar Flow interface. The oscillation of pillars was simulated with a velocity having the form of a standing plane wave $v_{1y} = \omega l e^{-i\omega t}$ travelling in the vertical direction. In the bulk of the fluid, the acoustic response p_1, T_1 and \mathbf{v}_1 was found to oscillate harmonically in the direction of the oscillation. This behaviour is confirmed by the theoretical solution obtained by H.Bruus [10] in the analysis of the resonances modes of the acoustic response of a fluid enclosed between two infinite and parallel oscillating walls. On the other hand, in the critical area between two pillars, p_1 and T_1 exhibited a linear variation along the y direction, while \mathbf{v}_1 was parabolic. As a result, the physical behaviour of the fluid, in the region near the was completely different from the rest of the channel. The thermal and the viscous boundary layer thickness δ_{th} and δ_s were computed well by the implemented model. Moreover, between two consecutive pillars, the second-order velocity \mathbf{v}_2 was found to have a response similar to the Schlichting-Rayleigh streaming, meaning that this model, with some approximations can be adapted to our scenario. Coupled with this, the streaming pattern of \mathbf{v}_2 followed similar trajectories predicted by the theoretical study of the acoustic streaming generated by an oscillating cylindrical body in a fluid at rest, presented by H.Schlichting and K. Gersten in the textbook '*Boundary Layer analysis*'. Then, changing the distance between the pillars, significant variations in the spatial configurations of the streaming velocity were found. Increasing the distance between the pillars, the streaming vortices tended to vanish since the drift flow became dominant. A similar behaviour was found by Huang *et al.* [3] in the investigation of streaming phenomena around oscillating sharp edges: increasing the distance between the oscillating edges, the streaming rolls started to disappear. The first and second-order velocities were found to be respectively a linear and parabolic function of the

amplitude of the oscillation, confirming the analytical predictions . Furthermore, the acoustic radiation force was significant only in the thin boundary layer around the pillars ; coupled with this, due to its direction parallel and concordant to the to streaming-induced vortices , it enforced the particles trapping near the pillars. The critical frequency f_{crit} for trapping particles was found to be strongly related to the distance between the pillars, having the latter evident consequences on the streaming rolls generation. For the smallest particles, dominated by the acoustic streaming, the trapping frequency had a different trend according to a critical distance d_{crit} . For $d > d_{crit}$ high frequencies are required, for $d < d_{crit}$ lower values could be used. The value of d_{crit} was found to decrease when the flow rate injected in the channel was intensified: for high flow rates the range of distances for which a high frequency was necessary became wider. On the contrary, for moderate flow rates d_{crit} increased, meaning that trapping could be achieved with more modest frequencies also when the distance between the pillars became larger. On the other side, a constant and low frequency was sufficient for the larger particles dominated by the acoustic radiation force, since the latter was independent from d_{crit} . We can conclude that in order to fulfill an efficient trapping of the small particles at low frequencies, it is more convenient to design pillars close to each other and operate with reduced flow rates. Given a certain design distance, figure 36 suggests the maximum flow to be imposed in order to trap the particles with small frequencies. Low frequencies are required to keep the wavelength below the transverse size of the channel and treating the acoustic field as a standing plane wave travelling in the vertical direction, which is the main assumption of our numerical model.

8.2 Future works

In this thesis we investigated the particles trapping obtained with streaming effects around circular pillars but many different shapes can be designed to generate vorticity. Following the same guidelines of this work, new geometries like squared and triangular pillars can be studied. In particular, it is well known from previous works that consistent streaming can be generated around oscillating tips [4][13]. These types of pillars can become good candidates to generate more efficient trapping and substitute cylindrical pillars. In the following figures we can see the streaming velocity for triangular pillars:

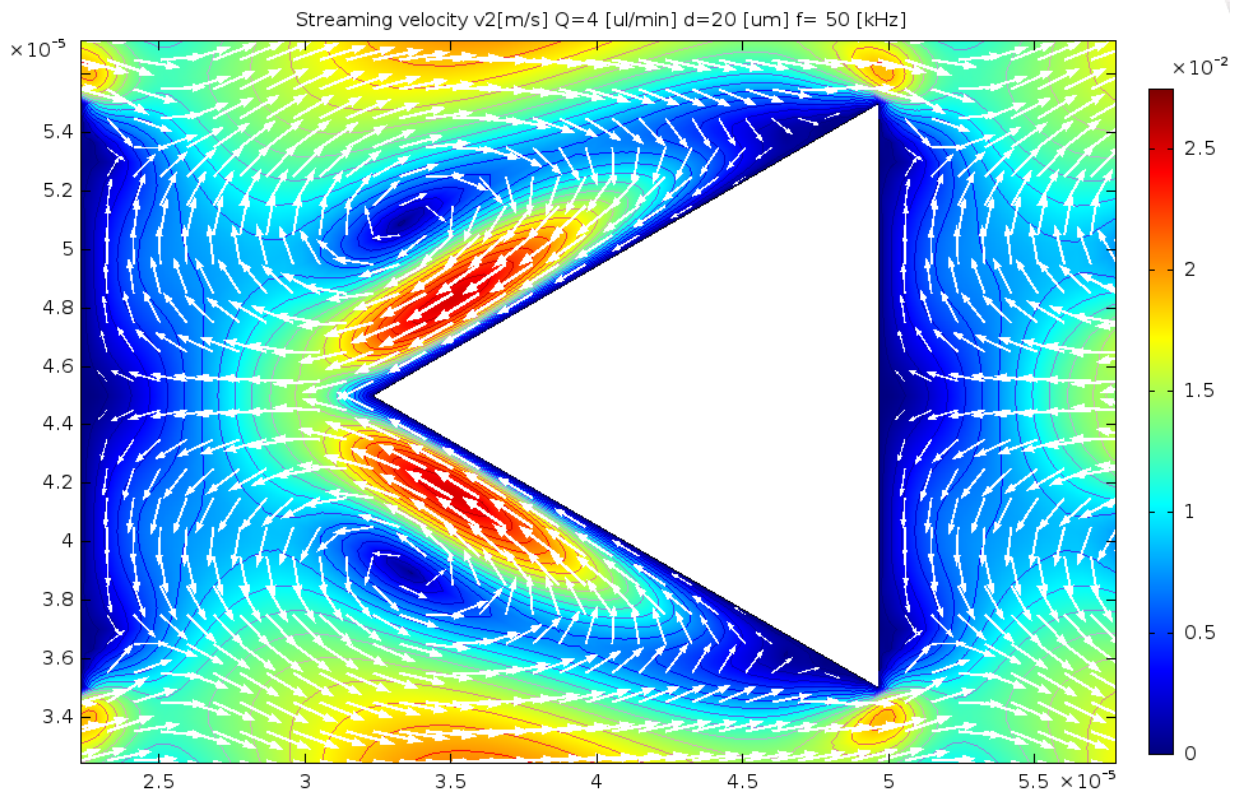



Figure 38: Color plot of the second-order velocity adopting triangular pillars

Appendix A

PERMISSIONS

Appendix A (continued)




Welcome, Marco
Not you?

[Log out](#) | [Cart \(0\)](#) | [Manage Account](#) | [Feedback](#) | [Help](#) | [Live Help](#)

[Get Permission / Find Title](#)
 [Go](#)
[Advanced Search Options](#)

[<< Back to view orders](#)

[Copy order >](#)


[Print this page](#)
[Print terms & conditions](#)
[Print citation information](#)
[\(What's this?\)](#)

Confirmation Number: 11712821
Order Date: 04/20/2018

Customer Information
Customer: Marco Ragone
Account Number: 3001273879
Organization: Marco Ragone
Email: mragon2@uic.edu
Phone: +39 13125720387


Search order details by: [Go](#)

This is not an invoice

Order Details
Journal of micromechanics and microengineering : structures, devices, and systems

Billing Status:
N/A

Order detail ID: 71135024
ISSN: 0960-1317
Publication Type: Journal
Volume:
Issue:
Start page:
Publisher: INSTITUTE OF PHYSICS PUBLISHING
Author/Editor: Institute of Physics (Great Britain) ; American Institute of Physics

Permission Status:  **Granted**
Permission type: Republish or display content
Type of use: Thesis/Dissertation
Order License Id: 4333360917351
[View details](#)

Note: This item was invoiced separately through our **RightsLink service.** [More info](#)

\$ 0.00

Total order items: 1
Order Total: \$0.00

[About Us](#) | [Privacy Policy](#) | [Terms & Conditions](#) | [Pay an Invoice](#)
 Copyright 2018 Copyright Clearance Center

Appendix A (continued)



RightsLink®

Home

Account
Info

Help



Title: Acoustofluidics 2: Perturbation theory and ultrasound resonance modes

Author: Henrik Bruus

Publication: Lab on a Chip

Publisher: Royal Society of Chemistry

Date: Nov 21, 2011

Copyright © 2011, Royal Society of Chemistry

Logged in as:
Marco Ragone
Account #: 3001273879

[LOGOUT](#)
Order Completed

Thank you for your order.

This Agreement between Mr. Marco Ragone ("You") and Royal Society of Chemistry ("Royal Society of Chemistry") consists of your license details and the terms and conditions provided by Royal Society of Chemistry and Copyright Clearance Center.

Your confirmation email will contain your order number for future reference.

[printable details](#)

License Number	4331070459480
License date	Apr 16, 2018
Licensed Content Publisher	Royal Society of Chemistry
Licensed Content Publication	Lab on a Chip
Licensed Content Title	Acoustofluidics 2: Perturbation theory and ultrasound resonance modes
Licensed Content Author	Henrik Bruus
Licensed Content Date	Nov 21, 2011
Licensed Content Volume	12
Licensed Content Issue	1
Type of Use	Thesis/Dissertation
Requestor type	academic/educational
Portion	figures/tables/images
Number of figures/tables/images	3
Distribution quantity	1
Format	print and electronic
Will you be translating?	no
Order reference number	
Title of the thesis/dissertation	Numerical analysis of an acoustofluidic device for particle trapping
Expected completion date	May 2018
Estimated size	100
Attachment	
Requestor Location	Mr. Marco Ragone Via Paradigna 13 Parma, Parma 431000 Italy Attn: Mr. Marco Ragone
Billing Type	Invoice
Billing address	Mr. Marco Ragone Via Paradigna 13

Appendix A (continued)

**ROYAL SOCIETY OF CHEMISTRY LICENSE
TERMS AND CONDITIONS**

Apr 16, 2018

This Agreement between Mr. Marco Ragone ("You") and Royal Society of Chemistry ("Royal Society of Chemistry") consists of your license details and the terms and conditions provided by Royal Society of Chemistry and Copyright Clearance Center.

License Number	4331071052987
License date	Apr 16, 2018
Licensed Content Publisher	Royal Society of Chemistry
Licensed Content Publication	Lab on a Chip
Licensed Content Title	Acoustofluidics 14: Applications of acoustic streaming in microfluidic devices
Licensed Content Author	Martin Wiklund,Roy Green,Mathias Ohlin
Licensed Content Date	Jun 12, 2012
Licensed Content Volume	12
Licensed Content Issue	14
Type of Use	Thesis/Dissertation
Requestor type	academic/educational
Portion	figures/tables/images
Number of figures/tables/images	1
Format	print and electronic
Distribution quantity	1
Will you be translating?	no
Order reference number	
Title of the thesis/dissertation	Numerical analysis of an acoustofluidic device for particles trapping
Expected completion date	May 2018
Estimated size	100
Requestor Location	Mr. Marco Ragone Via Paradigna 13 Parma, Parma 431000 Italy Attn: Mr. Marco Ragone
Billing Type	Invoice
Billing Address	Mr. Marco Ragone Via Paradigna 13 Parma, Italy 431000 Attn: Mr. Marco Ragone
Total	0.00 USD
Terms and Conditions	

This License Agreement is between {Requestor Name} ("You") and The Royal Society of Chemistry ("RSC") provided by the Copyright Clearance Center ("CCC"). The license consists of

Appendix A (continued)

**ROYAL SOCIETY OF CHEMISTRY LICENSE
TERMS AND CONDITIONS**

Apr 16, 2018

This Agreement between Mr. Marco Ragone ("You") and Royal Society of Chemistry ("Royal Society of Chemistry") consists of your license details and the terms and conditions provided by Royal Society of Chemistry and Copyright Clearance Center.

License Number	4331070739268
License date	Apr 16, 2018
Licensed Content Publisher	Royal Society of Chemistry
Licensed Content Publication	Lab on a Chip
Licensed Content Title	Acoustofluidics 13: Analysis of acoustic streaming by perturbation methods
Licensed Content Author	S. S. Sadhal
Licensed Content Date	Jun 1, 2012
Licensed Content Volume	12
Licensed Content Issue	13
Type of Use	Thesis/Dissertation
Requestor type	academic/educational
Portion	figures/tables/images
Number of figures/tables/images	3
Format	print and electronic
Distribution quantity	1
Will you be translating?	no
Order reference number	
Title of the thesis/dissertation	Numerical analysis of an acoustofluidic device for particles trapping
Expected completion date	May 2018
Estimated size	100
Requestor Location	Mr. Marco Ragone Via Paradigna 13 Parma, Parma 431000 Italy Attn: Mr. Marco Ragone
Billing Type	Invoice
Billing Address	Mr. Marco Ragone Via Paradigna 13 Parma, Italy 431000 Attn: Mr. Marco Ragone
Total	0.00 USD

Terms and Conditions

This License Agreement is between {Requestor Name} ("You") and The Royal Society of Chemistry ("RSC") provided by the Copyright Clearance Center ("CCC"). The license consists of

Appendix A (continued)

**ROYAL SOCIETY OF CHEMISTRY LICENSE
TERMS AND CONDITIONS**

Apr 16, 2018

This Agreement between Mr. Marco Ragone ("You") and Royal Society of Chemistry ("Royal Society of Chemistry") consists of your license details and the terms and conditions provided by Royal Society of Chemistry and Copyright Clearance Center.

License Number	4331061053970
License date	Apr 16, 2018
Licensed Content Publisher	Royal Society of Chemistry
Licensed Content Publication	Lab on a Chip
Licensed Content Title	Acoustofluidics 7: The acoustic radiation force on small particles
Licensed Content Author	Henrik Bruus
Licensed Content Date	Feb 21, 2012
Licensed Content Volume	12
Licensed Content Issue	6
Type of Use	Thesis/Dissertation
Requestor type	academic/educational
Portion	figures/tables/images
Number of figures/tables/images	2
Format	print and electronic
Distribution quantity	1
Will you be translating?	no
Order reference number	
Title of the thesis/dissertation	Numerical analysis of an acoustofluidic device for particles trapping
Expected completion date	May 2018
Estimated size	100
Requestor Location	Mr. Marco Ragone Via Paradigna 13 Parma, Parma 431000 Italy Attn: Mr. Marco Ragone
Billing Type	Invoice
Billing Address	Mr. Marco Ragone Via Paradigna 13 Parma, Italy 431000 Attn: Mr. Marco Ragone

Appendix A (continued)

23/4/2018

RightsLink Printable License

**ROYAL SOCIETY OF CHEMISTRY LICENSE
TERMS AND CONDITIONS**

Apr 23, 2018

This Agreement between Mr. Marco Ragone ("You") and Royal Society of Chemistry ("Royal Society of Chemistry") consists of your license details and the terms and conditions provided by Royal Society of Chemistry and Copyright Clearance Center.

License Number	4335130337147
License date	Apr 23, 2018
Licensed Content Publisher	Royal Society of Chemistry
Licensed Content Publication	Lab on a Chip
Licensed Content Title	Acoustofluidics 5: Building microfluidic acoustic resonators
Licensed Content Author	A. Lenshof, M. Evander, T. Laurell, J. Nilsson
Licensed Content Date	Jan 16, 2012
Licensed Content Volume	12
Licensed Content Issue	4
Type of Use	Thesis/Dissertation
Requestor type	academic/educational
Portion	figures/tables/images
Number of figures/tables/images	1
Format	print and electronic
Distribution quantity	10
Will you be translating?	no
Order reference number	
Title of the thesis/dissertation	Numerical analysis of an acoustofluidic device for particles trapping
Expected completion date	May 2018
Estimated size	1
Requestor Location	Mr. Marco Ragone Via Paradigna 13 Parma, Parma 431000 Italy Attn: Mr. Marco Ragone
Billing Type	Invoice
Billing Address	Mr. Marco Ragone Via Paradigna 13 Parma, Italy 431000 Attn: Mr. Marco Ragone
Total	0.00 USD

Terms and Conditions

This License Agreement is between {Requestor Name} ("You") and The Royal Society of Chemistry ("RSC") provided by the Copyright Clearance Center ("CCC"). The license consists of your order details, the terms and conditions provided by the Royal Society of Chemistry, and the payment terms and conditions.

Appendix A (continued)

23/4/2018

RightsLink Printable License

**ROYAL SOCIETY OF CHEMISTRY LICENSE
TERMS AND CONDITIONS**

Apr 23, 2018

This Agreement between Mr. Marco Ragone ("You") and Royal Society of Chemistry ("Royal Society of Chemistry") consists of your license details and the terms and conditions provided by Royal Society of Chemistry and Copyright Clearance Center.

License Number	4335130179379
License date	Apr 23, 2018
Licensed Content Publisher	Royal Society of Chemistry
Licensed Content Publication	Lab on a Chip
Licensed Content Title	Tipping the balance of deterministic lateral displacement devices using dielectrophoresis
Licensed Content Author	Jason P. Beech, Peter Jönsson, Jonas O. Tegenfeldt
Licensed Content Date	Jun 15, 2009
Licensed Content Volume	9
Licensed Content Issue	18
Type of Use	Thesis/Dissertation
Requestor type	academic/educational
Portion	figures/tables/images
Number of figures/tables/images	1
Format	print and electronic
Distribution quantity	10
Will you be translating?	no
Order reference number	
Title of the thesis/dissertation	Numerical analysis of an acoustofluidic device for particles trapping
Expected completion date	May 2018
Estimated size	1
Requestor Location	Mr. Marco Ragone Via Paradigna 13 Parma, Parma 431000 Italy Attn: Mr. Marco Ragone
Billing Type	Invoice
Billing Address	Mr. Marco Ragone Via Paradigna 13 Parma, Italy 431000 Attn: Mr. Marco Ragone
Total	0.00 USD
Terms and Conditions	

This License Agreement is between {Requestor Name} ("You") and The Royal Society of Chemistry ("RSC") provided by the Copyright Clearance Center ("CCC"). The license consists of

CITED LITERATURE

1. Evander, M. and Nilsson, J. : Acoustofluidics 20: Applications in acoustic trapping, Lab Chip, 2012, 12, 4667-4676
2. Dual, J. and Schwarz, T. : Acoustofluidics 3: Continuum mechanics for ultrasonic particle manipulation Lab Chip, 2012, 12, 244-252
3. Bruus, H.: Theoretical Microfluidics, OXFORD MASTER SERIES IN CONDENSED MATTER PHYSICS , Oxford University Press, 2008
4. Nama, N., Huang, P., Huang,T. and Costanzo, F. : Investigation of acoustic streaming patterns around oscillating sharp edges, Lab Chip, 2014, 14, 2824-2836
5. Bruus, H. : Acoustofluidics 7: The acoustic radiation force on small particles, Lab Chip, 2012, 12, 1014
6. Bruus,H. and Karlsen, J.T. : Forces acting on a small particle in an acoustical field in a thermoviscous fluid, Physical Review , E92, 043010, 2015
7. Muller, P.B. , Barnkob,R., Jensen, M.J.H.and Bruus, H. : A numerical study of microparticle acoustophoresis driven by acoustic radiation force and streaming-induced drag forces, Lab Chip, 2012, 12, 4617-4627
8. Bruus,H.,Dual,J., Hawkes, J., Hill, M., Laurell,T., Nilsson, J., Radel, S. , Sadhal, S. , Wiklund, M. : Acoustofluidics -exploiting ultrasonic standing wave forces and streaming in microfluidic systems for cell and particle manipulation Lab Chip, 2011, 11, 3579-3580
9. Ren,L., Chen,Y., Li, P., Mao, Z., Huang, P., Rufo, J.,Guo, F.,Wang,L., McCoy,J.P., Levine,S.J. and Huang, T.J. : Lab Chip, 2015, 15, 3870-3879
10. Xie, Y.; Ahmed, D.; Lapsley, M.I.; Lu, M.; Li, S.; Huang, T.J. ; Acoustofluidic Rely: Sequential trapping and Transporting of Microparticles via Acoustically Excited Oscillating Bubbles. Journal of Laboratory Automation, 2014, 1-7
11. Ozcelik, A.; Ahmed,D.; Xie, J.; Nama,N.; Qu,Z.; Nawaz, A.A.; Huang T.J. ; An Acoustofluidic Micromixer via Bubble Inception and Cavitation from Microchannel Sidewalls, Analytical Chemistry, 2014,86,5083-5088
12. Ahmed,D., Ozcelik, A., Bojanala, N., Nama, N., Upadhyay, A., Chen, Y., Hanna-Rose, W.,Huang, T.J.; Rotational manipulation of single cells and organisms using acoustic waves, nature COMMUNICATIONS, 2016, 7:11085

CITED LITERATURE (continued)

13. Ozcelik, A, Nama, N., Huang, P.H., Kaynak,M., McReynolds ,M.R., Hanna-Rose, W.and Huang, T.J. : Acoustofluidic Rotational Manipulation of Cells and Organisms Using Oscillating Solid Structures, Small journal, 2016, 5120-5125
14. McGrath, J., Jimenez, M., Bridle, H. : Deterministic lateral displacement for particle separation: a review Lab chip, 2014, 14, 4139-4158
15. Bruus,H., Settnes,M., Forces acting on a small particle in an acoustical field in a viscous fluid, Physical Review, E85, 016327, 2012
16. Barnkob, R., Nama, N., Ren,L., Huang, T.J., Costanzo and F.Kahler: Acoustically Driven Fluid and Particle Motion in Confined and Leaky Systems, PHYSICAL REVIEW APPLIED 9, 014027 (2018)
17. Bian,Y., Guo, F., Yang,S., Mao, Z., Bachman, H., Tang, S.Y., Ren, L., Zhang, B., Gong, J., Guo, X., and Huang, T.J.: Acoustofluidic waveguides for localized control of acoustic wavefront in micrfluidics; Microfluid Nanofluid (2017) 21:132
18. Mao, Z. ,Xie, Y., Guo, F. ,Ren, L. , Huang, P.H. , Chen, Y., Rufo, J. , Costanzo, F. and Huang, T.J. Experimental and numerical studies on standing surface acoustic waves in microfluidics Lab Chip, 2016, 16, 515
19. Nama, N., Barnkob, R. , Mao, Z. , Kahler, C.J. , Costanzo, F. and Huang T. J.: Numerical study of acoustophoretic motion of particles in a PDMS microchannel driven by surface acoustic waves Lab Chip, 2015, 2700-2709
20. Kaynak, M. , Ozcelik, A. , Nama, N. , Nourhani, A. , Lammert P.E. , Crespi, V.H. and Huang, T.J.: Acoustofluidic actuation of in situ fabricated microrotors Lab Chip, 2016, 16, 3532
21. Orbay, S., Ozcelik, A., Bachman, H. and Huang, T.J. : Acoustic actuation of *in situ* fabricated artificial cilia, Journal of Micromechanics and Microengineering, 2018, 18, 025012
22. Rivas, L. , Medina-Sanchez, M.; Escosura,M. and Merkoci, A.: Improving sensitivity of gold-nanoparticle-based lateral flow-assays by using wax-printed pillar as delay barriers of microfluidics Lab Chip, 2014,14, 4406

CITED LITERATURE (continued)

23. Niu, X. , Gulati, S. , Edel, J.B. and deMello A. J. : Pillar-induced droplet merging in microfluidics circuits Lab Chip, 2008, 8, 1837-18417
24. Sadhal, S.S. : Acoustofluidics 13: Analysis of acoustic streaming by perturbation methods, Lab Chip, 2012, 12, 2292-2300
25. Wiklund, M. , Green, R. and Ohlin, M. : Acoustofluidics 14: Applications of acoustic streaming in acoustofluidics devices, Lab Chip, 2012, 12, 2438-2451
26. Schlichting, H. and Jersten, K. : Boundary Layer Theory, Springer, 2017, 9th edition
27. King, L.V. and London, R. Soc., Ser. A 147, 212 (1934)
28. Yosioka, K. and Kawasima, Y. : Acoustica 5, 167 (1955)
29. Gorkov, L. P. , Sov. Phys. Dokl. : 6, 773 (1962), Doklady Akademii Nauk SSSR 140, 88 (1961)
30. Doinikov, A.A., J.Acoust. Soc. Am. 101, 713 (1997)
31. Doinikov, A.A., J.Acoust. Soc. Am. 101, 722 (1997)
33. Doinikov, A.A., J.Acoust. Soc. Am. 101, 731 (1997)
33. Danilov, S.D. ; Mironov, M. A.; J. Acoust. Soc. Am. 107, 143 (2000)
34. Dual, J. And Moller, D. : Acoustofluidics 4: Piezoelectricity and application in the excitation of acoustic fields for ultrasonic particle manipulation Lab Chip, 2012, 12, 506-514
35. Lenshof, A. , Evander, M. , Laurell, T. and Nillson, J. : Acoustofluidics 5: Building microfluidic acoustic resonators Lab Chip, 2012, 12, 684-695
36. Wiklund, M. , Brismar, H. and Onfelt, B. : Acoustofluidics 18: Microscopy for acoustofluidic micro-devices Lab Chip, 2012, 12, 3221-3234

VITA

NAME	Marco Ragone
EDUCATION	
	Master of Science in Mechanical Engineering, University of Illinois at Chicago May 2018, USA
	Specialization Degree in Energy and Nuclear Engineering, July 2018 (expected), Polytechnic of Turin, Italy
	Bachelor's Degree in Energy Engineering
LANGUAGE SKILLS	
Italian	Native speaker
English	Full proficiency
	2016-IELTS examination
	A.Y. 2017/2018 One semester of study abroad in Chicago, Illinois
	A.Y. 2016/2017 One semester of lessons and exams attended exclusively In English
TECHNICAL SKILLS	
Basic level	Matlab, STAR CCM+
Average level	COMSOL Multyphysics